Investigation of Transient Phenomena of Proton Exchange Membrane Fuel Cells

by

Roongrojana Songprakorp

BSc, Prince of Songkhla University Thailand, 1986
MSc, King Mongkut's Institute of Technology Thonburi Thailand, 1996

A Thesis Submitted in Partial Fulfillment of the
Requirements for the Degree of
DOCTOR IN PHILOSOPHY
in the
Department of Mechanical Engineering.

University of Victoria

Investigation of Transient Phenomena of Proton Exchange Membrane Fuel Cells

by

Roongrojana Songprakorp

BSc, Prince of Songkhla University Thailand, 1986
MSc, King Mongkut's Institute of Technology Thonburi Thailand, 1996

Supervisory Committee

Dr. Ned Djilali, Supervisor (Dept. of Mechanical Engineering, University of Victoria)

Dr. Zuomin Dong, Departmental Member (Dept. of Mechanical Engineering, University of Victoria)

Dr. Andrew Rowe, Departmental Member (Dept. of Mechanical Engineering, University of Victoria)

Dr. Ashoka K.S. Bhat, Outside Member (Dept. of Electrical Engineering, University of Victoria)

Supervisory Committee

Dr. Ned Djilali, Supervisor (Dept. of Mechanical Engineering, University of Victoria)

Dr. Zuomin Dong, Departmental Member (Dept. of Mechanical Engineering, University of Victoria)

Dr. Andrew Rowe, Departmental Member (Dept. of Mechanical Engineering, University of Victoria)

Dr. Ashoka K.S. Bhat, Outside Member (Dept. of Electrical Engineering, University of Victoria)

Abstract

The research presented in this thesis is a contribution to the modeling and understanding of the dynamic behavior of proton exchange membrane fuel cells (PEMFCs). A time-dependent, two-phase non-isothermal model of the membrane electrode assembly was developed and implemented using the finite element method. In addition to solving a phenomenological transport equation for water in the membrane, the model takes into consideration the non-equilibrium water sorption to better capture some of the dynamic characteristics of water transport in the MEA. Mass transfer using Fickian diffusion is implemented in the model. Two different models describing the electrochemical reactions in the catalyst layer including a macro-homogeneous model and an agglomerate model, are also implemented. Conservation of energy is included in the solution procedure in order to assess the impact of thermal effects on the

dynamics of the transport in the MEA. For the purpose of model and concept validation, the model was first solved in a steady two-dimensional mode for a through-plane computational domain using a commercial software package, COMSOL Multiphysics version 3.2b. The impact of using a single- and two-phase modeling approaches was evaluated, and the predicted current-voltage performance characteristic are found in good agreement with the experimental data available in the literature. In addition, the developed model was benchmarked against a finite element-based in-house code for further validation and to evaluate numerical accuracy and computational performance.

Transient simulations of operation under dynamic voltage sweeps are presented, and parametric studies are conducted to investigate the impact of various model, operation and transport properties on the predicted dynamic cell performance. In particular, the rate of load change, the difference in water content between the anode and cathode, and the water sorptions rate are shown to have significant impact on cell performance in unsteady operation, especially at higher current densities. Parametric studies also address the sensitivity of the model results to physical properties, highlighting the importance of accurately determining certain physical properties of the fuel cell components. Finally, the application of the model to air-breathing fuel cells provides further insight into the dynamic performance characteristic of such type of fuel cells.

Table of Contents

List of Tables

List of Figures

Nomenclature

A_v	specific reaction interfacial area per volume of catalyst, $[m^{-1}]$
a_w	water activity, [-]
A_{Pt}	active surface area of platinum in the catalyst layer, $[m^2 \cdot kg^{-1} of platinum]$
c_i	molar concentration of species i, $[mol \cdot m^{-3}]$
$c_{H_2}^{ref}$	reference concentration of hydrogen, $[mol \cdot m^{-3}]$
$c_{H_{2,s}}$	concentration of hydrogen at the reaction site, $[mol \cdot m^{-3}]$
$c_{O_2}^{ref}$	reference concentration of oxygen, $[mol \cdot m^{-3}]$
C_{ox}	oxidized species concentration, $[mol \cdot m^{-3}]$
C_{red}	reduced species concentration, $[mol \cdot m^{-3}]$
c_{tot}	concentration of the mixture, $[mol \cdot m^{-3}]$
D_i	diffusion coefficient of species i in pore space, $[m^2 \cdot s^{-1}]$
d_j	mass coefficient, [-]
D_i^{eff}	diffusion coefficient of gas in gas diffusion layer, $[m^2 \cdot s^{-1}]$
E_r	effectiveness factor, [-]
eff	effective value, [-]
EW_m	equivalent weight of dry Nafion membrane, $[kg \cdot mol^{-1}]$
h_L	latent heat of water evaporation, $[J \cdot mol^{-1}]$
$H_{H_{2,N}}$	Henry's law constant for hydrogen in Nafion, $[Pa \cdot m^{-3} \cdot mol^{-1}]$
$H_{O_{2,N}}$	Henry's law constant for oxygen in Nafion, $[Pa \cdot m^{-3} \cdot mol^{-1}]$

i_0	exchange current density, $[A \cdot m^{-2}]$
k^H	dimensionless Henry's law constant, [-]
k^{eff}	effective thermal conductivity, $[W \cdot m^1 K^{-1}]$
k_c	reaction rate constant, $[s^{-1}]$
K_{abs}	absolute permeability, $[m^2]$
k_{cond}	condensation rate, $[s^{-1}]$
k_{evap}	evaporation rate, $[Pa^{-1} \cdot s^{-1}]$
$k_{l,k}$	relative permeability of liquid water in domain k, $[m^2]$
k_{la}	liquid water-electrolyte absorption coefficient, $[s^{-1}]$
k_{ld}	liquid water-electrolyte desorption coefficient, $[s^{-1}]$
$k_{v,k}$	relative permeability of water vapour in domain k, $[m^2]$
k_{va}	water vapour-electrolyte absorption coefficient, $[s^{-1}]$
k_{vd}	water vapour-electrolyte desorption coefficient, $[s^{-1}]$
m_{Pt}	platinum mass loading per unit area in the catalyst layer, $[kg \cdot m^{-2}]$
n	number of charges transferred
n_d	electro-osmotic drag coefficient, [-]
N_i	molar flux density of species i, $[mol \cdot cm^{-2} \cdot s^{-1}]$
p^{sat}	saturation pressure, [Pa]
P_c	capillary pressure, [Pa]
P_g	total pressure of mixture, [Pa]
P_l	liquid water pressure, [Pa]
p_v	partial pressure of water vapour, $[Pa]$
$Pt \mid C$	mass percentage of platinum on the support carbon black, [-]
r_{agg}	radius of agglomerate pellet, [m]
RH	relative humidity, [%]

s	liquid saturation, [-]
$S_{cond/evap}$	condensation/evaporation source term, $[mol \cdot m^{-3} \cdot s^{-1}]$
S_{ohm}	ohmic heat loss, $[J \cdot m^{-3}]$
S_{vsorp}	water vapour sorption source term, $[mol \cdot m^{-3} \cdot s^{-1}]$
U	internal energy rate, $[J \cdot kg^{-1}]$
u_i	mobility of species i, $[m^2 \cdot mol \cdot J^{-1} \cdot s^{-1}]$
v	reaction rate, $[mol \cdot m^{-2} \cdot s^{-1}]$
z_i	charge number of species i, [-]
E	electrical potential, [V]
F	Faraday's constant, 96495 $[C \cdot mol^{-1}]$
L	catalyst layer length, $[m]$
R	universal gas constant, 8.3143 $[J \cdot mol^{-1} \cdot K^{-1}]$
T	absolute temprature, [K]

Greek Letters

α	reaction transfer coefficient, [-]
δ_{agg}	Nafion film thickness covering the agglomerate, [m]
ϵ_N^{CTL}	electrolyte volume fraction in the catalyst layer, [-]
ϵ_S^{CTL}	solid phase volume fraction in the catalyst layer, [-]
ϵ_S^{GDL}	solid volume fraction in the gas diffusion layer, [-]
ϵ_V^{CTL}	void volume fraction in the catalyst layer, [-]
ϵ_V^{GDL}	porosity or void volume fraction in the gas diffusion layer, [-]
ϵ_{agg}	electrolyte volume fraction inside the agglomerate, [-]
η	over potential, $[V]$
Γ	Butler-Volmer coefficient, [-]
γ_θ	surface tension of water, $[kg \cdot m^{-1} \cdot s^{-1}]$

λ_l^*	membrane water content equilibrated with liquid water, [-]
λ_v^*	membrane water content equilibrated with water vapour, [-]
λ_w	water content(mole of H_2O/mole of SO_3^-), [-]
μ	dynamic viscosity of fluid, $[kg \cdot m^{-1} \cdot s^{-1}]$
Ω_i	boundary i
$\Omega_{\mathscr{D},AB}$	dimensionless function for a binary diffusivity, [-]
ϕ_L	Thiele's modulus, [-]
ϕ_m	protonic potential in membrane phase, [V]
ϕ_s	electronic potential in solid matrix, [V]
ρ_C	charge density, $[C \cdot m^{-3}]$
σ	conductivity, $[S \cdot m^{-1}]$
θ	contact angle, [degree]
τ	stress, $[N \cdot m^{-2}]$

Symbols & Vectors

$< Nu >$	Nusselt number averaged over the heat transferred area
$\bar{n}$	number of agglomerate per unit volume, $[m^{-3}]$
$\Im(\zeta)$	Leverette function
$\mathscr{D}_{AB}$	binary diffusivity of gas mixture A and B, $[m^2 \cdot s^{-1}]$
$\mathscr{L}_i$	volumetric mass density/momentum rate, $[kg \cdot m^{-3} \cdot s^{-1}]$
$\mathscr{M}_{i,k}$	volumatric mass rate, $[kg \cdot m^{-3} \cdot s^{-1}]$
$\mathscr{W}$	volumetric water generation/depletion, $[mol \cdot m^{-3} \cdot s^{-1}]$
Φ	electrostatic potential, [V]
$\triangle G^0$	Standard Gibb's free energy $[J \cdot mol^{-1}]$
$\mathbf{I}$	total current, $[A \cdot m^{-2}]$
$\mathbf{J}$	Jacobian matrix

$\mathbf{q}$	heat flux density, $[J \cdot m^{-2} \cdot s^{-1}]$
$\mathbf{u}$	mass averaged velocity, $[m \cdot s^{-1}]$
$\mathbf{N_D}$	diffusion flux, $[mol \cdot m^{-2} \cdot s^{-1}]$
ζ	saturation variable
A'	frequency factor, [-]
Q_M	volumetric energy generation/depletion rate, $[J \cdot m^{-3} \cdot s^{-1}]$

Superscripts

$\circ$	standard condition
eff	effective value

Subscripts

β	phase β
$_{eq}$	equilibrium
e	electron
EOD	electro-osmotic drag
k	domain k
m	membrane or electrolyte phase
s	solid phase
a	anode
amb	ambient condition
b	backward
c	cathode
f	forward

Acknowledgements

I am gratefully thankful to my supervisor, Dr. Ned Djilali, for the opportunity to be part of his research group and for his support and encouragement throughout my graduate studies and I would like to acknowledge Drs. Krissanapong Kirtikara, Apichai and Supaporn Therdtienwong of King Mongkut University of Technology Thonburi, Thailand and Ged McLean of Angstrom Power for inspiring me to pursue my PhD at the University of Victoria. I am truly thankful to Drs. Zuomin Dong, Ashoka Bhat and Andrew Rowe, my thesis committee members, for their support and time to review my thesis. I also wish to express my deepest appreciation to Dr. Akeel Shah for his time as my external examiner and for reviewing my research.

For financial support, I am grateful to the National Energy Policy Office, Ministry of Energy of the Royal Thai government for fully funding the four-year scholarship. Financial support from Anand-UVic Fund is gratefully acknowledged. I am also indebted to Dr. Ned Djilali for providing me with additional financial support.

The following research fellows and former PhD students of Computational Fuel Cell Engineering group, the Institute for Integrated Energy Systems (IESVic) of Uni-

versity of Victoria, deserve special acknowledgement: Dr. Pang-Chieh (Jay) Sui always gave me valuable support, discussions and friendly encouragement. Dr. Marc Secanell Gallart (IFCT-NRC, Vancouver) provided fruitful collaboration on the validation of simulation and was also my brain sharpener. Drs. Viatcheslav Berejnov, Jingwei Hu, Te-Chun Wu for the supporting discussions during my research work. Thank you to Dr. Aimy Bazylak for her enthusiasm and suggestions on my writing.

Without Dorothy Burrows, Susan Walton, Peggy White, Barry Kent, Arthur Makosinski, Douglas Kim Thompson and Erin Robinson, my life at UVic would not be as smooth as it has been and therefore I would like to take this opportunity to thank all of you for your kind help and friendship. I would also like to gratefully thank Dr. David Sanborn Scott for his special friendship.

My successful study would never been achieved without all the folks at School of Energy, Environment and Materials, and at Clean Energy Systems Group at King Mongkut University of Technology Thonburi who worked harder to cover my load, in particular Ajarn Chaya Jivacate, Terry Commins and Dr. Dhirayut Chenvidhya. Your great support is greatly appriciated.

I would like to express my most sincere thanks to my parents, Chatree and Khanit Songprakorp. Without you and your unconditional love you give me, this would never have been happened. I am also gratefully thankful to my brother, sister and sisters-in-law, Jirat, Hattaya, Penkhae Songprakorp and Thaneeya Na Nakorn, whom I left behind to care our parents while I pursued my doctorate degree in Canada. This,

again, would have not been possible without your help.

My special thanks to our extended family, Arthur, Rita and the Hobbs, who have given me the sentimental support and family-like atmosphere since my first day in Canada. I am gratefully thankful to John and Veronica Frey for their kind support during our stay in Canada. With their great effort, we have learnt how to speak English. Special thanks to special people and good friends, Matthew, Audrey, Claire and Charlotte Takoski for your great support and friendship and fun times during the past years. I am also grateful to Nattanon(Chai) Rutvanee for his support and brother-like friendship.

Last but not least, I would like to express my deeply thank to my wife, Aumawan Songprakorp, for her unconditional emotional support, patience and devotion as she gave up her great permanent job to come to stay with me in Canada. Thank you very much Moo for all your love, your support and understanding, especially over the last two years that you had been working hard to keep our life comfortable.

In loving memory of my grandparents, in particular Khun Yaai Ruen Intrachan, whose love and courage is always with me to fulfill her last dream.

To my family, my teachers and Davesh Jeet Grewal

Chapter 1

Introduction

1.1 Fuel Cells and Clean Energy Technology

Available conventional energy sources such as crude oil and natural gas have been exploited, extracted and refined to serve a dramatic growth of world population since 1970's. Referring to International Energy Agency's report [1], the world energy demand projection for the year of 2030 is of one and a half of the amount of current consumption which is estimated to be 700 Quadrillion BTU. This is equivalent to 31,500 million tons of coal, or 700 trillion cubic feet of natural gas, or 84,000 million barrels of crude oil. With this energy use rate, oil and other fossil fuels are reaching close to naturally discharge limitation, in other words, depletion. Having relied too heavily on fossil fuels, the consequences have come in terms of unsecured energy supplies and pollution. Many analysts argue that oil "crises"and fluctuations of crude

oil price corresponding to high demands in energy as well as global political issues impact for example of energy security. The other major issue is of course climate change; the combustion of hydrocarbon fuels remains non-desirable carbon emissions cause Green House gas phenomena (GHG); contributing to global warming (cooling).

Although renewable energy, for examples, hydro, wind, solar, tidal and ocean waves have been harvested and transformed to be usable energy, mechanical and thermal energy, the large efforts in research and development in renewable energy technologies have been established not longer than three decades ago back in 1970's, following the oil supply crisis. The main obstacles to substituting these alternatives for conventional energy sources like oil and petroleum products lie in their lower reliability (including unpredictability and fluctuations), low concentration and costly implementation. Wind energy, for instance, is available in specific areas depending upon geographical locations and it is neither uniform nor steady. In tropical regions, solar energy has the enormous potential to be a major local energy source but it needs large open areas and deployment of costly photovoltaic arrays.

In spite of these challenges and issues, there has been a growing interest in renewable energy technologies worldwide. Furthermore, these energy sources are replenished continuously (i.e. renewable) and hence, enhance energy supply security. There is increasing emphasis on "quality of life"issues, such as air quality and the environment. These concerns will demand a better and cleaner energy than the conventional environmental-pollution hydrocarbon fuels. These driving forces have increased ef-

forts around the world in seeking new power sources and energy technologies.

Hydrogen is a clean fuel, can in principle be produced abundantly and is relatively safe [2–6]. It can be produced from many kinds of energy sources whereas gasoline is refined from crude oil only. Even though hydrogen gas has less volumetric energy density than gasoline, it is possible to increase the energy density by storage in either gaseous, liquid or solid forms (e.g. metal hydrides). Like gasoline, hydrogen can be used as a fuel in Internal Combustion Engines (ICEs). To generate electrical energy directly, however, this energy currency needs a specific energy technology such as a fuel cell.

To illustrate the role of hydrogen in the context of an energy sources to services chain, Figure 1.1(modified from [7]) provides a conceptual comparison of using hydrogen and gasoline for land transportation and mobile applications. On the energy sector side, it is obvious that hydrogen fuel has more choices of primary energy sources and a flexibility in using various transformer technologies. Moreover, from a service point of view, hydrogen not only has no emissions, but also can meet a variety of services in conjunction with fuel cells and, therefore, these advantages make hydrogen in association with fuel cells a prime candidate as a future energy currency. A fuel cell is a power source which efficiently converts a chemical energy to electricity via redox reactions of hydrogen and oxygen gases and releases water as a by-product. Its

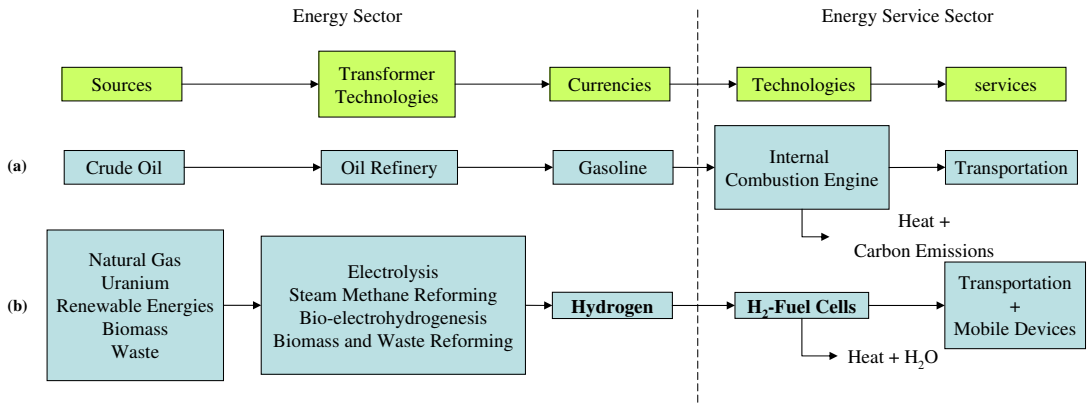

Figure 1.1: Service delivery chain using fuel cell with hydrogen as an energy currency

simple chemical reactions can be written as

$$H_2 \rightarrow 2H^+ + 2e^- \tag{1.1}$$

$$O_2 + 4H^+ + 4e^- \rightarrow 2H_2O \tag{1.2}$$

$$H_2 + \frac{1}{2}O_2 \rightleftharpoons H_2O \tag{1.3}$$

In general, given their electrochemical nature, fuel cells have many of the characteristics of rechargeable batteries. However, a key distinguishing feature between fuel cells and rechargeable batteries is that a fuel cell transforms its fuel directly into electrical power and produces power as long as the fuel is supplied. On the other hand, batteries are energy storage devices that release power until the chemical reactants stored in the battery are depleted; a battery must then be recharged. This is one of the advantages of fuel cell over battery that pushes hydrogen fuel cells further

towards a promising zero local emission technology which potentially fits in numerous applications where battery are not viable. Since batteries have reached close to their maximum capabilities, a power gap already exists between today ever-increasing power demands of applications and the energy densities of present batteries.

Among the various types of fuel cell, particularly in small and medium-sized power systems, proton exchange membrane fuel cells (PEMFCs), also named polymer electrolyte membrane fuel cells as it employs a polymer membrane as a gas separator and proton facilitators, are prime candidates for vehicular applications [8, 9] and portable consumer electronics, due to their advantage of low operating temperature, good power density, and excellent energy conversion efficiency compared to ICEs.

Using hydrogen fuel cells in mobile applications such as portable devices, power packs and automobiles one can potentially encounter problems, namely size and weight considerations, and unsteady power delivery. Due to a limitation of space and weight in such applications, the fuel cell's peripheral components (e.g. fuel and oxidant tanks, humidifiers, cooling system) need to be relatively small compared to the size of the devices, so that they can be integrated into a system. An example of the possible solutions to this problem is an air breathing fuel cell. It can be operated on atmospheric air to supply the oxidant; hence, the oxygen tank and its humidifier can be eliminated. Operation under such open conditions, however, makes it difficult to regulate the intakes of gas and air into fuel cell. Dynamic processes (i.e. transports of gases and charges) inside each component of the fuel cell will play an importance role

in generating power, and performance will be strongly dependent upon the changing environments.

In start-up and shut-down processes, a step change in current can have a large impact. In this situation the reactions can take place quasi-instantaneously at the reaction sides with time scales less than 0.1 second [10], whereas thermal transport process takes several seconds to minutes [11]. Accordingly, the difference in these time scales will result in a dynamic behaviour that can strongly affect the performance of the fuel cell. These transient and dynamic effects can eventually induce performance degradation. In practical operations, power sources have to be fast enough to respond to changes of operating conditions as well as duty loads, otherwise an auxiliary power source is needed and, hence, an additional cost is incurred. To overcome this problem, it is essential to understand how and under what conditions the transients would be present. Systematic solutions can then be established.

The commercialization of PEM fuel cells faces the challenge of prohibitively high cost. Moreover, the above technical issues need in-depth understanding to be able to devise adequate solutions for improving the commercially viability. The need to improve the performance of fuel cells by better design and materials development and enhancing capability for production at a reasonable cost are some of the main objectives of ongoing fuel cell research. There are two approaches to do so: to design and build prototype cells, and experimentally evaluate performance, and to simulate by use of modeling. The first approach yields useful and physically representative

information but is costly and time consuming. It is difficult to evaluate (*in situ*) such processes as membrane water-transport and electrochemical reaction, due to the limitations of available experimental techniques. Modeling can provide deeper insights into these phenomena at a lesser cost and a faster turnaround time. In practice, it is essential to combine experimental prototyping and simulations to achieve the optimal design cycle.

1.2 Literature on the Dynamics of PEMFCs

Numerous modelling and experimental studies regarding the transient and dynamic behaviour of PEM fuel cells have been reported in the open literature. Current-voltage characteristics, for example, have been examined along with the undershoot and overshoot phenomena occurring in fuel cells when subjected to abrupt change in load during start up or shut down. The effects of operating parameters and conditions such as pressure, temperature, humidity and gas composition have been investigated both experimentally and numerically. Since water is a byproduct of the oxygen reduction reaction in a fuel cell cathode, there is a rich literature on water management. In the following subsections, an overview of the literature, focusing on studies of the dynamic behaviour of a fuel cell and related issues, is presented.

1.2.1 Experimental approach

The performance characteristics of a proton exchange membrane fuel cell are typically reported in the form of a current-voltage plot. These plots can provide indirect monitoring of some of the phenomena responsible for losses, such as mass transport limitations, water flooding and membrane dehydration. The I-V curves, however, might have a similar shape even though the phenomena are different. In the work of William et al. [12], for example, a similar sharp drop in cell performance was shown for both membrane dehydration and mass transport limitations. The data are mostly obtained from steady state testing conditions (e.g., slowly increase potential or step change with a resting time to allow systems to reach a new steady state before proceeding to the next step). On the other hand, in practical operation, current-voltage and other system performance characteristics are dynamic and may not attain steady state or equilibrium values. A current-voltage plot of a system in unsteady conditions will in general differ from that at steady state.

The dynamic behaviour of a fuel cell in terms of an overshoot and undershoot of current when it is operated under sudden load changes, as well as under dilute fuel, has been studied experimentally by Kim and co-workers [13, 14]. The stoichiometric ratio of the fuel was found to influence the response of the system, and in particular a drop in the undershoot current was observed when feeding the fuel cell with dilute fuel. Additionally, control of the fuel outlet conditions such as back pressure was found to reduce the peak time length of overshoot current. With respect to overshoot

and undershoot, their results generally exhibited the same trends as those reported in [15–18].

Attempts to reduce the cost of balance of plant and the complexity of fuel cell systems have been undertaken in a number of ways that can potentially alter the dynamics. Running fuel cells under dry conditions (by feeding low or unhumidified oxygen and/or hydrogen), for example, will eliminate gas humidifiers from the system. Fuel cells under dry gas operation have been also investigated in attempts to improve water management in the membrane [18, 19]. Yu et al. [20] have experimentally investigated the effects of dry gas on the dynamic response of a fuel cell.

Another dynamic phenomenon investigated experimentally is hysteresis [19–21] which is observed during transient load when changing the direction of potential sweeping. Their works showed that water content in the membrane is responsible for this phenomenon. It should be noted that in Yu et al. [20] the results unveil the crossing points of current-voltage curves between forward and backward sweeps in both poteniostatic and galvanostatic modes and occurred only under dry operation. Those thresholds and the phenomena were explained in terms of dynamic equilibrium state of the MEA.

In a PEM fuel cell, a polymer membrane (e.g. Nafion®, Gore-Tex™), is used as a proton conductor and a permeation barrier for the reactants. The membrane is an effective proton conductor when hydrated. However, conductivity drops dramatically when the membrane has low water content [22–24] for typical membranes such as

Nafion. Many contributions have been made in attempts to characterize membrane properties and develop new membranes. According to polymer membrane studies [16, 24–29], it is evident that water transport plays a crucial role in the dynamic response of a fuel cell. Benziger et al. [16] observed the transient phenomena in terms of current response of fuel cell at various water contents. Ye et al. [30] have found that the water permeability of Nafion membranes is dependent on the partial pressure of water vapor, and the local thermodynamic diffusion coefficient determined from the water permeability is at a maximum when the membrane has a water content of around 3.3. Krtil et al. [31] experimentally evaluated the water sorption rate of a cast Nafion film exposed to water vapor using micro balance techniques to measure the mass change of water. The results show that the water desorption rate is five times higher than the sorption rate and the slow swelling process is a cause of a faster water release from the ion cluster. Ge et al. [32] have experimentally studied the water transport process for a Nafion membrane in contact with water vapor and liquid forms, and concluded that for a membrane in contact with water vapor, the electro-osmotic drag coefficient increases with increasing water content, independently of temperature when water activities at the anode and cathode are equal, whereas a linear dependence on temperature exists when the membrane is in contact with liquid water. More recently, Majsztrik et al. [29] have experimentally investigated the sorption/desorption and transport processes of water in and through various models of Nafion membrane in the temperature range from 30°C to 90°C. They conclude that

the rate of membrane swelling limits the water sorption rate. In particular, water desorption is limited by the rate of water transport across an interface between the membrane and gas phases. Takata et al. [33] have studied the adsorption properties of water vapor on sulfonated perfluoropolymer membranes and found that the amount of clustered water is closely related to the proton conductivity of the membrane. Another interesting issue regarding water transport in fuel cells, particularly when operated in dynamic mode, is the non-equilibrium state of the water phase at the membrane/gas interface. The dynamics of water generated and transported in the vicinity of the catalyst layer was studied by Zhang et.al [34]. In this experimental work, the dynamics of micro droplets on the catalyst surface were monitored. Voltage oscillations at high current density were attributed to catalyst layer flooding. They conclude that the net water transport coefficient used in water management calculations is in fact a dynamic variable rather than a constant.

At a system level, Yan et al. [17] have thoroughly examined the transient response of H_2/air PEM fuel cells under a variety of loading cycles and operation conditions. The general findings include that the cathode humidity level, operating temperature and air stoichiometric flow rate strongly influence fuel cell performance. Performance is affected directly by a limited oxygen supply and indirectly by variations in humidity in the cathode feed gas, as well as water flooding.

Unlike the experimental works mentioned above, Weydahl et al. [35] have studied the dynamic behaviors of a PEMFC supplied with pure hydrogen and oxygen, with

transient resolution of the order of sub-seconds. Based on electrochemical impedance spectroscopy, chronoamperometry and an electrical model, their results show that the response times of the charge transfer process in a fuel cell are in range of 0.38 to 1.6 ms when stepping pure resistance load to lower values.

Due to the advantages of a reduced number of components and a simpler configuration, air-breathing fuel cells have gained increasing interest. There are many publications reporting on the status and performance of this type of PEMFC [36–39]. The performance of a planar self-breathing fuel cell fabricated on a printed circuit board (PCB) has been investigated experimentally by Schmitz et al. [36]. The issues of gas diffusion thickness, the opening ratios and operating temperature have been investigated. The results shows that a thicker gas diffusion layer is preferable to a thinner layer as flooding can easily occur in the latter. In relation to the operating temperature, optimal performance was observed in the range of 35-40°C with opening ratios of between 60 and 80%. Fabian et al. [38] examined the performance of a $3cm^2$ air breathing fuel cell with a dead-ended anode under various operating temperatures. In their work, a potential sweep with varying resting time interval to reach a new steady state was used. Shadowgraph visualization was employed to investigate the temperature profiles of the fuel cell. A similar experimental work on air-breathing PEMFCs has also conducted by Jeong et al. [40, 41], who focused on the performance of a fuel cell cathode under different platinum loadings, gas diffusion layer structures and humidity ratios. The cell resistance was measured using impedance spectroscopy,

thus providing more details than the aforementioned work.

In addition to the work on the dynamic response of PEMFCs, many contributions have been made to a Direct Methanol fuel cell (DMFC) [42–46]. Argyropoulos et al. [42,47] showed that methanol feed concentration, feed rate and air pressure under dynamic load affects the voltage response of the fuel cell. In their experiments, the load cycle was employed to study the effects of load history.

As noted earlier, the problems related to dynamic phenomena cannot be resolved solely with an experimental approach. Experimental characterization of these dynamic phenomena has limitations: high cost and long times. Numerical investigations using mathematical models based on conservation principles can complement experiments and have advantages in terms of cost and time, and provides insights into and understanding of phenomena that cannot be observed experimentally. The next subsection provides a concise review of existing works related to dynamic fuel cell modeling.

1.2.2 Modeling approach

To date, a large number of mathematical models of PEM fuel cell systems have been developed. These cover various aspects: multi-dimensionality [48, 49], domains [50, 51], operating conditions [18, 52, 53], heat and water management [54, 55], control scheme [13, 14, 56] and so on. Good reviews on steady-state fuel cell modeling up to 2004 include [57–60].

Dynamic fuel cell models have, on the other hand, mostly appeared in the past 5 years in the open literature. The earlier work of Amphlett et al. [61] was based on a one-dimensional steady-state electrochemical model in which both heat and mass transfer transient features are coupled with empirical sub-models to predict the transient response of a Ballard fuel cell stack. Subsequently, the performance of the Ballard MK5-E stack under fast load was modelled by Hamelin et al. [21]. The polarization curve was modeled experimentally and the coefficients used in this model were based on Kim et al. [62]. The model predicted well the behaviour of the fuel cell under various stack temperatures and over a range of low to medium current densities. The response of the fuel cell to a step-up load change was reported to be less than 0.15 seconds compared to 10 micro-seconds for the characteristic electrochemical reaction time.

More recently, studies of the dynamic behaviour of fuel cells have focused on start-up and shut-down conditions as well as sudden changes of load [13–15, 52, 63–66], as in automotive applications [56, 67]. Some studies have focused on water management in the membrane-electrode assembly (MEA) [20, 68–70]. In addition, there are several dynamic models for Direct Methanol Fuel Cells (DMFCs) [43, 44, 71, 72].

Theoretical models, accounting for heat and mass transfer, water transport and some transient phenomena in a single cell has been developed by Wöhr et al. [73] and Bevers et al. [74]. The model region is subdivided into three zones: diffusion layer, catalyst layer and membrane. Each is considered as a one-dimensional connected to

the other components *via* material and energy flux conditions at the interfaces. The dusty-gas model combining the Stefan-Maxwell equations and a model for Knudsen-diffusion (with convective transport) was used to describe gas transport within the assumed homogeneously distributed cylindrical pores of the gas diffusion layers. This model was able to predict the performance of a fuel cell stack (4 single cells) during dynamic operation by coupling a single module. The effect of increasing current density was analyzed in terms of the rate of temperature change, the water deficiency in the membrane, and voltage characteristics. Chen et al. [70] extended the one-dimensional theoretical model developed by Okada et al. [68] to investigate the unsteady-state features of water transport in the membrane, with particular emphasis on the influence of physical and operational parameters on the characteristic time for water transport across the membrane to reach a steady state.

Motivation for system simplicity led van Bussel et al. [69] to investigate various operation strategies such as operating on dry gas at low overpressure. The two-dimensional model accounts for water production, drag and diffusion in the membrane and diffusion of water vapor in the gas diffusion layers, to study water management and the effects of operating conditions on performance. The time-dependent behaviour is determined essentially by using small time step to adjust the membrane resistance based on the water balance.

A fully three-dimensional model was developed by Dutta et al. [75] to investigate the transient behaviour and performance of a fuel cell, specifically focusing on

a configuration with a triple serpentine gas flow channel. Simulation results of the transient response to variations in the amplitude and the frequency of load changes representative of the stop and start driving scenarios were presented. The model was implemented in the commercial computational fluid dynamics (CFD) package FLUENT by adding user-defined function (UDF) subroutines to account for the electrochemical reactions, as well as condensation and evaporation (phase change), and transport of water between the anode and cathode channels.

Another notable CFD based multi-dimensional model is due to Um et. al [76] who based their development on a CFD formulation previously used for batteries. Similarly to the work by Wöhr et al. [73], this model employed a single-domain approach in which a single set of governing equations valid for all sub-regions was used without requiring boundary conditions for each interface, except for a jump condition implemented of the catalyst-gas diffusion interface to account for a discontinuity in concentration. The transient response of current density under sudden changes of voltage was simulated. A thorough theoretically-based dynamic model and analysis of the simplifications of the electrochemical description to create a dynamic model of PEM cells were presented by Ceraolo et al. [77]. The model included a total of 22 numerical parameters determined from experiments using Nafion 115 membranes, including AC impedance measurements.

Friede et al. [15] presented experimental measurements and modeling work showing that operating conditions have a very strong influence on the electrical output of

a fuel cell. Two major phenomena were distinguished experimentally: the humidity of the membrane and the flooding and dry out of the electrodes. The effects of those phenomena on the fuel cell performance have a time constant of several seconds and can be observed by a measurement of the ohmic resistance of the fuel cell. Longer time constants can be observed for the flooding of the cell due to liquid water accumulation in the electrodes. These time constants can reach several minutes, and have to be considered when planning an efficient control system. Modeling in this work did not, however, consider electrode flooding and drying.

Following the experimental work of [20], Ziegler et al. [78] developed a dynamic isothermal two-phase model of PEMFC incorporating the membrane model proposed by Weber [79]. This model was shown to be capable of capturing the hysteresis of current-voltage of the cell under potential and current sweeps even though the predictions differ quantitatively from the validation data.

Shah et al. [80] developed a transient non-isothermal model of a fuel cell MEA accounting for liquid water transport. The model included micro-porous layers used to reduce flooding in the gas diffusion media. The catalyst layer was represented using an agglomerate kinetics model. The model is capable of predicting dynamic accumulation of liquid water in cathode gas diffusion layer and successfully reproduces the current-voltage hysteresis which will be discussed in more detail later on in this thesis. As with most theoretical studies of transient, the simulations performed with the model are 1D. An important feature of the model is that it accounts for different

water states, as well as membrane adsorption and desorption rates that are functions of hydration. However, the effect of temperature on the time constant for water to reach an equilibrium is not accounted for. The importance of water management in fuel cells has led to numerous steady state studies on water transport, flooding and management schemes. Regardless of the operating mode, modelling water transport in fuel cells requires transport parameters and coefficients which can be obtained from steady state experiments as discussed in the previous section. The followings summarizes relevant modeling work on water transport.

Moltupally et al. [25] developed a set of equations to predict the water diffusion flux across a Nafion 115 membrane using Fickian diffusion coefficients obtained from a self-diffusion measurement. Ge et al. [27] studied the transport of water vapor as well as liquid through a Nafion membrane. The model included non-equilibrium water uptake in terms of the mass-transfer coefficients for the absorption and desorption of water and water diffusion. The main conclusion was that the mass-transfer coefficient for the absorption of water is much lower than that for the desorption of water. These results are consistent with the experiment on water permeation and diffusion of Majsztrik et al. [29], in which water sorption, desorption, and permeation in and through Nafion membranes were measured as functions of temperature. Water permeation was found to be limited by inter facial mass transport across the membrane/gas interface for thin membranes and at low temperature. At higher temperatures and with thicker membranes the diffusional resistance across the membrane

becomes important for water permeation. Majsztrik et al. also pointed out that there is a difference in the rate of permeation between liquid and water equilibrated Nafion. In addition, water desorption from saturated membranes is limited by the inter facial mass transport resistance at the membrane/gas interface. Water sorption from humidified gas is limited by the rate of swelling of the polymer membrane to accommodate the water. In this work a shrinking core model has been proposed to describe water sorption into Nafion.

Wu et al. [53,81] developed a 2-dimensional, non-isothermal transient model which accounts for the effect of an electric double layer. The liquid saturation is fixed. Shan et al. [82,83] proposed a dynamic fuel cell model accounting for dynamic temperature distributions across the fuel cell, water concentration redistribution in the membrane, dynamic proton concentration in the cathode catalyst layer and dynamic reactant concentration redistribution in the cathode GDL. In both modeling works, Springer's water transport formulation [84] is used.

Recently, Vorobev et al. [85] have proposed a one-dimensional isothermal model of a low-humidity non-steady operation of a PEM fuel cell with a linear model to represent the equilibration process. The main difference with similar models is that they determine the transition time between the two phases as a finite-rate equilibration process instead of using the isotherm water equilibrium curve. It implies a finite time to reach new equilibrium state, with values ranging from 0.1 to 100 which equivalent to time constant in range of 8.8×10^{-5} - 8.8×10^{-2} seconds. They mentioned the

importance of the finite rate equilibration within the catalyst layers for the processes of water transport in PEM fuel cells, the non-steady mode in particular. In a system point of view, few papers address the effects of transient variations in the fuel cell system performance. Most of them contribute model-based control methodology. Some of those are reviewed as follows. [56, 86, 87]

Pukruspan et al. [56] developed a control-oriented fuel cell system model using physical principles and stack polarization data. The inertia dynamics of the compressor, manifold filling dynamics and time-evolving mass of reactant, humidity and partial pressure, and membrane water content are captured. This model has not been fully validated but it reflects extensive work to consolidate the open-literature information currently available. Transient experimental data, once available, can be used to calibrate the model parameters such as membrane diffusion and osmotic drag coefficient. Additionally, stack flooding effects are not taken into account in this model. Yerramalla et al. [67] developed a mathematical model based on mass, energy and electrochemical reactions: Nernst and Tafel equations. The model accounts for polarization due to current leakage between single cells. The model can be executed as either a linear model or non linear model to study the transient behaviour of a single cell, with the response of the fuel cell stack obtained simply by multiplying a single cell output by the numbers of cells. The main interest was the transient effects of the inverter on fuel cell performance. Alternative approaches to modeling the dynamic behaviour of fuel cells are empirical, such as the model proposed by Garnier

et al. [87] for automotive applications. The model is based on the measurement of the electrochemical impedance of a single cell. Then, by means of an appropriated transfer function the electrical circuit equivalent to a fuel cell is obtained. This approach needs some measurement of a polarization curve and an impedance spectrum without knowledge of the internal geometry of the cell stack.

1.3 Problem Statement

In the previous section, the problems regarding transient phenomena and dynamics in fuel cell have been discussed. Although some particular problems have already been addressed there are at least two issues which have not extensively been investigated: the effect of a non-equilibrium state of water on the fuel cell response and the dynamic behaviour of air breathing fuel cells.

1.4 Scope of Research and Objectives

This thesis focuses on numerically investigating the transients behaviour of a proton exchange membrane fuel cell operated using hydrogen and makes the contributions to the field listed below. The main goals of this thesis are to establish the parameters involved in the transient phenomena in PEMFC and, then, to develop a time-dependent, non-isothermal fuel cell model of a proton exchange membrane fuel cell:

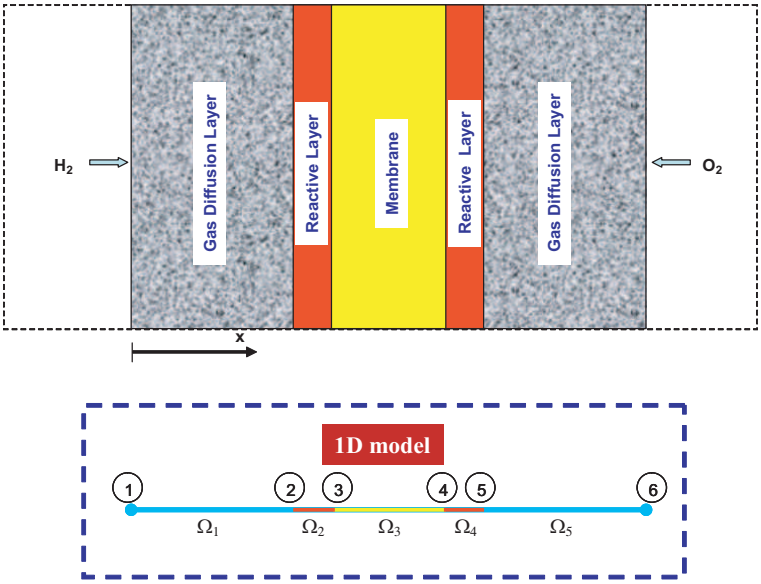

Figure 1.2: Schematic diagram of membrane electrode assembly and domains used in study

- The identification of important parameters that control transient phenomena in fuel cell.

- The development of a dynamic model based on the non-equilibrium thermodynamics of water phase change to investigate transient behaviour of fuel cells.

- Employ the developed model to examine the dynamic behaviour of air-breathing fuel cell systems and fuel cell operation strategies.

1.5 Thesis outline

The remainder of this thesis is divided into four chapters.

Chapter 2 describes key parameters which potentially cause transients and dy-

namic behaviors in a fuel cell when it is subjected to change in operating conditions. This chapter also focuses on theoretical works regarding these parameters. Chapter 3 covers the modeling framework developed and used in this study. All sub-models are developed and their implementation into the framework and validation are discussed.

The simulation data obtained from the model developed in this study are presented and discussed in chapter 4. Comparisons with existing models are conducted and, at the end of the chapter, application of the dynamic model on air-breathing fuel cell is illustrated.

Chapter 5 summarizes the works presented in this thesis and the main findings and suggest future research directions.

Chapter 2

Fundamentals of Fuel Cell

In this chapter the basic components of a fuel cell and their function are briefly discussed. The concept of a spatial averaged volume is introduced followed, in section 2.2, by a description of the main physical processes occurring in a fuel cell and the corresponding general governing equations used in the mathematical framework for the fuel cell model in this thesis. The processes and equation includes the kinetics of electrochemical reactions in the fuel cell based on the Butler-Volmer formulation, the charge transport equations for electrons and protons in the MEA using Ohm's law, the gas flux expressions based on Fickian diffusion approach and mass conservation and continuity, and the heat equation. Three basic water transport mechanisms and the general multiphase flow equations are also discussed. The assumptions associated with the mathematical models in each component are discussed. The last part of the chapter is devoted to an analysis of parameters which dominate transients and

dynamic phenomena occurring in PEMFCs, in particular when the fuel cell is operated under varying operating conditions.

2.1 Fuel Cell Structure and Physical Parameters

Figure 2.1 illustrates a typical design of PEMFC and a simplified schematic in a 2-dimensional view. A single cell (or unit cell) consists of the assembly of two main parts: bipolar plate and a membrane electrode assembly (MEA). The MEA consists five layers: anode gas diffusion, anode catalyst, membrane, cathode catalyst and cathode gas diffusion. The bipolar plates are made of metal or a conductive polymer (e.g., carbon-based composite which increases toughness over graphite and better conductivity than polymers). Their main functions include conduction of electric current and providing a flow field channel for the distribution of reaction gases. The bipolar plate also provide a support structure for the stack, separate reactant gases between cells and contribute to transport heat out of the cell. The plates usually have flow channels for the reactants feed which connect to gas manifolds on each side. In some designs, cooling channels are also embedded in the bipolar plates for enhancing the heat transfer. As the main focus of this study is on the phenomena inside the MEA, the bipolar plates are not explicitly considered, instead they are treated as boundaries.

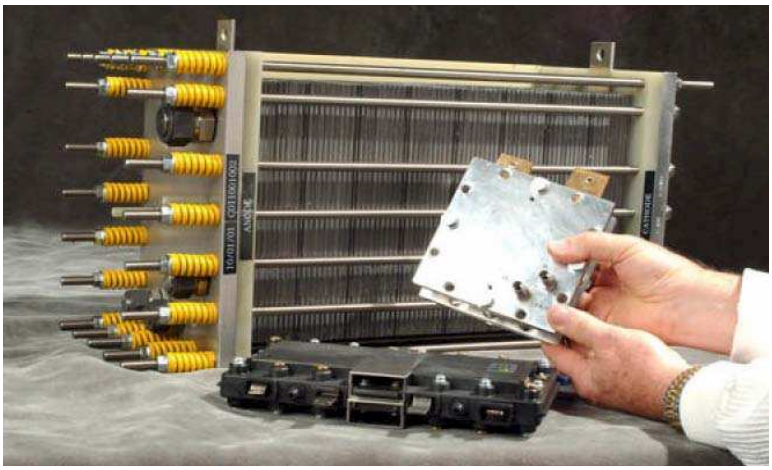

(a) PEMFC stack design (Courtesy of National Renewable Energy Laboratory, NREL, USA)

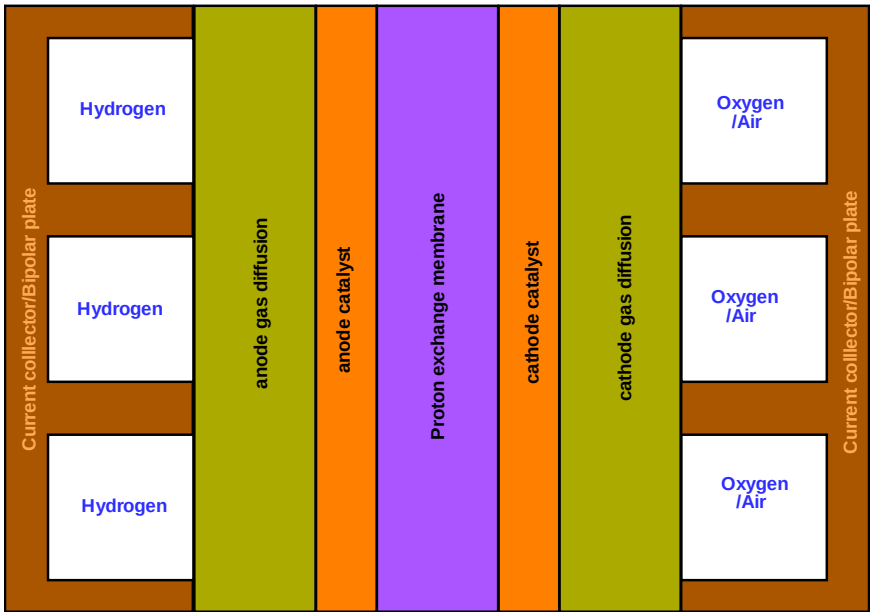

(b) Schematic of cross-sectioned cell

Figure 2.1: (a) Depiction of PEM fuel cell stack design from NREL and (b) 2-dimensional schematic cross-section of a single cell

2.1.1 Membrane electrode assembly

Gas diffusion layers

Generally, the gas diffusion layers (GDLs) are made of a porous material such as carbon cloth, carbon or woven paper, or metal wire mesh [88,89]. Gases can permeate through the GDL to the reaction site, primarily via diffusion but also by convection if a pressure gradient is present. The GDL also conducts electrons from the catalyst layer to the current collector plates. In addition, heat generated at the catalyst layers will be transferred mainly by conduction to the bipolar plates and by convection in gas phases to the gas flow channels. The GDL material is typically treated with a hydrophobic material, such as Teflon, to facilitate liquid water removal. The physical characteristics of the GDL, such as the porosity and tortuosity, can have a significant impact on the transport of reactants as well as on overall cell performance [90–92].

In summary, the gas diffusion layers (GDLs) perform the following functions

- to uniformly distribute hydrogen and oxidant (oxygen or air) to reaction sites
- to provide pathways for electrons to/from the external circuit
- to transfer heat from inside the cell
- to structurally support the thin catalyst layers
- to serve as a drainage path for liquid water into the gas flow channels

Catalyst layers

In low temperature fuel cells, due to the high activation energy needed to induce the electrochemical reactions, a catalyst, such as platinum, is required. Practically, the catalyst is prepared by mixing a small amount of Pt with carbon particles and proton-conducting ionomer, and then applying the solution onto both sides of a membrane electrolyte by either spraying or painting. In the catalyst layers, the reduction reaction in Equation 1.1 occurs in the anode side and hydrogen is oxidized releasing protons and electrons, while in the cathode side the oxidation reaction (Equation1.2) takes place as the reduced oxygen molecules combine with protons from electrolyte and electrons from the external circuit, water is generated as a product of reaction via equation 1.3.

Polymer electrolyte membrane

The primary function of the polymer electrolyte membrane (PEM) is conduction of ions, but it also serves as a separator between the reactant gases, and as an electronic insulator. Functional membranes must also have sufficient mechanical and thermal stability. PEMs consist of microphase-separated structures (see Kreuer et al. [93]), comprising hydrophobic polymer chains (perfluorosulfonated ionomer) and hydrophilic sulfonic acid groups. Ionic conductivity of a PEM, which is crucial to the efficient operation of a PEMFC, is strongly dependent on hydration. The hydration is expressed in terms of λ, the number of sorbed waters per sulfonate head. Water content, and in turn ionic conductivity, is determined by the balance of various wa-

ter transport mechanisms that include diffusion and electro-osmotic drag (EOD)-the mechanism whereby water molecules associated with a proton are "dragged"with the proton migrating from anode to cathode.

In PEMFC applications, there are two main types of polymer membranes being studied: perfluorosulfonic acid membranes such as Nafion and Gore-Tex membranes and sulfonated aromatic polymers (e.g. sulfonated polyetherketone, SPEEK and polyetherketone, SPEK).

Nafion®, DoPont, has been widely used and is currently the industry benchmark thanks to its main are high chemical and mechanical stability, high ion-exchange capacity and high exchange rate [94]. This membrane exhibits phase separated domains consisting of an extremely hydrophobic backbone which gives morphological stability and extremely hydrophilic functional groups. These functional groups aggregate to form hydrophilic pores which act as water reservoirs [95, 96].

Conventional PEMFCs typically operate with Nafion membranes, which offers quite good performance below 90°C. Ongoing efforts in developing high temperature membrane (e.g. over 90°C) are aimed at improving the performance, efficiency and CO-tolerance of the PEMFC system.

2.1.2 Representative elementary volume and volume fraction definition

The morphology of the porous materials in an MEA is not directly represented in this work, but rather modelled using a continuum approach. Following [97], all porous media in this work (e.g., GDLs and CTLs) are treated using the spatial approach in which a macroscopic variable is defined over a sufficiently large volume called representative elementary volume (R.E.V). This approach averages and simplifies a microstructure and provides a homogeneous macroscopic view of the volume. Figure 2.2(a) and (b) illustrate the REV in which the dark elements represent a solid phase and the rest is void space (pore) and a simplified unit square in which a ratio of a solid and void area corresponds to the one in (a). Referring to Figure 2.2(b), the porosity, ϵ, of a dry porous media defined as the fraction of the total volume occupied by void space and a 1-ϵ represents the fraction of solid volume. For porous media like the GDLs in which the void space may be occupied by multi-phases (e.g., gaseous, vapour and liquid water), the bulk porosity will consist of the gas ϵ_g and liquid ϵ_l volume fractions. The volume fractions are related by

$$\begin{aligned} \epsilon_s + \epsilon_l + \epsilon_g &= 1 \\ \epsilon_l + \epsilon_g &= \epsilon \end{aligned} \tag{2.1}$$

More details of the REV approach can be obtained from [97, 98].

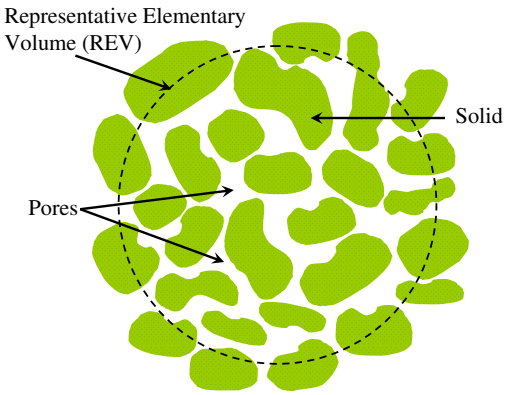

(a) Representative elementary volume (REV)

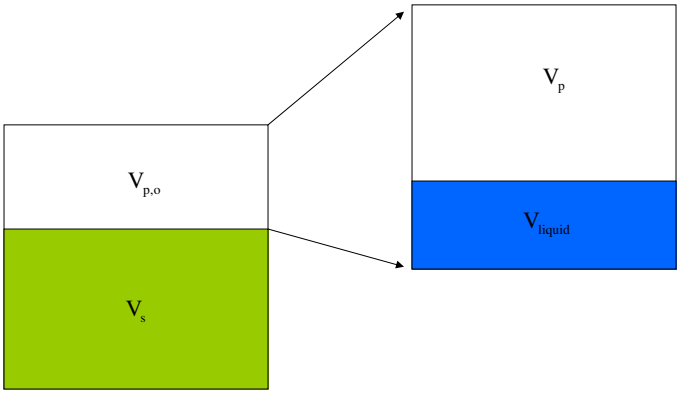

(b) Volumes occupied by solid, primary pores and liquid in REV

Figure 2.2: (a) A representative elementary volume (REV) used in the study as a porous midea flow domain and (b) Schematic volumes occupied by solid, primary pores and liquid

2.2 Transport Processes in PEMFCs

For a better understanding of processes happening dynamically in the fuel cell and the occurrence of spontaneous oscillations in electrochemical and hydrodynamic systems, the mathematical descriptions and theoretical basis of the processes are discussed.

In the derivation of the transport equations, a representative elementary volume element (REV) in a bulk phase (section 2.1.2) is employed together with the following assumptions.

- The continuum approach is used, in which the REV is assumed to be constant in space and time.
- The volume fractions of gases in the REV will change according to presence of liquid water.
- Throughout this study, the solid volume fraction is kept constant.

2.2.1 Kinetics reactions

The anode and cathode have each a potential - a half-cell potential difference - when compared to the reference electrode such as the Hydrogen Reference Electrode (HRE). On the anode electrode, at the standard condition, the hydrogen oxidation reaction takes place and the standard half-cell potential of the reaction is E_a°. Similarly, the cathode electrode, the oxygen reduction reaction has the potential E_c°. This potential

difference is called the standard half-cell potential of the electrodes, E°_{cell}, the driving force for the fuel cell to produce electrical work:

$$E^{\circ}_{cell} = E^{\circ}_{c} - E^{\circ}_{a} \tag{2.2}$$

Theoretically, the chemical reaction proceeds toward its equilibrium, and the electrical work done by the fuel cell can be related to the change of Gibb's free energy, $\triangle G^{\circ}$ as

$$\triangle G^{\circ} = -nFE^{\circ}_{cell} \tag{2.3}$$

To further derive an expression for the relation between cell potential and concentration of reactants at the conditions which deviates from the standard one, a general electrochemical reaction is considered:

$$S_{ox} + ne^{-} \rightleftharpoons S_{red} \tag{2.4}$$

The net reaction rate of the above reaction is

$$v_{net} = v_f - v_b = k_f C_{ox}(0,t) - k_b C_{red}(0,t) \tag{2.5}$$

where v and k are a reaction rate and a rate constant. Subscripts f and b denote the forward and backward process. $C(0,t)$ represents the concentration of species at the electrode surface.

At the fuel cell anode, hydrogen gas is oxidized to H^+ and releases an electron; the reaction is controlled by the surface overpotential, η. Oxygen, on the other hand, is reduced as it has a tendency to receive electron more than hydrogen in the reduction reaction. Thus the reaction rates on each side have to be compatible and can be expressed in terms of current(fluxes of electrons). The rate constant in Equation(2.5) can be described using the Arrhenius equation and potential energy surface as

$$k = A' e^{-\triangle G^\circ / R_g T} \tag{2.6}$$

Here $\triangle G^\circ$ is the standard Gibbs free energy of activation and A' is a frequency factor. Introducing a transfer coefficient, α which determines the change of activation energy of electron if the potential is changed by $\triangle E$ such as $\triangle E = E$ - E°_{eq}.

$$\begin{aligned} \triangle G_a &= \triangle G^0_a - (1-\alpha) F(E - E^\circ) \\ \triangle G_c &= \triangle G^0_c + \alpha F(E - E^\circ) \end{aligned} \tag{2.7}$$

Inserting Equation (2.3) and Equation (2.7) into Equation (2.5) yields an expression relating reaction rate, cell potential and concentration:

$$v_{net} = k^0 [C_{ox}(0,t) e^{-\alpha \frac{F}{RT}(E-E^\circ)} - C_{red}(0,t) e^{(1-\alpha)\frac{F}{RT}(E-E^\circ)}] \tag{2.8}$$

Since the reaction rate v_{net} is the molar rate at which the electrons flow through

the cell then

$$v_{net} = \frac{i}{nFA} \tag{2.9}$$

where $i = i_c - i_a$ is the total current delivered from the cell. Then Equation 2.8 can be rewritten in the form of total current as

$$i_a = \underbrace{FAk^0 C_i e^{\left(-\frac{\triangle G(0)F}{RT}\right)} e^{\left(\frac{(\alpha_i)F}{RT}\triangle\phi_{eq}\right)}}_{= i_{0,a}} e^{\left(\frac{\alpha nF}{RT}\eta\right)} \tag{2.10}$$

$$i_c = \underbrace{FAk^0 C_i e^{\left(-\frac{\triangle G(0)F}{RT}\right)} e^{\left(\frac{(\alpha_i)F}{RT}\triangle\phi_{eq}\right)}}_{= i_{0,c}} e^{\left(\frac{\alpha nF}{RT}\eta\right)} \tag{2.11}$$

where η is the surface overpotential which is the driving force, and i_o is an exchange current density.

$$\eta = E^{\circ}_{cell} - E^{\circ}_{eq} \tag{2.12}$$

The E°_{eq} is the equilibrium potential at which forward and backward rates are equal and the exchange current is defined.

$$i = i_0[exp\left(\frac{-\alpha nF}{RT}\eta\right) - exp\left(\frac{(1-\alpha)nF}{RT}\eta\right)] \tag{2.13}$$

2.2.2 Charge transport

There are two types of charges transported in a PEM fuel cell: protons and electrons. Both electron and proton transport takes place in the catalyst layer domain; only

electrons are transported in the GDL, and transport of protons takes place in the membrane. To describe the transport of charges in fuel cell the balance of charges over the REV at a given time and the potential difference defined in the previous section are applied. The resulting equation governing the transport of charges is

$$\frac{\partial}{\partial t}\rho_c + \nabla \cdot \mathbf{N}_i = 0 \tag{2.14}$$

where ρ_c is the total charge density which consists of the electrons and protons charge densities and $\mathbf{N}_i$ is the net fluxes of species i(protons and electrons).

The relationship between the electric field, $\mathbf{E}$, and the gradient in electrostatic potential, Φ, across two electrodes can be written as

$$\mathbf{E} = -\nabla\Phi \tag{2.15}$$

Using Ohm's law, the current of charged species is related to the potential gradient via

$$\mathbf{i}_{i,k} = -\sigma_{i,k}\nabla\Phi \tag{2.16}$$

where σ is the conductivity. The subscripts i and k denote the charged species (e.g., i = e for electron and p for proton) and conducting phases (e.g., s for solid phase and m for ionomer or membrane phase). The current is the net flux of charges driven by

the electric field.

$$\mathbf{i}_{i,k} = \sum_i z_i F \mathbf{N}_i \tag{2.17}$$

where $\mathbf{N}_i$ is the flux density of charged species i.

In an electrolyte, protons can move in response to an electric field, concentration gradients and bulk fluid motion. Based on the dilute solution theory, the fluxes of protons are given by the Nernst-Planck equation which reads

$$\mathbf{N}_p = -z_i u_i F c_i \nabla \Phi_i - D_i \nabla c_i + c_i \mathbf{v} \tag{2.18}$$

The first term in the equation describes the motion of charged species that results from a potential gradient, so-called migration. The migration flux is related to the potential gradient $\nabla \Phi_i$ by a charge number, z_i, concentration, c_i, and mobility, u_i. The second term relates the diffusive flux to the concentration gradient of the dissolved species. The final term is a convective term and represents the motion of the species as the bulk motion of the protons in the membrane. For the analysis of one-phase systems, the solvent is the membrane, and thus, $\mathbf{v}$ is zero. The dilute solution theory considers only the interactions between the dissolved species and the solvent, e.g., hydronium ion and ionomer. The motion of each charged species is described by its transport properties, for examples, the mobility and the diffusion coefficient which can be related to one another at infinite dilution via the Nernst-Einstein equation,

i.e.

$$u_i = \frac{D_i}{RT} \tag{2.19}$$

With the assumption that the solute species are sufficiently dilute so that the interactions amongst them can be neglected, material balances can be written on the basis of the above expression for the flux.

To obtain a useful general equation of charge transport for fuel cell modelling the electrochemical potential of charged species, ϕ_i, is introduced:

$$\nabla\phi_i = \nabla\Phi + \frac{RT}{F}\nabla lnc_i \tag{2.20}$$

By electroneutrality, $\sum_i z_i c_i = 0$, and combining Equations (2.16),(2.18),(2.19) and (2.20) gives the general governing charge transport equation as

$$\frac{\partial}{\partial t}\rho_{C,i} - \nabla\cdot(\sigma_i\nabla\phi_i) = \mathscr{E}_i \tag{2.21}$$

where $\mathscr{E}$ is a source/sink associated with the electrochemical reactions and external current sources $[A\cdot m^{-3}]$.

2.2.3 Mass transport of gases

The continuity equation

The conservation of mass equation is expressed from an REV as shown in Equation

(2.22). The source term accounts for changes in the mass flux due to the consumption or generation of reactants from each reaction.

$$\frac{\partial}{\partial t}\rho + \nabla \cdot (\rho \mathbf{u}) = \mathscr{M} \tag{2.22}$$

where $\mathscr{M}$ $[kgm^{-3}s^{-1}]$ is mass sources or sinks describing a rate of mass of fluids generated or consumed in the REV. ρ is the mixture density and $\mathbf{u}$ is the which can be calculated from the conservation of momentum. The momentum equation in porous PEM materials is given by Darcy's equations, for incompressible flow this is expressed as

$$\mathbf{u} = -\frac{\mathbf{K}}{\mu}(\nabla P - \rho \mathbf{g}) \tag{2.23}$$

Here μ denotes the dynamic viscosity of the fluid and $\mathbf{K}$ and $\mathbf{g}$ are the specific or intrinsic permeability of the porous medium $[m^2]$and gravitational force $[kg \cdot m^{-1}s^{-1}]$, respectively. Note that $\mathbf{K}$ is in general a second-order tensor. For an isotropic medium the specific permeability can be treated as a scalar. To keep the equation in a general form, the mixture density is defined as

$$\rho = \frac{P}{RT \sum(\varpi_i / M_i)} \tag{2.24}$$

where P, ϖ and M are the total gas pressure [Pa], mass fraction and molecular mass $[kgmole^{-1}]$of species i, respectively.

Equation (2.22) is the equation of continuity, which describes the time rate of change of the mixture density at a fixed point in space. For use in fuel cell modelling, it is convenient to write the equations in terms of fluxes of species. Application of the law of mass conservation to each species yields the equation of continuity for species i in a multicomponent mixture. Hence, the equation of continuity can be rewritten as

$$\frac{\partial}{\partial t}\rho_i + \nabla \cdot N_i = \mathscr{M}_i \tag{2.25}$$

Here N_i denotes the flux of gaseous species i $[kg \cdot m^{-2} \cdot s^{-1}]$. $\mathscr{M}_i$ is the rate at which volumetric mass of species i will be produced or consumed.

In section 2.2.1, the fluxes of species, N_i, is derived from the law of transport in dilute solutions which accounts for all fluxes due to migration, diffusion in a concentration gradient and convection with the bulk fluid velocity. Mass transport flux in a gas phase is analogous to that in the solution except that there is no migration term as gas molecules are uncharged, hence, flux of each gaseous species is given by

$$\mathbf{N}_i = -D_i \nabla c_i + c_i \mathbf{v} \tag{2.26}$$

Similarly, the first term describes the diffusive flux of the gaseous spices i due to the concentration gradient. The D_i, diffusion coefficient$[ms^{-1}]$, is a transport property of the gas, and is discussed in the next subsection. The final term corresponds to the convective flux of the species i in the movement of bulk mixture with velocity

$\mathbf{v}[ms^{-1}]$. Inserting Equation (2.26) into (2.25) and accounting for the available gas volume in the porous medium, $\epsilon_{g,k}$, yields the governing equation of gas transport:

$$\epsilon_{g,k}\frac{\partial}{\partial t}\rho_i + \nabla \cdot (-D_{i,k}\nabla c_i + c_i\mathbf{v}) = \mathscr{M}_{i,k} \tag{2.27}$$

where $\epsilon_{g,k}$ is the gas volume fraction in the REV in which the composition of gas and liquid phase is described by volume fraction of each phase.

In analogy with the continuity relation, the momentum equation of a mixture containing i species is given by

$$\frac{\partial}{\partial t}(\rho_i\mathbf{u}_i) + \nabla \cdot L_i = \mathscr{L}_i \tag{2.28}$$

where $\nabla \cdot L_i$ is the change of momentum flux of the mixture and $\mathscr{L}_i$ is the volumetric momentum sources or sinks such as a gravitational mass or mass density.

Gas diffusivity

As mentioned previously, the gas systems in fuel cell are multicomponent systems, i.e., mixture of hydrogen gas and water vapour in anode gas channel and mixture of oxygen and water vapour or humid air in cathode gas channel. Therefore, a gas mixture of N species is considered in gas transport. In multicomponent system, if the pore size is much larger than the mean free path there is momentum transfer between the molecules of different gases which gives rise to an random non-viscous mass transport mechanism referred to as gaseous diffusion. The binary diffusion

coefficient, with respect to the volume average flow, can be determined using the Chapman-Enskog theory together with an ideal gas law. According to this theory the binary diffusion coefficients show a small variation with composition, which for our purposes can be neglected. For dilute non-isothermal system the binary diffusion coefficient,$\mathscr{D}_{A,B}$, can be estimated from [99]

$$\mathscr{D}_{AB} = 1.8583 \times 10^{-7} \frac{\sqrt{T^3 \left(\frac{1}{M_A} + \frac{1}{M_B}\right)}}{p\sigma_{AB}^2 \Omega_{\mathscr{D},AB}} \tag{2.29}$$

in which M_i, T and p are the gas molar mass $[kg{\cdot}mol^{-1}]$, temperature [K] and pressure [atm], respectively. $\sigma_{A,B}$ denotes the Lennard-Jones parameter [unit:$\mathring{A}$] which can be estimated by averaging those of all species presented in the system and $\Omega_{\mathscr{D},AB}$, Equation (2.2.3), is a dimensionless function of the temperature and of the intermolecular potential field for one molecule of gas A and one of gas B. The supporting data for the calculation are provided in Table 2.2.3. The value of $\mathscr{D}_{AB}$ is in $[m^2 \cdot s^{-1}]$.

$$\Omega_{\mathscr{D},AB} = \frac{a_1}{\tau^{a_2}} + \frac{b_1}{e^{(b_2\tau)}} + \frac{c_1}{e^{(c_2\tau)}} + \frac{d_1}{e^{(d_2\tau)}} \tag{2.30}$$

where coefficients a, b, c and d are given in Table 2.2.3.

In gas diffusion layers, all gases are treated as an ideal gas and it is assumed that the transport of gas phases is separated from that of liquid phase. However, both liquid and gas phases are solved simultaneously. As hydrogen transports through

the porous media along with water vapour in the anode side and, similarly, oxygen transports in the mixture of nitrogen and water vapour in the cathode side, we assume that the dilute gas assumption is valid and may be treated by Fick's law. Thus, mass transport of all species in gas phase can be described by general governing equation.

Table 2.1: Data used in gas diffusivity calculation [100]

Species i	M_i,$[\frac{kg}{mol}]$	σ_i,$[\mathring{A}]$	ϵ_i
H_2	2.016	2.827	59.7
O_2	32.0	3.467	106.7
H_20	18.032	2.641	809.1
N_2	28.01	3.798	71.4
Air	28.97	3.711	78.6

Table 2.2: Data used in $\Omega_{\mathscr{D},AB}$ calculation [100]

Coefficient	a	b	c	d
1	1.06036	0.193	1.03587	1.76474
2	0.15606	0.47635	1.52996	3.89411

2.2.4 Heat transport

In this thesis, a non-isothermal system is considered to take into account for the temperature dependence of key parameters and pressures. Non-isothermal effects have been shown to be importance in a number of steady state studies and are expected to play and important role in determining the transients and dynamic behaviours of fuel

cell. Energy transport in a fuel cell is generated by the first law of thermodynamics. In analogy with the continuity and momentum equations in the previous section, the conservation of energy equation reads [99]

$$\frac{\partial}{\partial t}\left(\rho U+\frac{1}{2}\rho v^2\right)+\nabla\cdot\left(\rho U+\frac{1}{2}\rho v^2\right)\mathbf{v}+\nabla\cdot\mathbf{q}+\nabla\cdot(p\mathbf{v})+\nabla\cdot[\tau\cdot\mathbf{v}]-\rho\,(\mathbf{v}\cdot\mathbf{g})=Q_M \tag{2.31}$$

where U is the internal energy per unit mass which is dependent on the local temperature and density of fluid in the REV. It is noted that the internal energy includes heat added into the REV and work done in accordance with the first law of thermodynamics. $\mathbf{v}$ represents the fluid velocity. In Equation (2.31), the first term is the rate of accumulation of internal and kinetic energy per unit volume. The second term sums the convective heat fluxes that transports through the REV along with the fluid motion and the rate of energy input per unit volume by conduction. The last three terms include the work done on the fluid by pressure, shear and gravity forces. Q_M accounts for energy productions.

The above energy equation can be further simplified by considering only thermal energy instead, yielding

$$\rho\frac{DU}{Dt}=-(\nabla\cdot\mathbf{q})-p(\nabla\cdot\mathbf{v})-(\tau\nabla\mathbf{v})+Q_M \tag{2.32}$$

In the above equation, the substantial derivative of the internal and kinetic energy is as for the convenience. The conductive heat in the first term on the right hand and the

energy production are still the same. $p(\nabla \cdot \mathbf{v})$ describes the reversible rate of internal energy increase per unit volume by compression. $(\tau \nabla \mathbf{v})$ is the irreversible viscous dissipation. Rewriting the heat conduction term $\mathbf{q} = -k\nabla T$ with the assumption of incompressible fluid and that viscous dissipation is negligible Equation (2.32) can be reduced to

$$\frac{\partial \rho U}{\partial t} + \nabla \cdot \left(-k\nabla \mathbf{T} + \sum_i \rho U_i \right) = Q_M \tag{2.33}$$

This is the general equation of energy conservation used for modelling in the next chapter.

2.2.5 Multiphase flow

It is experimentally evident that liquid water is produced in the cathode catalyst layer under some operating conditions [34, 101]. The liquid water is then adsorbed by the ionomer and transported into the membrane to the anode due to water concentration gradient. This so-called "back diffusion" mechanism allows water production to diffuse from the cathode catalyst layer to the anode side. Additionally, liquid water is also transported by means of capillary forces through GDLs to the gas channel. Hence, the water in GDL can be considered in two phases: vapour from the humid oxygen/air and evaporated water, and liquid from the reaction as well as condensation. To treat the transport of water properly, a multiphase flow approach will be used in this study.

Recall that in the section 2.1.2, the volume fractions of liquid phase, ϵ_l is defined as a volume of liquid that occupies the pore space. By defining a liquid saturation, s, as a volume fraction of liquid phase and void space in each domain, ϵ_l can be rewritten as

$$\epsilon_l = s\epsilon \tag{2.34}$$

hence, $(1 - s)\epsilon$ is the gas volume fraction, ϵ_g, in pore space in porous medium. The aboved equation has to be satisfied $\epsilon_l + \epsilon_g = \epsilon$ in Equation(2.1), in other words, $s_l + s_g = 1$. To be consistent throughout this thesis, β is assigned as a suffix denoting the phase of a species, with $\beta = l$ for liquid phase and g for gas phase.

In general, partially saturated water vapour and liquid water can exist in the same pores, phase change can take place, and capillary-driven flow and accumulation or depleting of liquid water can take place, with all processes occurring dynamically. In the model, all fluid phase occupying the voids, e.g., reactants and water vapour, are assumed to be immiscible fluid, and the fluid phases are connected, and obey continuous flow. For two-phase immiscible flow, a viscous Newtonian wetting liquid together with a non-viscous gas are considered.

The derivation of the governing equations for two-phase flow is based on the following assumptions:

- The porous medium is homogeneous and isotropic inside the REV
- The solid phase is fixed in space and time

- The individual fluid phases remain continuous at all times
- The fluids exert no interfacial drag on each other
- The liquid are incompressible and the density is constant
- Gravity forces are small and negligible compared to capillary forces at the pore scale.

By employing the continuity equation of fluid flow through individual pores in the REV and the definition of volume fraction of phase defined above, the general flow equation for each phase can be obtained by integrating the continuity equation of all phases over the REV and is given by and is given by

$$\frac{\partial}{\partial t}(s\epsilon\rho)_\beta + \nabla \cdot (\rho \mathbf{v})_\beta = S_\beta \tag{2.35}$$

where $s\epsilon$ represents the volume fraction of the phase which occupies the pore space. The term S_β is accounted for mass transfer due to phase change.

As the amount of mass transfer due to a change of phase from liquid to gas or from gas to liquid has the same quantity but opposite direction, the sum of the production terms of all phases is zero. Thus the general equation for liquid-gas phase flow reads

$$\sum_\beta \left(\frac{\partial}{\partial t}(s\epsilon\rho)_\beta + \nabla \cdot (\rho \mathbf{v})_\beta \right) = 0 \tag{2.36}$$

Here the velocity of phase β can be estimated by using Equation(2.23) in which the index l and g will be assigned for liquid and gas phase.

Since the characteristic pore scale is in the range of several microns, surface forces, e.g., surface tensions between phase, dominate the flow distribution. Thus, neglecting the gravitational force and rewriting Equation(2.23) for the phase velocity of species yields

$$\mathbf{u}_\beta = -\frac{K_\beta}{\mu_\beta}\nabla P_\beta \tag{2.37}$$

Note K_β, the phase permeability, differs from the single phase permeability, K. In the case of two phase flow, the two phases occupying a pore influence the flow behaviour of one another as each occupies parts of the pore space which is not available for the other phase. Thus when the saturation of the wetting phase is for example reduced from full to partial saturation, the effective permeability for the wetting phase is in general decreased as well. The effective permeability for a phase k_β is defined as the product of the intrinsic permeability, K, and the relative permeability of phase $k_{r,\beta}$, i.e.

$$k_\beta = k_{r,\beta}K_k \tag{2.38}$$

where the subscript k denotes the domain k^{th} which may have different value of K.

2.2.6 Water transport

As noted earlier, the ionic conductivity of the membrane, which is critical to the overall performance of a PEM fuel cell, depends on the hydration level. Therefore, to be able to modelling fuel cell accurately it is of important to understand the physics of water transport, how it influences fuel cell performance, and the modelling framework to account for it.

Transport of water occurs throughout the fuel cell in three different phases: vapour, liquid and dissolved forms. Those states of water do not exist in all domains. For example, water vapour always exist in the GDLs but not in membrane, dissolved water state occurs only in the membrane and catalyst layers where ionomer is present. To make it relevant to the domains in which each phase of water is transported the discussions will start with the transport of water vapour and liquid form in pore spaces in catalyst layers and gas diffusion layers, and then moves on to that of dissolved water in catalyst layers and in the membrane, respectively.

In this study, it is assumed that liquid water in the cathode catalyst layer is generated on the surface of platinum inside the agglomerates in which platinum, carbon particles and ionomer are mixed together. This liquid then dissolves in the ionomer phase. Simultaneously, a portion of the dissolved water diffuses in the ionomer phase towards the membrane, while another portion moves to the surface of agglomerate. Once it has reached the pores it undergoes phase change to either liquid or vapour depending upon thermodynamics condition in the pores and travels through the pore

space toward the cathode GDL and gas channel.

In the GDLs the water can be either only vapour or a mixture containing both vapour and liquid depending on a variety of parameters including stoichiometry, inlet relative humidity, temperature and pressure. The transport of water vapour inside the GDLs was described earlier in the context of equation (2.37).

Transport of water in the membrane is generally described in terms of two main mechanisms: migration, in terms of electro-osmotic drag, and diffusion due to the concentration gradient of water between the anode and the cathode electrodes. The diffusion coefficient of the dissolved water depends strongly on the membrane water content, λ_w, which is a function of water activity, a_w and temperature. This diffusion coefficient has so far seen determined primarily through measurements and several empirical correlations have been proposed [22, 25, 84].

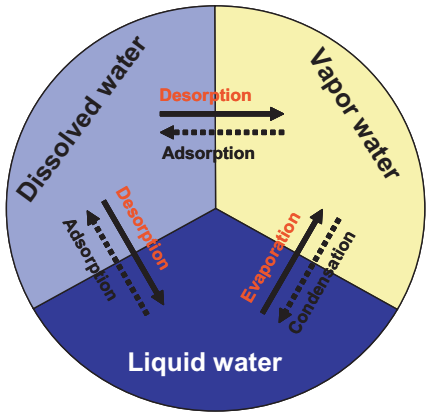

Figure 2.3: Conceptual forms of water

Electro-osmotic mechanism

In a membrane subjected to an electric potential, the migration of protons is accompanied by transport of water molecule. This so-called electro-osmotic drag mechanism may cause a dehydration on the anode side if appropriate water management is not in place. The electro-osmotic drag coefficient, n_d is defined as the number of water molecules dragged per proton and its value depends upon the water content of the electrolyte(ionomer). Fluxes of dragged water molecules are represented by

$$\mathbf{N}_{EOD} = -z_i u_i F c_i \nabla \Phi_i = n_d \frac{\mathbf{i}}{F} \tag{2.39}$$

where $\mathbf{i}$ is the total current density.

Several experimental results have been reported in the literature for the electro-osmotic drag coefficients in proton exchange membranes (PEM) under various conditions, and in particular dominating the effect of humidification [27, 32, 102].

Water Diffusion

Diffusion of dissolved water is driven by the concentration gradient, and assuming a quasi-Fickian process, the diffusion flux is given by

$$\mathbf{N_D} = \nabla \cdot (-D_{w,k} \nabla c_d) \tag{2.40}$$

where c_d and $D_{w,k}$ denote the concentration and the diffusion coefficient of dissolved water. Insertion of Equation (2.40) and (2.39) into the general governing equation(2.27) yields

$$\epsilon_{e,k}\frac{\partial}{\partial t}\rho_w + \epsilon_{e,k}\nabla\cdot(\mathbf{N_D} + \mathbf{N}_{EOD}) = \mathscr{W}_{e,k} \tag{2.41}$$

in which $\mathscr{W}_{e,k}$ is the volumetric water generation or consumption in the domain k. Equation 2.41 is the flux-form of the governing equation for water transport in the domains containing the membrane phase, i.e. catalyst layers and the electrolyte membrane. Equation 2.41 is a generalization to transient of the Springer's original diffusion model (Springer, Zawodzinski and Gottesfeld, (1991)). Springer's model, which is solved in conjunction with Ohm's law, is the most popular membrane transport in the literature due to its robustness and reasonable fit with experimental data for Nafion membranes. The model does have some drawbacks as it relies on empirical correlations obtained for Nafion membranes under specific conditions; it also performs less satisfactorily under low humidification conditions (Fimrite et al, 2005a). Alternative models have been proposed in the literature, and they can be generally classified as "hydraulic"(i.e. driven by pressure gradient) and "diffusion"models (driven by concentration gradient). Fimrite et al [96] provide a review of the advantages and drawbacks of these models and note that transport models based on the use of the chemical potential gradients in the membrane provide a conceptually simpler and more general modelling framework. Such models have been proposed by

Janssen [102], Thampan et al [103], Weber and Newman [104] and Fimrite et al [105]. These models have not yet been systematically tested and Springer's framework was selected for an extension to the transient formulation in this thesis. The model is implemented, however, using temperature dependent sorption isotherms to address one of the shortcomings of earlier implementations [96]. Details on the implementation are provided in Chapter 3.

Chapter 3

Modelling Framework

In this chapter the implementation of the mathematical model established in the previous chapter along with a description of the computational method are presented. Furthermore, the model developed in this thesis is implemented in two scales of dimensionality: a two-dimensional steady-state model (2D) and a one-dimensional time-dependent model (1D-t). The rationale for this approach is the limited body of experimental literature covering dynamic behaviour in operating fuel cells, which can be used for model validation. In order for a model to represent the physics and compare well with experimental observations, the key processes must be adequately acconted for. For instance, 2D water transport should be integrated in the model to study cross-sectional water transport. The 2D steady-state model implementation is validated through comparison with available experimental data as well as a 2D fuel cell model developed by Secanell et al. [106] with an in-house code. With this

validated model, a 1D time-dependent model for an MEA is implemented and applied to study dynamic and transient phenomena in fuel cells.

3.1 Fuel Cell Model

Model description

In this work, a nonisothermal two-phase dynamic model of an MEA including the gas diffusion layers, catalyst layers and membrane is developed. Since the focus of this study is to gain insight into the dynamic phenomena in an MEA, the gas flow channels are not considered but rather imposed as boundary conditions. A schematic of a 2D domain representing a through-plane normal to a membrane is provided in Figure 3.1(a). A red-dashed box shows the 2D computational domain and a blue dashed line shows the 1D-t computational domain. Figure 3.1(b) depicts the domains and boundaries for the 2D model. The symbols and indices labelling the computational domains are kept the same for both 1D and 2D geometries. However, as the 1D model boundaries are usually imposed by input parameters such as reactant mole fraction, temperature and solid electrical potential, the labels of nodes and boundaries in the 1D computational geometry are assigned differently and shown in Figure 3.1(c).

Detailed model descriptions of the following transport phenomena in each computational domain are provided.

- A macro-homogeneous based electrochemical kinetics model in the anode cata-

lyst layer (domain Ω_2).

- The diffusive-convective transport of hydrogen and water vapour through the anode gas diffusion layer and catalyst layer (domains Ω_1 and Ω_2).
- The conduction of electrons through the gas diffusion layers and catalyst layers (domains Ω_1 and Ω_2).
- The transport of protons through the polymer phase of the catalyst layers and membrane (domains Ω_2, Ω_3 and Ω_4).
- The diffusive-convective transport of oxygen, water vapour and nitrogen gas through the cathode gas diffusion layer and catalyst layer (domains Ω_4 and Ω_5).
- The electrochemical kinetics based on the spherical shape agglomerate model [107] in the cathode catalyst layer (domain Ω_4).
- The transport of water through the membrane driven by dissolved water concentration gradients and electro-osmotic drag (domains Ω_2, Ω_3 and Ω_4).
- The transport of liquid water through the anodic and cathodic gas diffusion layers and catalyst layers of anode and cathode (domains Ω_1, Ω_2, Ω_4 and Ω_5).

Model assumptions

The following general assumptions are used in both the 2D steady-state and 1D time-dependent models.

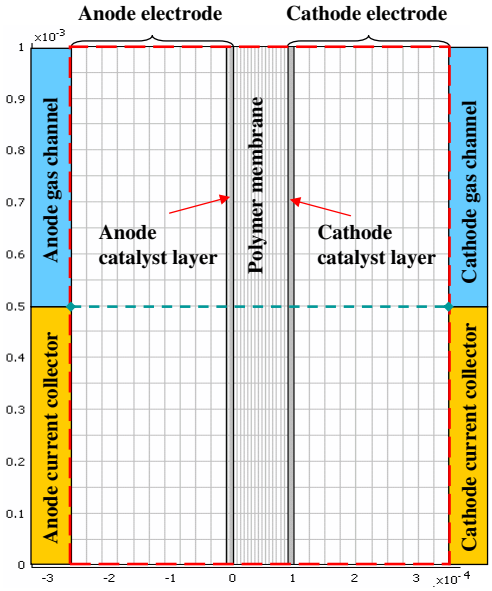

(a) Computational domain for MEA

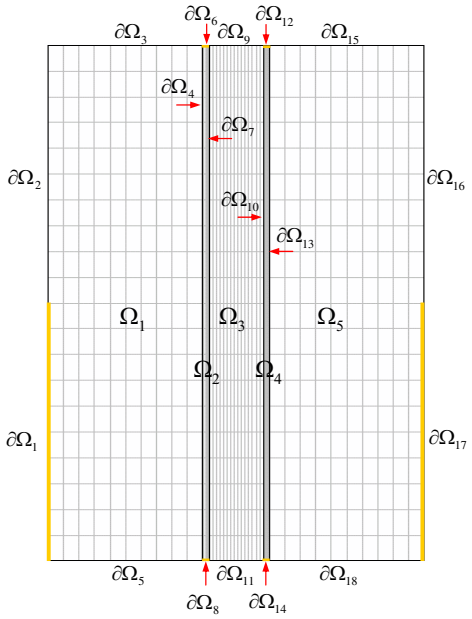

(b) Labels of domains and boundaries for 2D geometry

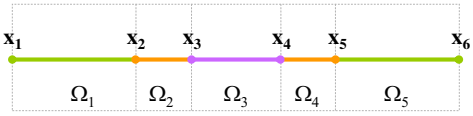

(c) Labels of domains and boundaries for 1D geometry

Figure 3.1: Schematics of the (a)MEA computational domain and grid discretization used in 2D computational simulations (b) labeled 2D domains (Ω_i) and boundaries ($\partial\Omega_i$) and (c) the boundaries for 1D formulation

- All gaseous species behave as ideal gases.
- The gas pressure in the gas diffusion layers is assumed to be constant.
- The diffusive fluxes of gases are described using a Fickian diffusion approach.
- The product water of the cathode reaction is assumed to be liquid phase and generated inside the agglomerates.
- Gravitational effects on the transport of liquid water are neglected.
- Interfacial electrical contact losses are neglected.
- The active area is small therefore gas can be assumed equally distributed.

3.1.1 Modelling anode catalyst and diffusion layer

In this section, the mathematical models of the reaction kinetics, hydrogen and water vapour transport, and charge transport in the GDL and CTL on the anode side are described.

Anode reaction kinetics model

The catalyst layer is a thin layer coated on both sides of the membrane, consisting of the layer consists of a mixture of platinum, carbon and electrolyte. The thickness of the catalyst layer is typically in the 10-50 μm range. From a macroscopic point of view, the reaction sites exist in the so-called agglomerates, where platinum and carbon

particles are mixed together with electrolyte. These agglomerates also contain water-filled channels into which the reactant gas is dissolved and subsequently diffuses to the reaction sites. In the anode catalyst layer, the hydrogen reduction reaction takes place at the surface of the dispersed platinum catalyst. Electrons are conducted via carbon particles; whereas protons travel through the electrolyte. A schematic diagram of the catalyst layer is shown in Figure (3.2)(b). Using equation (2.13) in accordance

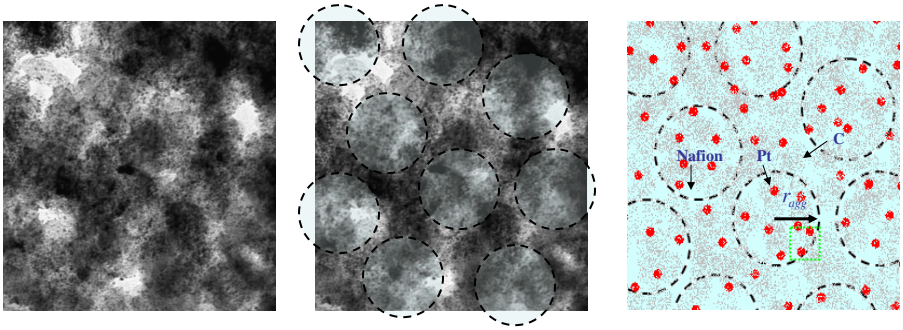

(a) TEM image of catalyst layer(Courtesy of [108])

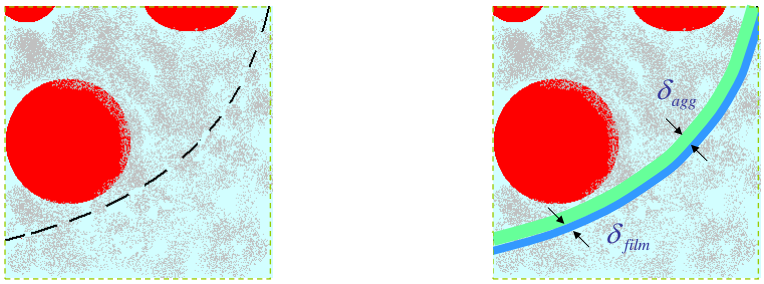

(b) Conceptual model of catalyst layer

Figure 3.2: (a) A close-up of catalyst layer obtained from TEM image and a conceptual schematic of agglomerate in catalyst layer, the red dots represent the dispersed Pt and gray clumps are carbon particles, and (b) the sub-figure on the left hand shows inside an agglomerate a Pt element on which reaction takes place and the right-hand one indicates an example of electrolyte and water film covering the agglomerate pellet.

with the effect of concentration, the expression for the volumetric current density due

to the hydrogen reduction reaction at the anode catalyst can be written as

$$\nabla \cdot \mathbf{i}_a = A_v i_0^{ref} \left(\frac{c_{H_{2,s}}}{c_{H_2^{ref}}} \right)^{\gamma} \left\{ exp\left(\frac{\alpha_a F}{RT}(\phi_s - \phi_m) \right) - exp\left(\frac{-\alpha_c F}{RT}(\phi_s - \phi_m) \right) \right\} \quad (3.1)$$

where A_v is the specific reaction interfacial area per volume of catalyst. i_0^{ref} is the reference exchange current density. $c_{H_{2,s}}$ is the hydrogen concentration at the reaction site, which is the concentration of dissolved gas in a Nafion phase covering the agglomerate pellet, and is obtained from

$$c_{H_{2,s}} = \frac{c_{H_{2,g}}}{k^H_{H_{2,N}}} \quad (3.2)$$

The parameter $k^H_{H_{2,N}}$ is the dimensionless Henry's law constant which is dependent upon the temperature over the solution surface as

$$k^H_{H_{2,N}} = \frac{H_{H_{2,N}}}{RT} \quad (3.3)$$

where $H_{H_{2,N}}$ is the Henry's law constant in Nafion defined as the ratio between the aqueous-phase concentration of hydrogen and its gas-phase concentration.

This divergence of the current density is related to the average current density at the surface of the catalyst particles in an agglomerate pellet. The specific active area of the catalyst layer relates to the physical parameters used in making the catalyst layer such as the platinum loading, m_{Pt}, and a catalyst surface area per unit mass of

the catalyst particles, A_{Pt}. The relationship is in the form:

$$A_v = \frac{A_{Pt} m_{Pt}}{L} \tag{3.4}$$

where L denotes the catalyst layer thickness. A_{Pt} is the active surface area of platinum in the catalyst layer, which is a function of a ratio of platinum and carbon particles and can be determined via the empirical formula studied by [109] as

$$\begin{aligned} A_{Pt} = 2.2779 \times 10^5 (Pt \mid C)^3 - 1.5857 \times 10^5 (Pt \mid C)^2 \\ -2.0153 \times 10^5 (Pt \mid C) + 1.5950 \times 10^5 \end{aligned} \tag{3.5}$$

in which $Pt \mid C$ represents the ratio of platinum catalyst and carbon in powder mixture. As stated in the model description above, the reaction site is in an agglomerated pellet into which hydrogen gas dissolves and diffuses through the water and electrolyte films to reach the Pt particles. Figure(3.2(b)) shows the schematic of one agglomerate pellet with electrolyte and water films.

Modelling gas transport in the anode

The anode consists of the gas diffusion layer and catalyst layer. The gaseous species present at the anode are H_2 and H_2O. Both gases are fed into a gas channel and transport through the gas diffusion layer through diffusion and convection. Based on the dilute gas theory [99], a diffusive flux can be derived using Fick's law. Employing

equation (2.27) and relating the concentration of species, c_i, to the mixture concentration, c_{tot}, via its mole fraction, x_i, the mass balance on the anode side is given by

$$\epsilon_V^k \frac{\partial}{\partial t}[(1-s)c_i] + \nabla \cdot \left(-c_{tot} D_i^{eff,k} \nabla x_i + c_i \mathbf{v}\right) = S_i \tag{3.6}$$

where x denotes the mole fraction of species. i represents H_2 and vapour, V is pore space and k denotes GDL, CTL. The mass balance equation for the anode porous electrode contains an additional term that accounts for the convective flux of each species within the pores due to the bulk velocity, $\mathbf{v}$.

The physical properties of the GDL, such as porosity and tortuosity, can have a significant impact on the transport of reactants as well as on overall cell performance. The effective values of flow characteristics such as diffusivity and tortuosity are thus used in the model. In addition, the liquid saturation, s, defined in section 2.2.5 is employed in all gas transport equations to describe the effect of an increase of liquid water in the domain. To account for porous medium morphology Bruggeman's relationship [110] is employed to determine the effective parameters from the bulk values. Therefore, all diffusion coefficients are corrected by a factor of $\epsilon_k^{3/2}$. Here, ϵ_k is a gas volume fraction in the domain k^{th}. The effective gas diffusion coefficients in domain k^{th} can be calculated by the formula below.

$$D_i^{eff,k} = D_{i,k} \left((1-s)\varepsilon_V^k\right)^{3/2} \tag{3.7}$$

in which D_i is the diffusivity of species i in free space is obtained from the Chapman-Enskog kinetic theory [100] which accounts for a dependence of temperature and pressure for dilute systems such as vapour in H_2 gas and O_2 in N_2 gas or air.

Mercury intrusion porosimetry is typically employed to measure the porosity of the GDL. The relationship of porosity of medium and a volume fraction of solid matrix in the gas diffusion medium, ϵ_S^{GDL} is

$$\epsilon_V^{GDL} = 1 - \epsilon_S^{GDL} \tag{3.8}$$

The term on the right hand side in equation(3.6), S_i represents a rate of reaction per unit volume of species i. In other words, a volumetric concentration production or depletion rate depending on species and reaction is considered. This reaction production is conserved and can be determined from the chemical reactions of each species over the domain. For the HOR at the anode catalyst, recalling equation(1.1)

$$H_2 \rightarrow 2H^+ + 2e^-$$

and applying chemical balance of the above reaction into equation(2.9) yields

$$S_{H_2} = -\frac{\nabla \cdot \mathbf{i}_a}{2F} \tag{3.9}$$

where $\nabla \cdot \mathbf{i}_a$ is the total current and the negative sign indicates that hydrogen is

consumed at the anode.

The insertion of equation(3.7) and (3.9) into equation (3.6) results in

$$\varepsilon_V^{CTL}\frac{\partial}{\partial t}[(1-s)c_{H_2}] - \nabla\cdot\left(c_{tot}D_{H_2}^{eff,\Omega}\nabla x_i + c_{H_2}\mathbf{v}\right) = \begin{cases} 0 & \text{in } \Omega_1 \\ -\frac{\nabla\cdot\mathbf{i}_a}{2F} & \text{in } \Omega_2 \end{cases} \tag{3.10}$$

where the volume fraction of pore space in CTL, ε_V^{Ω} is given in equation(3.8) and (3.33).

There are no reactions occurring in the GDL, thus the source term on the right side equals zero for Ω_1. The transport equations for water vapour includes all source terms that account for the phase change process and mass transfer between vapour and dissolved gas. Similar to the general transport equation, the governing equations for water vapour in the GDL and CTL are

$$\varepsilon_V^{GDL}\frac{\partial}{\partial t}[(1-s)c_{H_2O}] - \nabla\cdot\left(c_{tot}D_{H_2O}^{eff,GDL}\nabla x_{H_2O} + c_{H_2O}\mathbf{v}\right) = \begin{cases} S_{cond/evap} & \text{in } \Omega_1 \\ S_{cond/evap} + S_{vsorp} & \text{in } \Omega_2 \end{cases} \tag{3.11}$$

where $S_{cond/evap}$ and S_{vsorp} are the source terms due to the condensation/evaporation process and vapour sorption process, which are defined as in Equation (3.51) and (3.29) in section 3.1.2, respectively.

Anode charge transport submodel

At the anode, the electrons released from the hydrogen oxidation reaction conduct via carbon particles in the catalyst layer and gas diffusion layer. As given in section 2.2.2, the electron transport is governed by Ohm's law

$$\frac{\partial}{\partial t}\rho_{e,C} - \nabla \cdot (\sigma_s \nabla \phi_s) = \mathscr{E}_k \tag{3.12}$$

where $\rho_{i,C}$ is the charge density of an electron. σ_s is the conductivity of the solid matrix, i.e. GDL and CTL. $\mathscr{E}_i$ is the volumetric flux of electrons released from the reaction and is related to the ORR kinetics, $\mathbf{i}_a$, (Equation 3.1) by

$$\mathscr{E}_k = \begin{cases} 0 & k = \Omega_1 \\ -\nabla \mathbf{i}_a & k = \Omega_2 \end{cases} \tag{3.13}$$

While the HOR is taking place in the catalyst layer, protons are simultaneously released from the reaction and move toward the cathode via the electrolyte. Hence, protons exist only in the cathode catalyst layer and membrane. Proton transport is governed by

$$\frac{\partial}{\partial t}\rho_{p,C} - \nabla \cdot (\sigma_m \nabla \phi_m) = \mathscr{E}_k \tag{3.14}$$

where $\rho_{p,C}$ is the charge density of a proton. σ_m is the conductivity of the electrolyte. $\mathscr{E}_k$ is the volumetric flux of protons released from the reaction, and is given by

$$\mathscr{E}_k = \begin{cases} 0 & k = \Omega_1 \\ \nabla \mathbf{i}_a & k = \Omega_2 \end{cases} \tag{3.15}$$

3.1.2 Modelling transport processes in the membrane

The transport of water is described by two mechanisms: electro-osmotic drag and diffusion due to concentration gradients. Using Ohm's law in equation (2.16) and substituting the total current in equation (2.39) yields the flux of water according to electro-osmotic drag as

$$N_{EOD} = -n_d \frac{\epsilon_{e,k}\sigma_e}{F} \nabla \phi_e \tag{3.16}$$

$$n_d = \frac{5}{44}\lambda_w \tag{3.17}$$

where n_d is the electro-osmotic drag coefficient determined using Equation (3.17) which proposed by [84]. The subscript k denotes the domain in which the drag is being calculated. Since protons travel in both the catalyst layer and the membrane which consist of different volume fractions of the electrolyte, the term, $\sigma_{e,k}$ is added to take into account the effect of those volume fraction. The membrane protonic conductivity, σ_e, is dependent upon the hydration level of the membrane and membrane

temperature, which for Nafion membranes can be determined using the relation

$$\sigma_e = \sigma_e^o exp[1268(\frac{1}{303} - \frac{1}{T_{cell}})] \tag{3.18}$$

where the σ_e^o is the membrane conductivity at a reference temperature 30^oC

$$\sigma_e^o = 0.5139\lambda_w - 0.326 \tag{3.19}$$

According to the previous studies on water transport in the polymer membrane [23, 25,27,84,110], the state of water in the electrolyte can be described as absorbed water or uptake water. The variable commonly used for water in the electrolyte phase in the membrane model is termed the membrane water content, λ_w, defined as

$$\lambda_w = \frac{moles\,of\,absorbed\,water}{moles\,of\,SO_3^-} \tag{3.20}$$

The dependency of the membrane water content on water activity, a_w can be expressed as

$$\lambda_w(a_w, T) = \begin{cases} 0.043 + 17.8a_w - 39.85a_w^2 + 36a_w^3 & \text{at } T_{cell} = 30°C \text{ [84]} \\ 0.3 + 10.8a_w - 16a_w^2 + 14.1a_w^3 & \text{at } T_{cell} = 80°C \text{ [111]} \end{cases} \tag{3.21}$$

where water vapour activity, a_w, is defined as

$$a_w = \frac{x_w P_g}{p^{sat}} \tag{3.22}$$

in which x_w is the mole fraction of water vapour equilibrated with membrane phase and P_g is the total gas pressure. The term p^{sat} represents the saturation pressure at the gas temperature. The above expressions for membrane water content are obtained from fitting the experimental data at two different temperatures by Springer et al. [84] for the temperature at 30°C and by Hinatsu et al. [111] for the temperature at 80°C. Both experiments were done using Nafion 117 membranes.

In this study, the characteristics of a fuel cell under nonisothermal conditions are of interest. Accordingly, the expression for the membrane water content needs to be modified by taking into account the effect of temperature variation on a membrane water sorption as proposed by Ge et al. [27]. The water content expression becomes

$$\lambda_w(a_w, T) = \lambda_w(a_w, 30) + (\lambda_w(a_w, 80) - \lambda_w(a_w, 30)) \left(\frac{T - 303}{50} \right) \tag{3.23}$$

The electro-osmotic drag coefficient, n_d, in Equation (3.16) determines how many molecules of water are dragged along with the protons moving from the anode to cathode. Base on experimental evidence this coefficient is simply related to the water content described above.

Given that the water in the electrolyte is in a dissolved form, the dissolved water,

C_w, relates to the membrane properties via a simple expression

$$C_w = \frac{\rho_m}{EW_m} \tag{3.24}$$

in which ρ_m and EW_m refer to the membrane density and equivalent weight in dry state, respectively.

To describe the transport of water in the membrane in terms of diffusion, the flux of dissolved water is expressed as

$$N_\lambda = -\epsilon_m^{eff} D_w \nabla (C_w) \tag{3.25}$$

where ϵ_m^{eff} denotes the volume fraction of electrolyte phase in the domain. D_λ is the effective diffusion coefficient of dissolved water.

To date many different values of water diffusion coefficients and time constants to reach steady states have been reported in the literature [24, 25, 29, 84, 110, 112]. However, the empirical water diffusion coefficient expression proposed by Springer et al. [84] is chosen for this work because it is more robust. The water diffusion coefficient takes the form

$$D_w = D_{w,30} 10^{-10} exp[2416(\frac{1}{303} - \frac{1}{T_{cell}})] \tag{3.26}$$

where $D_{(\lambda),30}$ is the empirical correlation for the water diffusion coefficient measured

at the reference temperature 30°C, which is given by

$$D(w,30) = 2.563 - 0.33\lambda_w + 0.0264\lambda_w^2 - 6.71 \times 10^{-4}\lambda_w^3 \tag{3.27}$$

$D(w,30)$ is in m^2/s

Inserting Equation (3.16) and (3.25) into Equation (2.41) leads to the governing transport equation for water in the membrane as

$$\epsilon_{m,k}^{eff}\frac{\partial C_w}{\partial t} + \nabla\left\{-\epsilon_{m,k}^{eff}D_w\nabla\left(C_w\right) - n_d\frac{\epsilon_{m,k}^{eff}\sigma_m}{F}\nabla\phi_p\right\} = \begin{cases} S_{vsorp} + S_{lsorp} & \text{in } \Omega_2\&\Omega_4 \\ 0 & \text{in } \Omega_3 \end{cases} \tag{3.28}$$

in which S_{vsorp} and S_{lsorp} are the volumetric water sorption when the membrane is equilibrated with vapour and liquid water in the catalyst layers. The detailed description of S_{vsorp} is provided below whereas that of S_{vsorp} is given in section 3.1.4.

The rate of mass interchange between the membrane phase and vapour phase across the pore space and electrolyte interface, S_{sorp}, can be obtained via the expression

$$S_{vsorp} = \begin{cases} k_{va}\frac{\rho_m}{EW_m}(\lambda - \lambda_v^*) & \text{for absorption} \\ k_{vd}\frac{\rho_m}{EW_m}(\lambda - \lambda_v^*) & \text{for desorption} \end{cases} \tag{3.29}$$

in which the parameters k_{va} and k_{va} are the sorption coefficients for vapour absorption and desorption process, respectively. The term denotes the equilibrium value of water

content corresponding to the vapour state of water.

The sorption process for the vapour-dissolved phase of water involves both an absorption and desorption processes. This is due to the concentration-driven force between the state of local water and the equilibrium state of phases. According to the previous studies [22, 25, 84, 111] the Nafion membrane has a different maximum water content when it is in equilibrium with vapour and liquid water. This is well known as Schroeder's paradox. Referring to [27, 29] the sorption rate constant is a function of temperature.

3.1.3 Modelling cathode catalyst and diffusion layers

Cathode kinetic reaction submodel

In this study, the materials used as well as the microstructure of electrodes in both the anode and cathode are assumed to be identical. Therefore, all material properties used in the expressions for both electrodes are the same. At the cathode, due to the relatively high activation overvoltage, the oxygen oxidation reaction on the cathode side is crucial and potentially limits the performance of the PEM fuel cell. The rate of the ORR is relatively slow compared to that of HOR at the anode. The details of the cathode kinetics based on the agglomerate model is given below. Oxygen gas diffuses through the pore channels in the cathode GDL and reaches the interface between the GDL and CTL.

To account for the influences of the CTL microstructure in which oxygen, water vapour, liquid water, protons and electrons are transported, the composition in terms of platinum and carbon used are required for the volume fraction calculation. The expression that relates the catalyst layer platinum loading to porosity be is given by

$$\epsilon_S^{CTL} = (\frac{1}{\rho_{Pt}} + \frac{1 - Pt \mid C}{Pt \mid C\rho_c})\frac{m_{Pt}}{L} \tag{3.30}$$

where $Pt \mid C$ is a ratio of platinum and carbon content in the catalyst layers and m_{Pt} is the platinum loading $[mgPt/cm^2]$. The volume fraction of Nafion electrolyte in the CTL can be obtained from

$$\epsilon_N^{CTL} = \frac{4}{3}\pi n[r_{agg}^3\epsilon_{agg} + ((r_{agg} + \delta_{agg})^3 - r_{agg}^3)] \tag{3.31}$$

where r_{agg}, δ_{agg} and ϵ_{agg} denote the radius of the agglomerate pellet, the thickness of the Nafion film covering the agglomerate, and the volume fraction of Nafion in the agglomerate. $\bar{n}$ is the average number of agglomerate pellets per volume of the CTL, which is determined by the expression

$$\bar{n} = \frac{\epsilon_S^{CTL}}{\frac{4}{3}r_{agg}^3(1 - \epsilon_{agg})} \tag{3.32}$$

The volume fraction of pore spaces can be obtained via the relation

$$\epsilon_V^{CTL} = 1 - \epsilon_N^{CTL} - \epsilon_S^{CTL} \tag{3.33}$$

Given that the cathode CTL is modelled using an agglomerate approach with spherical agglomerates, the kinetics expression for the total cathodic reaction rate per unit volume of electrode can be expressed as

$$\nabla \cdot i_c = A_v i_{ORR} E_r \tag{3.34}$$

where A_v is the specific interfacial area per unit volume of the catalyst layer and given in equation (3.4), and i_{ORR} is the transfer current for the ORR. E_r is the effectiveness factor due to mass transfer and reaction within each agglomerate and can be determined by

$$E_r = \frac{1}{\phi_L}(\frac{1}{tanh(3\phi_L)} - \frac{1}{3\phi_L}) \tag{3.35}$$

where ϕ_L is Thiele's modulus for a spherical agglomerate given by

$$\phi_L = \frac{r_{agg}}{3}\sqrt{\frac{k_c}{D^{eff}}} \tag{3.36}$$

in which r_{agg} is the radius of a spherical agglomerate which can be determined by

$$r_{agg} = 3\frac{V_{agg}}{S_{agg}} \tag{3.37}$$

Based on the agglomerate model [106, 107, 113] and the above supporting expression, the governing equation for the cathode current can be written as

$$\nabla \cdot i_c = 4F \frac{c_{O_2}}{H_{O_2}} \left(\frac{1}{E_r k_c (1 - \varepsilon_v^{CTL})} + \frac{(r_{agg} + \delta_{agg})\delta_{agg}}{a_{agg} r_{agg} D_{O_2,N}} \right)^{-1} \tag{3.38}$$

where k_c is the rate constant given by equation (3.40). a_{agg} is a ratio of the effective surface area usable to dissolve oxygen into the agglomerate to the catalyst layer volume, which can be determined by physical agglomerate parameters via the expression

$$a_{agg} = n 4\pi (r_{agg} + \delta_{agg})^2 \epsilon_v^{CTL} \tag{3.39}$$

$$k_c = \frac{A_v i_0^{ref}}{4F(1 - \varepsilon_v^{CTL}) c_{O_2}^{ref}} exp \left\{ -\frac{\alpha_c F}{RT} (\phi_s - \phi_m) \right\} \tag{3.40}$$

This equation will later be used for a source term in the charge transport equations at the cathode catalyst layer.

Modelling gas transport in the cathode electrode

At the cathode electrode, humidified air consisting of oxygen, water vapour and nitrogen moves through the diffusive medium. Oxygen is then dissolved into the Nafion phase at the catalyst layer and diffuses through the Nafion to reach the platinum surface. Here, oxygen reacts with protons and produces water in liquid form via the

oxidation reaction. The mass balance equations for the cathode can be written as

$$\varepsilon_V^k \frac{\partial}{\partial t}[(1-s)c_i] - \nabla \cdot \left(c_{tot} D_i^{eff} \nabla x_i\right) = S_i \tag{3.41}$$

where i denotes O_2, N_2, and vapour, V refers to pore space and k represents GDL, CTL The parameters used in the above equation for individual species is the diffusion coefficient, D_i^{eff}, which can be obtained from equation (2.29), (2.30) and (3.7). The term on the right side of equation 3.41 represents the volumetric flow rate of species i, which is given in Table 3.1.

The oxygen transport in the MEA is governed by

$$\varepsilon_V^{GDL} \frac{\partial}{\partial t}[(1-s)c_{O_2}] - \nabla \cdot \left(c_{tot} D_{O_2}^{eff,k} \nabla x_{O_2} + c_{O_2}\mathbf{v}\right) = \begin{cases} -\frac{\nabla \mathbf{i}}{4F} & \text{in } \Omega_4 \\ 0 & \text{in } \Omega_5 \end{cases} \tag{3.42}$$

where k refers to the domain Ω_4 and Ω_5. $D_{O_2}^{eff,k}$ is the effective diffusion coefficient of oxygen, which is defined as in Equation (3.7)in section3.1.1.

The governing equation for water vapour in the anode can be developed along similar lines and reads

$$\varepsilon_V^{GDL} \frac{\partial}{\partial t}[(1-s)c_{H_2O}] - \nabla \cdot \left(c_{tot} D_{H_2O}^{eff,k} \nabla x_{H_2O} + c_{H_2O}\mathbf{v}\right) = \begin{cases} s_{cond/evap} + s_{vsorp} & \text{in } \Omega_4 \\ s_{cond/evap} & \text{in } \Omega_5 \end{cases} \tag{3.43}$$

Table 3.1: Source terms used in gas transport equations

Source term,S_i	aCTL	cCTL
$\mathscr{M}_{H_2}$	$\frac{-\nabla\cdot i}{2F}$	0
$\mathscr{M}_{O_2}$	0	$\frac{-\nabla\cdot i}{4F}$
$\mathscr{M}_{H_20}$	0	$\frac{\nabla\cdot i}{2F}$
$\mathscr{M}_{N_2}$	0	0

in which $D_{H_2O}^{eff,k}$ is the vapour diffusion coefficient in pore space. $s_{cond/evap}$, s_{vsorp} are the source terms due to the condensation/evaporation process and vapour sorption process which are defined as in Equation (3.51) and (3.29) in section 3.1.2, respectively.

PEMFCs typically operate with air as the oxidant, where nitrogen gas dilutes the system. The governing equation for nitrogen in the cathode is governed by

$$\varepsilon_V^k \frac{\partial}{\partial t}[(1-s)c_{N_2}] - \nabla\cdot\left(c_{tot}D_{N_2}^{eff,k}\nabla x_{N_2} + c_{N_2}\mathbf{v}\right) = 0 \tag{3.44}$$

where k refers to the CTL and GDL.

Cathode charge transport submodel

By analogy with the governing equation for charge transport at the anode, the equation that governs the transport of charge at the cathode is given by

$$\frac{\partial}{\partial t}\rho_{e,C} - \nabla\cdot(\sigma_s\nabla\phi_s) = \mathscr{E}_k \tag{3.45}$$

where $\rho_{e,C}$ denotes electron density in the solid phase. σ_s is the conductivity of the solid matrix. The volumetric electron generation, $\mathscr{E}_k$, due to the reaction is obtained from

$$\mathscr{E}_k = \begin{cases} \nabla \mathbf{i}_a & k = \Omega_4 \\ 0 & k = \Omega_5 \end{cases} \tag{3.46}$$

The governing equation for ionic transport is given by

$$\frac{\partial}{\partial t}\rho_{p,C} - \nabla \cdot (\sigma_m \nabla \phi_m) = \mathscr{E}_k \tag{3.47}$$

where σ_m is the conductivity of the electrolyte and ϕ_m refers to the proton potential in the electrolyte. The volumetric source term, $\mathscr{E}_k$, is given by

$$\mathscr{E}_k = \begin{cases} -\nabla \mathbf{i}_a & k = \Omega_4 \\ 0 & k = \Omega_5 \end{cases} \tag{3.48}$$

3.1.4 Modelling liquid water transport in porous electrodes

It is well known that operating a fuel cell at a high current density may result in flooding, especially at the cathode. Water management has been a central issue in previous studies and various methodologies have been proposed to tackle this problem. The recent work of Zhang et al. [34] showed that water generated at the cathode catalyst layer is in a liquid form. Understanding water production and the level of

water saturation have been gaining great attention in the field as since they have a tendency to reduce both the local fuel and oxidant mass diffusivities. The assumption that water generated in liquid form at the cathode catalyst layer has been made in models by [80,114]. Accordingly, in our model, water is assumed to be liquid with the assumption stated. Transport of liquid water is governed by the continuity of mass of liquid water (discussed further in the context of equation 2.41).

$$\frac{\varepsilon_k \rho_l}{M_w}\frac{\partial s}{\partial t} - \nabla \cdot \left(\frac{\varepsilon_k \rho_l}{M_w}\mathbf{v}_l\right) = S_{product} + S_{cond/evap} + \Lambda_w S_{lsorp} \tag{3.49}$$

where ρ_l is the density of liquid water and M_w is the molecular weight of water. Λ_w is the specific water concentration in membrane phase. In the above equation, the terms on the left account for the accumulation of mass in the pore space in the porous electrode and the diffusive flux of the liquid water, respectively. $\mathbf{v}_l$ denotes the velocity of liquid in the pore channels. On the right side, $S_{product}$ is the product water from the electrochemical reaction, $S_{cond/evap}$ is the volumetric rate of mass transfer between liquid and vapour due to a mass change in the capillary evaporation or condensation process, and S_{lsorp} is the rate of mass transfer between the dissolved water in the membrane and liquid at the liquid-membrane interface.

The water produced from the ORR reaction is given by

$$S_{product} = \frac{\nabla \mathbf{i}}{2F} \tag{3.50}$$

where $\nabla \mathbf{i}$ refers to the total current in Equation (3.38).

In considering the phase change of water between the liquid and vapour phase in small pores, the temperature of all phases including the solid wall in the volume is assumed to be the same as the pore volume. Therefore, the assumption of phase equilibrium holds. The rate of phase change can be written

$$S_{cond/evap} = \begin{cases} k_{cond} \frac{\varepsilon_V^k x_w}{R_g T}(p_v - P_{sat}) & \text{for condensation} \\ k_{evap} \frac{\varepsilon_V^k \rho_l s}{M_w}(p_v - P_{sat}) & \text{for evaporation} \end{cases} \tag{3.51}$$

in which k_{cond} and k_{evap} are the mass transfer rate at the interface between phases. p_v is the water vapour partial pressure on the surface of liquid.

To account for the water sorption processes by the electrolyte, the term S_{lsorp} is introduced as a source term for a rate of mass interchange between the membrane phase and liquid phase across the pore space and electrolyte interface. The expression reads

$$S_{lsorp} = \begin{cases} k_{la} \frac{\rho_m}{EW_m}(\lambda_w - \lambda_l^*) & \text{for absorption} \\ k_{ld} \frac{\rho_m}{EW_m}(\lambda_w - \lambda_l^*) & \text{for desorption} \end{cases} \tag{3.52}$$

in which ρ_m and EW_m refer to the membrane density and weight equivalent at dry state. The parameters k_{la} and k_{la} are the sorption coefficients for the absorption and desorption processes, respectively. The term λ_l^* denotes the equilibrium value of water content corresponding to the liquid state.

When liquid water is generated in the catalyst layer it dissolves into the ionomer and fills up the pores. The network of pores in this domain can be envisioned as a network of connected capillary tubes, of different and varying diameters, filled with varying amounts of water. Each partially filled pore contains an air-water interface with a curved meniscus. Here, the movement of liquid water is dominated by the pressure drop across the menisci or a capillary pressure, P_c. The capillary pressure is expressed as

$$P_c = P_l - P_g = \frac{2\gamma}{r} \tag{3.53}$$

where P_l is the liquid pressure, P_g is the gaseous pressure , γ is the surface tension, and r is the radius of curvature.

Capillary pressures can be positive or negative depending on the direction of curvature of the interface. If the liquid does not wet the capillary (contact angle $\theta_c > 90°$), the radius of curvature lies in the liquid phase and has a positive sign, which makes P_c positive. The pore will repel the water out. If the liquid wets the capillary (contact angle $\theta_c < 90°$), the radius of curvature lies outside the liquid phase and has a negative sign which makes P_c negative or, effectively, a capillary suction, and thus, water will be sucked into the pores. Capillary pressures increase in absolute magnitude as the pore size decreases, so small pores fill first in wetting systems and last in non-wetting systems.

$$P_l = P_g - P_c \tag{3.54}$$

To account for the convective flow of liquid water, D'Arcy's law is applied

$$\mathbf{v}_l = -\frac{\kappa_{l,k}}{\mu_l} \nabla \cdot P_l \tag{3.55}$$

where $\kappa_{l,k}$ is the permeability of the liquid water in the domain k. This value can be obtained from the relationship

$$\kappa_{l,k} = \kappa_{abs} \cdot \kappa_{rl,k}(s) \tag{3.56}$$

where κ_{abs} denotes the absolute permeability of the completely water-filled porous medium. $\kappa_{rl,k}(s)$ is the relative permeability of liquid phase in the porous medium domain k which depends upon the saturation level and empirically defined as

$$\kappa_{rl,k}(s) = \begin{cases} s^{\vartheta} & \text{for wetting phase} \\ (1-s)^{\vartheta} & \text{for non-wetting phase} \end{cases} \tag{3.57}$$

It should be noted that the relative permeability used for the liquid saturation calculation has a different formula in the literature. Berning and Djilali [115] and Pasaogullari et al. [116], for instance, assumed that the relative permeability is a linear function of liquid saturation where as Lou et al. [117] use a function of 4^{th} order to calculate the same parameters. Others treat this parameter in different values for GDL and CTL. An example is in [118], in which the authors used $\vartheta = 3$ for CTL

and 4.5 for GDL in accordance with the high porosity of fibrous porous medium (0.6 to 0.8).

For a porous medium, the relationship between the capillary pressure and saturation is commonly described using Leverette's empirical formula

$$\Im(\zeta) = 1.417\zeta - 2.12\zeta^2 + 1.262\zeta^3 \tag{3.58}$$

Where ζ is s for non-wetting phase and (1-s) for wetting phase.

Employing the above relationship, the capillary pressure is

$$P_c = \gamma_\theta \Im(s) \tag{3.59}$$

where γ_θ is the surface tension of water at the point of contact.

$$\gamma_\theta = \gamma cos\theta_c^k \sqrt{\frac{\varepsilon_k}{\kappa_k}} \tag{3.60}$$

where k is the domain considered, and the terms in the square root represent the mean pore radius. θ_c^k denotes the contact angle of water and pore wall in domain k. γ is the interfacial tension for pure water in contact with its vapour phase [119].

$$\gamma = 235.8 \left(1 - \frac{T_{sat}}{T_c}\right)^{1.256} \left\{1 - 0.625 \left(1 - \frac{T_{sat}}{T_c}\right)\right\} \tag{3.61}$$

where T_{sat} is the vapour saturation temperature, and T_c is the critical point temperature of pure water (374.15°C). The unit of γ in this equation is in millinewtons per meter.

Thus the governing equation for liquid water transport corresponding to the domains can be summarized as

$$\frac{\varepsilon_k \rho_l}{M_w}\frac{\partial s}{\partial t} - \nabla \cdot \left(\frac{\varepsilon_k \rho_l}{M_w}\mathbf{v}_l\right) = \begin{cases} S_{cond/evap} & \text{in } \Omega 1\&5 \\ S_{cond/evap} + \Lambda_w S_{lsorp} & \text{in } \Omega 2 \\ S_{product} + S_{cond/evap} + \Lambda_w S_{lsorp} & \text{in } \Omega 4 \end{cases} \tag{3.62}$$

3.1.5 Modelling energy transport in the MEA

The energy equations in fuel cell modelling can be derived from the conservation of energy, which accounts for a balance of heat flux from conduction, convection and radiation within the three phases of polymer, liquid and gas. With the assumption that the local thermal equilibrium holds and the fuel cell surface is cooled down to get to an equal temperature as the environment, the heat transfer between phases and that due to radiation may be neglected. The effects of ohmic losses within the membrane are taken into account by an additional source term in the energy balance equation. Additionally, energy generation(condensation) and consumption(evaporation) due to phase change are also accounted for [80, 118, 120, 121]. The transient energy effect associated with the mass storage within the domain is taken into account and is

proportional to a volume fraction in each domain. The general energy equation reads

$$\varepsilon_k \frac{\partial \sum_{\beta=1}^{n}(s_\beta \rho_\beta C_{p,\beta} T)}{\partial t} + \nabla \left(\varepsilon_k \sum_{\beta=1}^{n}(s_\beta \rho_\beta C_{p,\beta} T) \right) - \nabla \left(k^{eff} \nabla \cdot T \right) = \sum_{x=1}^{n} S_x \quad (3.63)$$

where, on the right hand side, the first term accounts for the time-dependent energy stored in the domains, the second term is the heat fluxes of all phases in the domains, and the last term represents the heat conduction due to the temperature gradient. β denotes the phase of the species and n is the number of phases. k refers to k^{th} domain. k^{eff} is the effective thermal conductivity obtained from a volume average of each species and materials

$$k^{eff} = \varepsilon_k \left(1 - s\right) k_{porespace} + \varepsilon_k \left(1 - s\right) k_{ionomer} + \varepsilon_k s k_{liquid} + \varepsilon_k k_{agg} \quad (3.64)$$

Here k_{pore}, $k_{ionomer}$, k_{liquid}, k_{agg} are the thermal conductivity of matrix, ionomer, liquid water and that of average value of agglomerates, respectively. Finally, ε_k is the volume fraction of quantities being considered in the k^{th} domain. Table 3.6 summarizes the values used in the computation. The source terms in the above energy equations account for a reversible reaction heat generation, an exothermic reaction loss, energy from phase change and ohmic heat losses. Given that S_η is the heat generation from the reversible reaction, S_{RX} is the exothermic reaction, S_phase is the energy involved in phase change process and S_ohm denotes the ohmic heat loss, each energy source term can be detailed as the following.

The heat generation according to thermodynamic irreversible of change of entropy, S_η, is

$$S_\eta = -\triangle s_{a,c} T_k \frac{\mathbf{i}}{nF} \tag{3.65}$$

where T is the local temperature in the domain, $\triangle s_{a,c}$ is the entropy change associated with the charge transfer in the chemical reactions at the anode and cathode, and n is the number of electrons transferred.

The activation loss, S_{RX}, from the exothermic reaction at each sides is given by

$$S_{RX} = (\eta \mathbf{i})_{a,c} \tag{3.66}$$

in which η is the activation overpotential. The energy due to the phase change process, S_{phase}, depends upon the amount of mass transfer between phases. The driving force in this process is the difference in the amount of water molecules above the liquid film and the pore saturation level. In this work, we assume that the rate of mass transfer is fast enough to keep the system at equilibrium. Thus the relation is

$$S_{phase} = h_L \cdot k_w \left(p_w - P_{sat}\right) \tag{3.67}$$

where h_L is the latent heat for liquid water and k_w denotes the rate of mass transfer across phase boundaries.

The ohmic heat loss, S_{ohm} $[J \cdot m^{-3}]$, can be expressed as

$$S_{ohm} = \epsilon_s \sigma_{s,k} \left(\frac{\partial \phi_s}{\partial x} \right)^2 + \epsilon_m \sigma_m \left(\frac{\partial \phi_m}{\partial x} \right)^2 \tag{3.68}$$

where σ is the conductivity of porous media. ϵ denotes the volume fraction of phases being considered in the domain. Table 3.4 summarizes the variables in the governing equations which need to be solved.

3.2 Finite Element Solution

This section provides a description of the numerical discretization method and technique used for solving the set of model equations. The finite element method was chosen for this work because of the flexibility that it allows in handling arbitrary geometries and applying the boundary conditions, which are particularly useful for future model development.

3.2.1 Discretization and grid independent

The complete set of mathematical model equations is implemented into the commercial software package, COMSOL Multiphysics 3.2b. The COMSOL platform was selected in this study because, although not as numerically efficient as codes based on CFD methodology, it offers much greater flexibility in new model development and

implementation. COMSOL features generic partial differential equations (PDEs), with the flexibility to change the coefficients of predefined PDEs or to create new ones from the general equation (weak forms).

Finite Element Scheme

As shown in Figure 2.1(b), the MEA is subdivided into small rectangular elements (mesh). The physics of one element is approximately described by degrees of freedom (DOFs), a finite number of dependent variables of unknown functions for each node. Each element is assigned a set of characteristic equations describing physical properties, boundary conditions, with an imposed force function, which are then solved as a set of simultaneous equations to predict the object behaviour in that node. The set of linear equations discretized above is rewritten in a general matrix formation of equation as

$$\mathbf{J}(\mathbf{u}^{(n)})\Delta\mathbf{u}^{(n+1)} = -R(\mathbf{u}^{(n)}) \tag{3.69}$$

where $\mathbf{J}(\mathbf{u}^{(n)})$ is the Jacobian matrix consisting of all coefficients in the model equations. $\Delta\mathbf{u}^{(n+1)}$ is the predictor-corrector which becomes the solution of the equation if $R(\mathbf{u}^{(n)})$, which is the discretized residual equation, goes to zero or obtains the error limit.

The governing equations are implemented into the solver in the form

$$d_j\frac{\partial u_j}{\partial t} + \nabla \cdot \Gamma_j = F_j \tag{3.70}$$

in which u_j presents the dependent variable which is needed to be solved. d_j is mass coefficient of the system j, and Γ_j is the summation of fluxes in the domain being considered. In the above general vector form, the first time derivative term accounts for the time-following accumulation of mass of the variable. The second term takes care of all diffusive and convective fluxes which respect to the variable u. The final term takes into account all source terms in the equations.

Grid independent solution

Grid independence solutions were obtained for both 2D and 1D-t models. For the 2D model, the set of solutions obtained from repeating the calculation on a series of successively refined grids from 114 cells to 900 cells which correspond to a range of 6200-46008 degrees of freedom are plotted in Figure 3.3 showing the grid dependency of the current density on the degree of freedom.

3.2.2 Solution technique

For the 2D steady-state simulations, all time-derivatives in the governing equations are set to zero, the boundary conditions listed in table 3.2 are applied. A stationary nonlinear solver and a direct solver using Guassian elimination in COMSOL Multiphysics package is employed with a relative estimated error of less than 10^{-10}. The relative estimated error is defined as

$$err = \left\{ \frac{1}{N} \sum_i \left(|E_i| / W_i \right)^2 \right\}^{0.5} \tag{3.71}$$

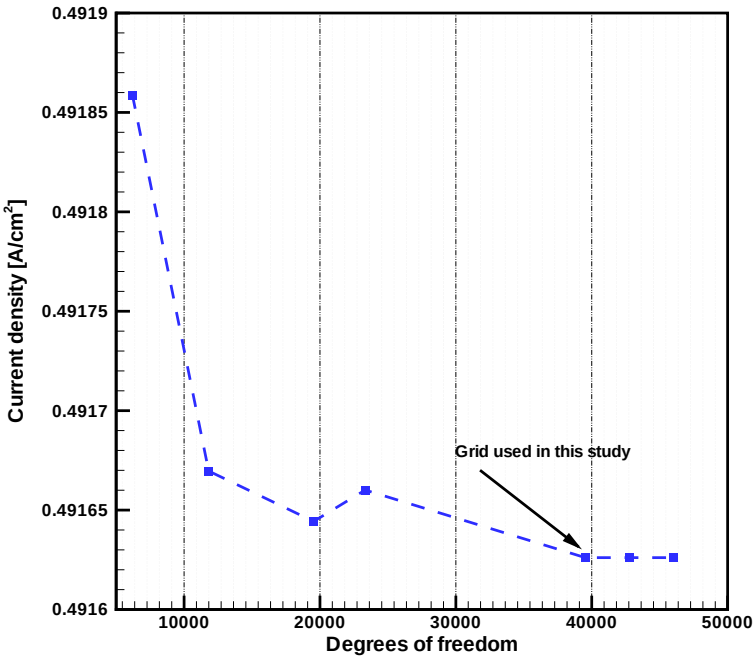

(a) Current density at dV = 0.5V

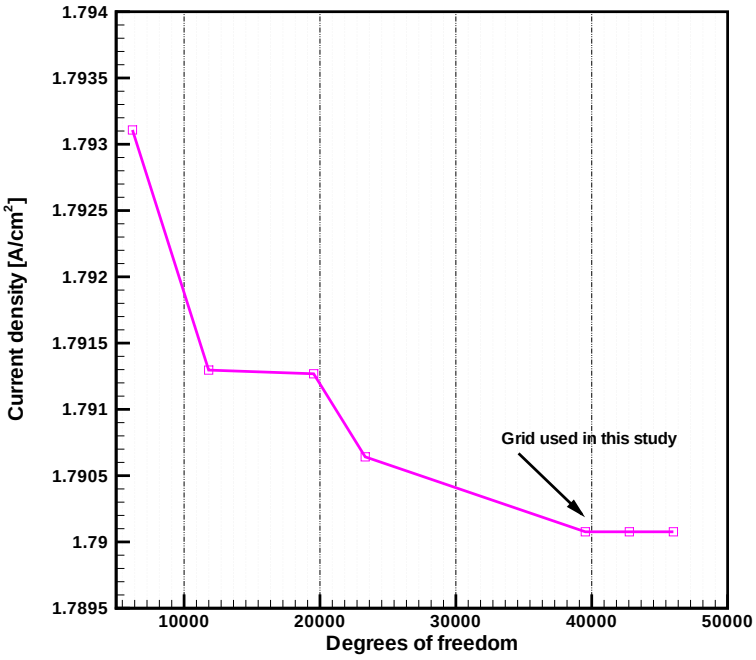

(b) Current density at dV = 1.0V

Figure 3.3: Grid independence investigation: the degree of freedom dependence of solutions for current densities obtained at (a)voltage drop across cell is 0.5 V and (b) 1.0 V

where E_i is the estimated error of the current approximation to the true solution vector. N is the number of degrees of freedom. W_i is the weight factors. Specific details regarding the solver can be found in the software manual [122].

From Equation (3.69), the value of the residual vector $\mathbf{u}$, at the starting point is $\mathbf{u}^0$ (initial guess). The solver forms the linearized model (the initial solutions) using these guessed values, and then computes the updated values with a new set of solutions $\mathbf{u}^{(1)} = \mathbf{u}^{(0)} + \alpha_d \delta\mathbf{u}$, where α_d denotes the damping factor. The relative error, err, is estimated by solving Equation (3.69) as $\mathbf{J}'(\mathbf{u}^{(0)})\mathbf{E} = -R(\mathbf{u}^{(1)})$. If $\mathbf{E}$ gives the relative error larger than the previous step, the solver reduces the damping factor and recalculates $\mathbf{u}^{(1)}$. This procedure is repeated until the relative error has reached a value less than the previous iteration. The solver then proceeds to the next Newton iteration. A damped Newton method is used for solving the non-linear equation system in both steady-state and time-dependent cases.

For time-dependent solutions, a method of lines discretization is used. The solver is an implicit time-stepping scheme which uses the backward Euler differentiation formula. Time stepping is selected to ensure proper resolution of the transients of interest. Due to nonlinearity of the source terms coupling the transport equations, a series of pre-solutions obtained from steady state simulations were used to initiate the solution of the set of unsteady non-linear partial differential equations.

3.2.3 Computational domains and boundary conditions

Two-dimensional computing domains

The two-dimensional geometry used for modelling 2D steady-state case is shown in Figure 2.1(b). The dimensions and geometry parameters of each component for the base case are listed in Table 3.8. The anode electrode computational domain consists of sub-domains Ω_1 for the gas diffusion layer and Ω_2 for the catalyst layer. Sub-domain Ω_3 represents a polymer membrane. Sub-domains Ω_3 and Ω_4 are for the gas diffusion layer and catalyst layer. Structured orthogonal grids are applied to all domains due to the simplicity of the MEA geometry. The number of elements in each domain and degrees of freedom are specified similar to those in [109] for a comparison which is discussed in the next section.

Boundary conditions

The boundary conditions for a 2D steady-state model are imposed corresponding to Figure 3.1(b), and the computational domains in which each governing equation is solved. At the boundaries $\partial\Omega_1$ of a solid matrix, a voltage drop across the MEA, dV, is imposed for a solid potential, ϕ_s. This relates to the set-up of the overpotential, η_i, in the above kinetic models. The relationship between the cell voltage and the voltage drop across the MEA can be expressed as

$$V_{Cell} = E^{th} - dV \tag{3.72}$$

in which E^{th} is the theoretical cell voltage, and is given by

$$E^{th} = 1.229 - 8.456 \times 10^{-4}(T - 298.15) + 4.31 \times 10^{-5}T(ln(p_{H_2}) + \frac{1}{2}ln(p_{O_2})) \quad (3.73)$$

where p_{H_2} and p_{O_2} are partial pressures of hydrogen and oxygen in the system, respectively. On the boundary $\partial\Omega_{17}$, the solid potential is set to be zero. At the interface between the catalyst layers and membrane, because Nafion membrane is an protonic-exchange polymer there is no electrons flowing across this boundaries. Therefore, on the boundaries $\partial\Omega_7$ and $\partial\Omega_{10}$ the Neumann zero conditions are applied and this is for all the solid potentials on the remaining boundaries. For the proton transport equation, Equation (3.14and 3.47), the boundaries considered are $\partial\Omega_4$ and $\partial\Omega_{13}$. According to that protons move in theory through only membrane phase, the Neumann zero boundary conditions are applied for the ionic potential on both boundaries as well.

At the boundary $\partial\Omega_2$ a water vapour mole fraction $x_{H_2O,a}$ is specified as a constant boundary condition (Dirichlet boundary condition). Fick's law holds for gas transport in the porous electrode while the boundary condition for hydrogen transport at this boundary is a balance of the mole fraction of the humidified hydrogen gas according to the mass conservation law. Hence, x_{H_2} = 1 - $x_{H_2O,a}$. The water vapour mole fractions on both sides are calculated from the water activity in the channels, $a_{w,c}$

and $a_{w,a}$ for the cathode and anode respectively, via equation

$$C_{H_2O,i} = RH_i \frac{p^{sat}}{p_g} \tag{3.74}$$

where RH_i is the relative humidity in the GDL/channel interfaces(i=a,c); subscripts a and b indicate the anode and cathode, respectively. p^{sat} is the saturation pressure $[Nm^{-2}]$ and P_g is the total pressure in the channels $[Nm^{-2}]$. The saturation pressure is a function of temperature and the relation is given by

$$log_{10}p^{sat} = -2.1794+0.02953(T-273)-9.1837\times10^{-5}(T-273)^2+1.4454\times10^{-7}(T-273)^3 \tag{3.75}$$

Similarly, at boundaries $\partial\Omega_{16}$, the Dirichlet boundary conditions for oxygen mole fraction, x_{O_2}, and water vapour mole fraction, $x_{H_2O,_c}$ are applied, The inlet boundary of the cathode is set as a constant. The condition for nitrogen gas at this boundary can be obtained from x_{N_2} = 1 - x_{O_2}-$x_{H_2O,_c}$.

At the interface between the membrane and catalyst layers, $\partial\Omega_4$ and $\partial\Omega_{13}$, the gas species are assumed not to penetrate the pore space in the membrane. That is, the gas fluxes through the membrane are taken to be zero. All remaining boundaries are set as (Neumann) zero fluxes.

Table 3.2: Boundary conditions for 2D steady-state model

	Boundaries								
Variable	$\partial\Omega_1$	$\partial\Omega_2$	$\partial\Omega_4$	$\partial\Omega_7$	$\partial\Omega_{10}$	$\partial\Omega_{13}$	$\partial\Omega_{16}$	$\partial\Omega_{17}$	elsewhere
ϕ_e	dV	$\nabla N_{\phi_e} = 0$	i.b.	$\nabla N_{\phi_e} = 0$	$\nabla N_{\phi_e} = 0$	i.b.	$\nabla N_{\phi_e} = 0$	0	$\nabla N_{\phi_e} = 0$
ϕ_p	-	-	$\nabla N_{\phi_p} = 0$	i.b.	i.b.	$\nabla N_{\phi_p} = 0$	-	-	$\nabla N_{\phi_p} = 0$
x_{H_2O}	$\nabla N_w = 0$	$x^0_{H_2O,a}$	i.b.	$\nabla N_w = 0$	$\nabla N_w = 0$	i.b.	$x^0_{H_2O,c}$	$\nabla N_w = 0$	$\nabla N_w = 0$
x_{O_2}	-	-	-	-	$\nabla N_{O_2} = 0$	i.b.	$x^0_{O_2}$	$\nabla N_{O_2} = 0$	$\nabla N_{O_2} = 0$
λ	i.b.	i.b.	$\nabla N_\lambda = 0$	-	-	$\nabla N_\lambda = 0$	i.b.	i.b.	$\nabla N_\lambda = 0$

Note: Superscript ^{0} denotes the inlet condition, i.b. refers to the internal boundary and (-) unused boundaries

Table 3.3: Boundary conditions for 1D time-dependent model

	Boundaries					
Variable	x_1	x_2	x_3	x_4	x_5	x_6
ϕ_e	dV	i.b.	$\nabla N_{\phi_e} = 0$	$\nabla N_{\phi_e} = 0$	i.b.	0
ϕ_p	-	$\nabla N_{\phi_p} = 0$	i.b.	i.b.	$\nabla N_{\phi_p} = 0$	-
x_{H_2O}	$x^0_{H_2O,a}$	i.b.	$\nabla N_w = 0$	$\nabla N_w = 0$	i.b.	$x^0_{H_2O,c}$
x_{O_2}	-	-	-	$\nabla N_{O_2} = 0$	i.b.	$x^0_{O_2}$
λ	-	$\nabla N_\lambda = 0$	i.b.	i.b.	$\nabla N_\lambda = 0$	-
s	$\nabla N_s = -h_s \cdot s$	i.b.	$\nabla N_s = 0$	$\nabla N_s = 0$	-	$\nabla N_s = -h_s \cdot s$
T	$N_T = -h_T(T - T_o)$	i.b.	i.b.	i.b.	i.b.	$N_T = -h_T(T - T_o)$

One-dimensional computational domain

Figure 1.3(c) shows the computational domain for the 1D-t simulations with geometry data listed in Table 4.1. For boundary and node labels inside the domain, x_i is assigned for each node. Therefore x_1 and x_6 denote the anode and cathode outer nodes, x_2 and x_5 are the nodes at the GDL/catalyst interface on the anode, and x_3, x_4 refer to those on the cathode.

Boundary conditions

Table 3.3 summarizes the boundary conditions for a 1D-t model, for the boundaries and computational domain shown in Figure 3.1(c). The governing equations are solved numerically using a time-dependent solver in COMSOL Multiphysics 3.2b. Similar to the inlet boundaries conditions set in the 2D case, the solid potential, ϕ_s, water vapour mole fraction, x_{H_2O}, and oxygen mole fraction, x_{O_2}, are prescribed at the inlet boundaries x_1 and x_6. In addition to gas and charge transport, the liquid water and energy transport are taken into account in the 1D-t model. For liquid water transport at the interface between the gas channels and the GDLs, x_1 and x_6, are assumed to be expelled out to the gas channels. In the literature, this was treated slightly differently. For instance, Shah at al. [80] implemented the steady-state flux of liquid water, which is related to water film thickness in the gas diffusion layer. Others assumed either a zero saturation or zero liquid water flux at this location or along portions of the channel/GDL interface [48, 50, 116, 123]. In this thesis, liquid water accumulation is assumed to be in the GDLs and transported to the GDL/channel

interface, x_1 and x_6, through capillary flow. The boundary conditions imposed at x_1 and x_6 are then fluxes of liquid water regulated by the amount of accumulated liquid water at the interface

$$\nabla N_s = -h_l s \tag{3.76}$$

where h_l is the rate of mass transfer of liquid water at the interface of the gas channel. In fact, the saturation at the GDL/channel interface depends on the gas flow in the channel, current density and wettability (contact angle). In order to compare the thermal effect of operating temperature and heat management in air-breathing fuel cells a non-isothermal submodel in which all temperature dependent variables are taken into account. The thermal boundary conditions at the inlet boundaries, x_1 and x_6, are treated with two different schemes: controlled temperature and heat flux due to free convection. For the constant temperature scheme, the boundary temperature is set to the temperature of the reactants or the cooling channel temperature. Contrary to fixed temperature boundaries, the rate of heat transfer between the GDL surface boundaries and the environment in a natural convection scheme is controlled by the thermal gradients between the ambient temperature, T_o and the GDL surface, T_s, and the concentrations gradients of oxygen and vapour in the air stream. The boundary condition at the inlet boundaries is given by

$$\begin{cases} T(x_i) = T_i & \text{for constant temperature} \\ \nabla N_T = -\frac{A_v}{A_s} h_T (T_s - T_o) & \text{for natural convection} \end{cases} \tag{3.77}$$

where N_T refers to the heat flux across the interface GDL/channel (x_1 and x_6). A_s is the surface area of a planar fuel cell. h_T denotes the convective heat transfer coefficient which can be described by a dimensional heat transfer coefficient, $< Nu >$, the Nusselt number. Thus the heat transfer coefficient, h_T, can be determined using the equation below

$$h_T = \frac{< Nu > k}{l} \tag{3.78}$$

where $< Nu >$ is the Nusselt number averaged over the heat transferred area, and k is the air thermal conductivity. l denotes the characteristic length of the fuel cell. The determination of the convective heat transfer coefficient for an air-breathing fuel cell, h_T, is mainly based on the analysis in [38, 39], where the hot side of a fuel cell is considered as the heated horizontal flat plate. The relationship between the heat transfer over the plate can be determined using the equation below [38]

$$< Nu >= 0.54k \left(\frac{2g}{\nu\alpha} \frac{\triangle\rho}{\rho L} \right)^{0.25} \tag{3.79}$$

where $\frac{\triangle\rho}{\rho}$ is the relative change of air density over the hot surface. ν and α are the air viscosity and thermal conductivity.

Initial Conditions

As described above, the initial conditions for the time-dependent experimental simulations are prescribed by the steady state pre-solutions. For example, the solutions for 50% relative humidity and 0.5 V are pre-computed and then used as the initial

conditions for the time-dependent simulation to study the behaviour of a MEA under a step change of voltage from 0.5V to 0.8V. It is importance to note that at the initial state, the water activity in electrolyte is equilibrated with water vapour in the pores. Similarly, the initial saturation values for unsteady state simulations are set to the steady state values.

Table 3.4: Dependent variables solved in COMSOL Multiphysics 3.2b solver

Model				Domain					
2D	1D-t	*Variable*		Ω1	Ω2	Ω3	Ω4	Ω5	Equation no.
✓	✓	Solid potential	ϕ_e	✓	✓		✓	✓	(3.12 and 3.45)
✓	✓	Electrolyte potential	ϕ_p		✓	✓	✓		(3.14 and 3.47)
✓	✓	Hydrogen mole fraction	x_{H_2}	✓	✓				(3.10)
✓	✓	Oxygen mole fraction	x_{O_2}				✓	✓	(3.42)
✓	✓	Water vapour mole fraction	x_{H_2O}	✓	✓		✓	✓	(3.11 and 3.43)
✓	✓	Nitrogen mole fraction	x_{N_2}				✓	✓	(3.44)
✓	✓	Water content	λ_w		✓	✓	✓		(3.28)
	✓	Liquid saturation	s	✓	✓		✓	✓	(3.62)
✓	✓	Temperature	T	✓	✓	✓	✓	✓	(3.63)

Table 3.5: Thickness of Nafion membranes 1100 EW series in dry and hydrated form [124]

Nafion code	Nominal thickness	Dry thickness $[\mu m]$	Hydrated Thickness $[\mu m]$
112	51	50± 2	58± 3
1135	89	91± 2	111± 2
115	127	141± 3	161± 5
117	178	183± 3	208± 5

Table 3.6: Source terms used in energy equation [80]

Symbol	*Sources of heat*	*Expressions*
$S_{reversible}$	electrochemical reactions	$-\triangle s_{a,c} T_k \frac{i}{F}$
$S_{activation}$	activation losses	$(\eta i)_{a,c}$
S_{ohmic}	ohmic	$\epsilon_s \sigma_k \left(\frac{\partial \phi_s}{\partial x}\right)^2 + \epsilon_m \sigma_m \left(\frac{\partial \phi_m}{\partial x}\right)^2$
$S_{phasechange}$	phase-change	$h_L \cdot k_w \left(P^w - P^{sat}\right)$

Table 3.7: Properties of parameters used in simulations

Symbol	*Parameter*	*Value*	*Unit*	*References*
ρ_l	density of liquid water	1000	kgm^{-3}	
M_{H_2O}	molar mass of liquid water	18^{-3}	$kgmol^{-1}$	
μ_l	liquid water viscosity	10^4	$Wm^{-1}K^{-1}$	
κ_{abs}	absolute permeability of CTL(GDL)	$10^{-13}(8.7 \times 10^{-12})$	$m^2 s$	[80]
k_{cond}	condensation rate constant	1.0	s^{-1}	[118]
k_{evap}	evaporation rate constant	5×10^{-5}	$Pa^{-1} \cdot s^{-1}$	[118]
$H_{H_{2,N}}$	Henry's law constant for hydrogen dissolved in Nafion	6.69×10^4	$Pa \cdot m^{-3} mol^{-1}$	[125]
$H_{O_{2,N}}$	Henry's law constant for oxygen dissolved in Nafion	3.16×10^4	$Pa \cdot m^{-3} mol^{-1}$	[125]
c_f	fixed charge concentration in membrane	1.8×10^3	$molm^{-3}$	[126]
$-\triangle s_a$	entropy associated with HOR	163.7	$Jmol^{-1}K^{-1}$	[80]
$-\triangle s_c$	entropy associated with ORR	0	$Jmol^{-1}K^{-1}$	[80]

3.3 Validation

Prior to applying the model developed to investigate the dynamic phenomena in PEMFC, simulations using the 2D fuel cell model for the MEA were conducted using the properties listed in Table 3.8 and 3.9. The resulting polarization curve is compared to the experimental work by Bender et al. [127] and the modelling work of Secanell [109]. Moreover, the details of the resulting data including the distributions of reactants, volumetric current density, overpotential, water vapour relative humidity and membrane water content are also presented.

Comparison of performance curves

Figure 3.4 shows the computed and experimental polarization curves. Simulation results were obtained for isothermal, non-isothermal and two phase non-isothermal modes. For the non-isothermal mode, the current densities agree well with the experimental data at low current density regime. The overestimations, however, are obtained at high current density. This can be explained in two possible ways. First, the isothermal model does not account for the effects of temperature on the local thermal properties of reactants in the system, such as diffusivity, soluability and water content, which essentially affect the performance of the fuel cell. Furthermore, more water produced at higher current densities. Consequently, water may condense in the pores and limit reactant transport to the cathode. This results in a decreased performance at the high current densities. With the non-isothermal model, the performance

Table 3.8: Membrane electrode assembly geometry and operating conditions used for 2D model validation [109]

Parameter	*Value*	*Unit*
Dimensions: anode GDL thickness, L_a^{GDL}	250×10^{-6}	[m]
anode CL thickness, L_a^{CTL}	10×10^{-6}	[m]
membrane thickness, L^m	89×10^{-6}, Nafion^{TM} 1135	[m]
cathode CL thickness, L_c^{CTL}	10×10^{-6}	[m]
cathode GDL thickness, L_c^{GDL}	250×10^{-6}	[m]
Cell operating conditions:		
T	353	[K]
Anode operating conditions:		
p	3	[atm]
x_{H_2}	0.8833	[-]
x_w	0.1167 (75%RH)	[-]
Cathode operating conditions:		
p	3	[atm]
x_{O_2}	0.1855	[-]
x_{N_2}	0.6978	[-]
x_w	0.1167 (75%RH)	[-]
Membrane properties:		
membrane weight equivalent, EW	1100	$[g \cdot mol^{-1}]$
membrane weight equivalent, ρ_{dry}	2.0	$[g \cdot mol^{-1}]$
Absorption(desorption) vapour-liquid-membrane water transfer rate:		
vapour-membrane, $k_{va}(k_{vd})$ [27]	$10^{-5}(10^{-5})$	$[s^{-1}]$
liquid-membrane, $k_{la}(k_{ld})$ [80]	10(10)	$[s^{-1}]$

Table 3.9: Gas diffusion layer and catalyst layer properties used for 2D model simulation [109, 127]

Parameter	Symbol	*Value*	*Unit*
Densities			
platinum	ρ_{Pt}	21.5	$[g \cdot cm^{-3}]$
carbon	ρ_C	2.0	$[g \cdot cm^{-3}]$
Nafion(dry)	ρ_m	2.0	$[g \cdot cm^{-3}]$
Diffusion coefficients			
hydrogen	D_{H_2}	3.4952×10^{-5}	$[m^2 \cdot s^{-1}]$
oxygen in nitrogen	D_{O_2,N_2}	9.1368×10^{-6}	$[m^2 \cdot s^{-1}]$
Water vapour in nitrogen	D_{H_2O,N_2}	9.8919×10^{-6}	$[m^2 \cdot s^{-1}]$
hydrogen in Nafion	$D_{H_2,N}$	12.8×10^{-9}	$[m^2 \cdot s^{-1}]$
oxygen in Nafion	$D_{O_2,N}$	8.71×10^{-10}	$[m^2 \cdot s^{-1}]$
Electrical properties			
GDL conductivity in x-direction	$\sigma_{s,x}^{GDL}$	1603	$[S \cdot m^{-1}]$
GDL conductivity in y-direction	$\sigma_{s,y}^{GDL}$	2727.8	$[S \cdot m^{-1}]$
CTL conductivity	σ_s^{CTL}	8884	$[S \cdot m^{-1}]$
Structural properties			
GDL porosity	ϵ_V^{GDL}	0.6	[-]
platinum loading	m_{Pt}	0.2	$[mg \cdot m^{-2}]$
platinum—Carbon ratio	$Pt\|C$	0.2	[-]
Agglomerate pellet properties			
radius	r_{agg}	1	$[\mu m]$
electrolyte film thickness	δ_{agg}	80	$[nm]$
volume fraction of electrolyte in an agglomerate	ϵ_{agg}	0.35	[-]
Electrochemical properties	*Anode*	*Cathode*	
anodic-anodic transfer coefficient, α_{aa}	0.5	-	[-]
anodic-cathodic transfer coefficient, α_{ac}	0.5	-	[-]
cathodic-cathodic transfer coefficient, α_{cc}	-	1	[-]
Butler-Volmer coefficient, γ	0.25	-	[-]
reference concentration, $c_{H_2}^{ref}, c_{O_2}^{ref}$	56.4	7.25	$[mol \cdot m^{-3}]$
exchange current density, i_0^{ref}	10^4	2.707×10^{-4}	$[mol \cdot m^{-3}]$

curve shows better agreement with the experimental data, compared to the isothermal model. This single phase model, however, is not able to capture the losses at high current density. A two-phase submodel is incorporated into the non-isothermal model in order to account for liquid water in the pore electrodes. The effect of liquid water saturation on the performance of the fuel cell is illustrated in figure 3.4. As expected, a lower cell voltage is obtained in the high current density regime. This can be interpreted as partial flooding. Qualitatively, the trend of predicted performance agrees well with that reported by Ye et al. [118], in which the resulting performance polarization curves from a single and two-phase model were compared.

To further verify the implementation of the developed model, a comparison was performed of the isothermal simulation results with the in-house code developed by [109], which is based on a finite element method. The result presented in terms of a performance characteristic curve based on 2D model simulation is shown in figure 3.5. The resulting performance curves are identical. Note that the model developed by Secanell et al. was for optimization purposes and is confined to isothermal single-phase conditions whereas the model in this study includes non-isothermal and two-phase sub-models that significantly enhance the predictive capabilities.

In addition to the performance characteristic curves, the transport phenomena in the MEA are also studied using the 2D non-isothermal two-phase model. Figures 3.6 to 3.14 show the simulation results including the transport phenomena and the distributions of the variables of interest in the MEA at three different operating conditions

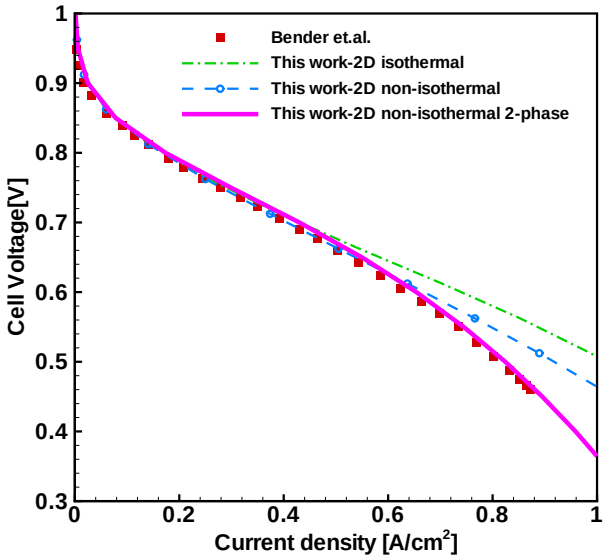

Figure 3.4: Comparison of polarization curves obtained from this study (line) and from Bender et al. (square)at the operating parameters in Table 3.8

specified by the voltage drops across the MEA. The voltage drops chosen are 0.4, 0.6 and 1.0 volts corresponding to current densities of 182, 812 and 1781 mA/cm^2 at cell voltages of 812, 612 and 212 mV. The cell voltages correspond to the voltage drops across the MEA via Equation (3.72). These operating conditions are chosen because they highlight the dominant transport phenomena at different operating conditions. The transport phenomena in an MEA can be considered in two main regions: the area under the gas channel and the area under the current collector. In the figures, a white dashed line across an electrode delineates those two regions. An upper section represents the area under a flow channel and the lower one is the area under current collector.

Transport phenomena in MEA

Figure 3.6, 3.7, 3.13 and 3.14 show the concentration distributions of hydrogen, oxygen and water vapour in corresponding electrodes for three different current densities. Throughout the simulations in this section, the concentrations of feed reactants at the boundaries under the flow channels are fixed for all three operating conditions and are given in table 3.2. The oxygen concentration distribution for three different current densities are shown in Figure 3.7. It is clear that the concentration within the catalyst layer is lower at the flow channel/GDL interface. Moreover, it is limited to a narrow region as current density is increased, as observed in Figure 3.7(c). The normal isocontours of the other two GDL boundaries boundary compared to the zero flux condition. As seen, the concentration under the channel is higher than that under the current collector. Oxygen diffuses from the boundary under the flow channel into other parts of domain mainly due to a concentration gradient. With a pure diffusion model, a diffusion coefficient plays a crucial role on the gradient of gas concentration, which also depends upon a rate of consumption by a reaction at the catalyst layer. This provides the estimate of the limiting current density of the cell and gives rise to a concentration polarization at high current density operation. Likewise, a similar distribution profile of hydrogen concentration at the anode can be observed in Figure 3.6. Quantitatively, the hydrogen concentration gradient is less than the oxygen concentration gradient, Noting that the amount of hydrogen consumed by the reaction is half of that of oxygen.

Charge transport in MEA

Figures 3.8 to 3.11 show the volumetric current density and the corresponding overpotential across the MEA at the anode and cathode catalyst layers for three different cell voltage drops across the MEA: 0.4 V (182 mA/cm^2), 0.6 V (812 mA/cm^2) and 1.0 V (1781 mA/cm^2). The effect of decreasing the voltage at boundaries $\partial\Omega_1$ and $\partial\Omega_{17}$ on the local current density and overpotential can be observed in Figure 3.9 to 3.11. The potential difference imposed at the boundaries drives the reactions in the catalyst layers resulting in corresponding current flow across the electrodes. The volumetric current density and overpotential at the anode catalyst layer is separated into two regions, while uniform in the in-plane direction even at high current density. As shown in Figure 3.8, the current is very large and its distribution limited to a narrow band near the catalyst/membrane interface, in comparison to the area close to GDL/CTL interface. This is due to the relatively fast HOR kinetics. On the other hand, the distribution of the volumetric current density and overpotential at the cathode site shown in Figure 3.11 are more broadly distributed from the interface adjacent to the membrane throughout the layer. This is because the oxygen reaction kinetics are much slower than the HOR. This implies that the catalyst layer thickness is a crucial design parameters; the thicker the catalyst layer, the lower platinum utilization becomes, particularly in the anode.

Heat transport in MEA

To further evaluate the model developed, an analysis of the temperature distribution within a MEA is conducted. The main heat source in the fuel cell comes from the exothermic ORR at the cathode catalyst layer. Based on the diffusive model approach, resistive heating plays a significant role in the membrane and the catalyst layers. The non-uniform temperature profiles across the MEA at different operating conditions are depicted in Figure 3.12. Generally, the temperature across the MEA is not much different due to the large thickness to length ratio, i.e. very thin MEA. The temperature difference of 4°C can, however, be observed at high current density regimes compared to 1°C when operated at low current density. This value agrees well with that reported by Birgersson et al [128]. Moreover, the heat generation is much higher under the current collector than under the gas channel. The imposed constant temperatures at boundaries $\partial\Omega_2$ and $\partial\Omega_{16}$ dominate the temperature distribution in the MEA. This causes heat fluxes from the middle of the MEA under the gas channel to the solid current collectors.

Water transport in MEA

The performance of the fuel cell relies on an adequate hydration level. The two phase submodel simulates the effect of multiphase water transport on cell performance. The cell polarization curves resulting from the two-phase model depicted in Figure 3.4 shows the effect of liquid water on the cell performance. Current density increases results in higher cell voltage drops. This is primarily due to the increased mass transfer of reactant gas resistance from liquid water blockage. The results and validation data are in very good agreement. However, a noticeable increase in cell potential is also observed at a current density of 0.2 to 0.5 $A \cdot cm^{-2}$. This is because more water is produced at the cathode resulting in higher membrane conductivity. Increasing the current density further causes pore flooding, and the cell performance starts to decrease. Figure 3.16 depicts the resulting liquid saturation distributions within the cathode catalyst layer for three current density values. Similar profiles of liquid saturation in case (a) and (b) can be explained by the low amount of condensed water vapour which corresponds to current densities at the cathode catalyst layer. Increasing the current density results in increased water production. Therefore, the liquid saturation is higher than that at the low current densities and the distribution is non-uniform.

Qualitatively, the water distribution in the membrane and MEA at different operating conditions can be observed in Figure 3.14 to 3.15 for the humidified reactants of 75% relative humidity on both side. The relative humidity of water vapour at

the anode electrode decreases from the same value as the feed stream to 50% when the current density is increased. Figure 3.17 shows the effect of the net flux of water in the membrane on the relative humidity in the MEA. The anode relative humidity decreases when the fuel cell is operated at higher current densities. This can be attributed to the electro-osmotic drag of water to the cathode, which dominates and induces membrane drying. Consequently, the membrane conductivity decreases, and fuel cell performance drops. A cell geometry and configuration like the rib and flow channel can also have an influence to the performance as well. Membrane water transport, for example, is dominated by the cell geometry as shown by the different cross-sectional profiles of water content at two different locations (the middle of the gas inlet (L1) and that of the current collector(L2)). At a low current density of 0.2 A/cm^2, there is no difference in anode water content at these two locations, whereas in the cathode catalyst layer, the water content under the gas channel is higher than under the current collector. This is because more water is produced by the reaction in the area under the gas channel when current density is increased. From Figure 3.7 and 3.10, the under-gas-channel exhibits a higher oxygen concentration than the area under the current collector, resulting in more current production. For high current operations, the more water is evacuated from the anode due to a higher drag coefficient. There is no added-on water from the humidified inlet gas under the current collector, which results in a lower water content at the anode compared to that under the gas channel. At the same operating condition, the water content at the cath-

ode is similar because the water generated by the cathode reaction and the dragged water molecules from the anode are balanced with the water fluxes in the catalyst layer/GDL interface. The effects of cell geometry such as gas channel width and bipolar plate shoulder dimensions on a cell performance are not dealt with in this thesis. More details concerning these particular issues can be found in the literature, for example, [36, 48, 129].

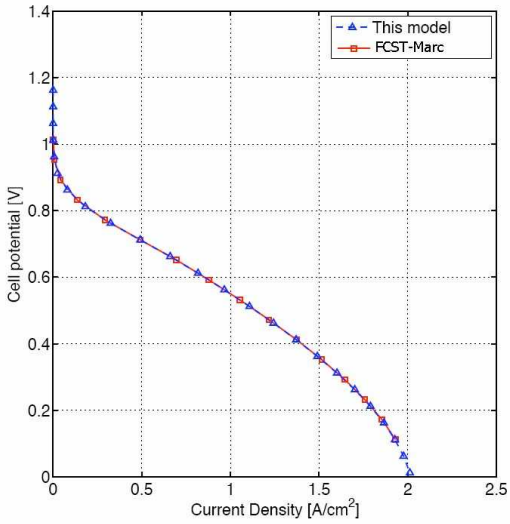

Figure 3.5: Comparison of polarization curves obtained from this study (triangle) and from FCST (square) at the operating parameters in Table 3.8

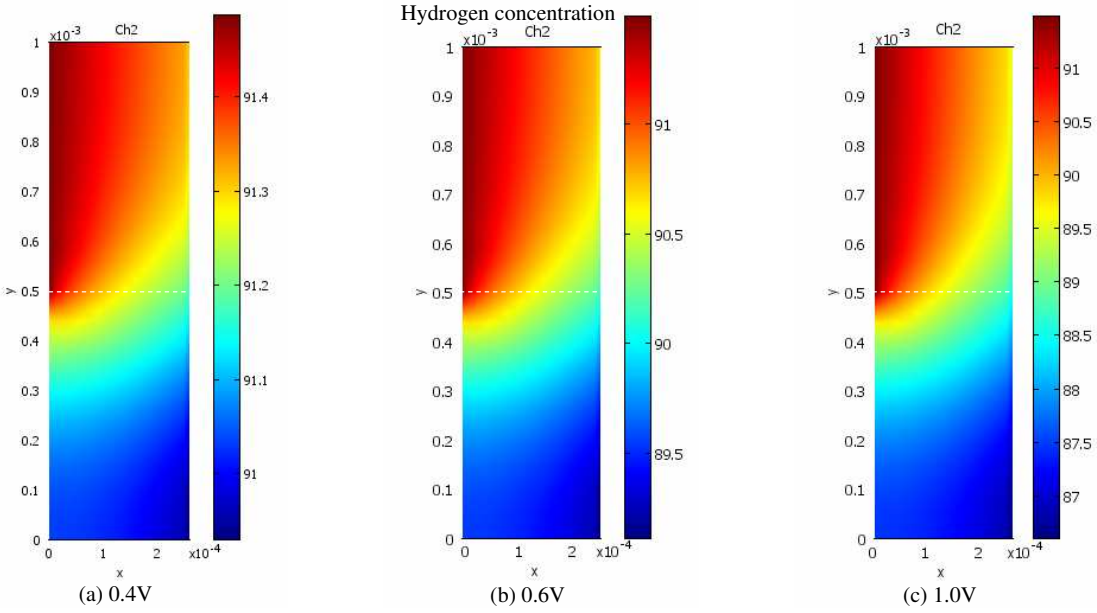

(a) 0.4V (b) 0.6V (c) 1.0V

Figure 3.6: Distribution of hydrogen concentration in anode electrode at voltage drops across MEA of (a) 0.4 V (182 mA/cm^2), (b) 0.6 V (812.97 mA/cm^2) and (b) 1.0 V (1781.2 mA/cm^2), the interface between anode catalyst layer and membrane is on the right.

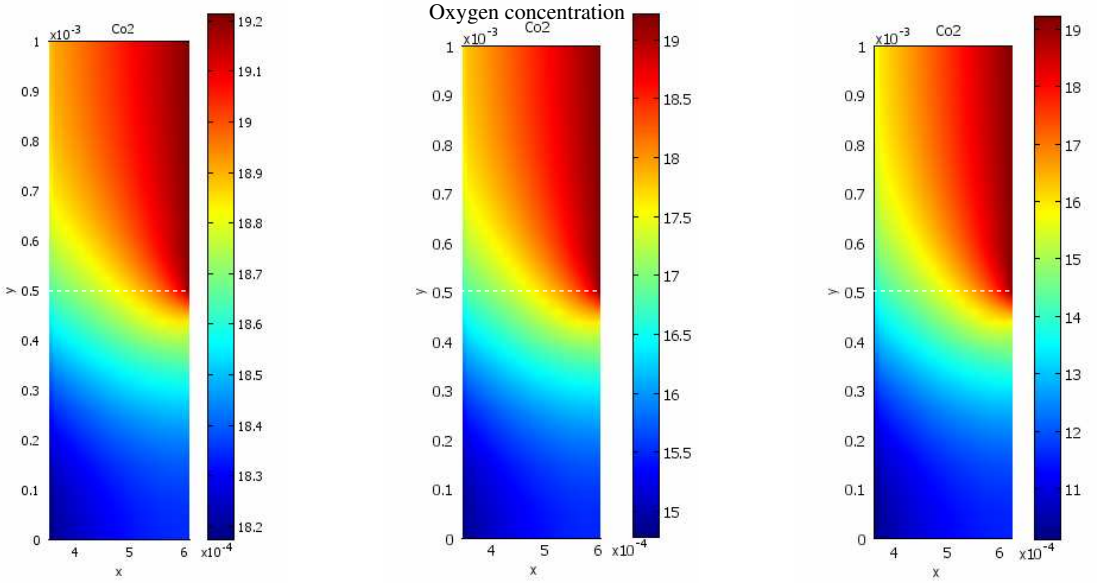

(a) 0.4V (b) 0.6V (c) 1.0V

Figure 3.7: Distribution of oxygen concentration in cathode electrode at voltage drops across MEA of (a) 0.4 V (182 mA/cm^2), (b) 0.6 V (812.97 mA/cm^2) and (b) 1.0 V (1781.2 mA/cm^2), the interface between cathode catalyst layer and membrane is on the left.

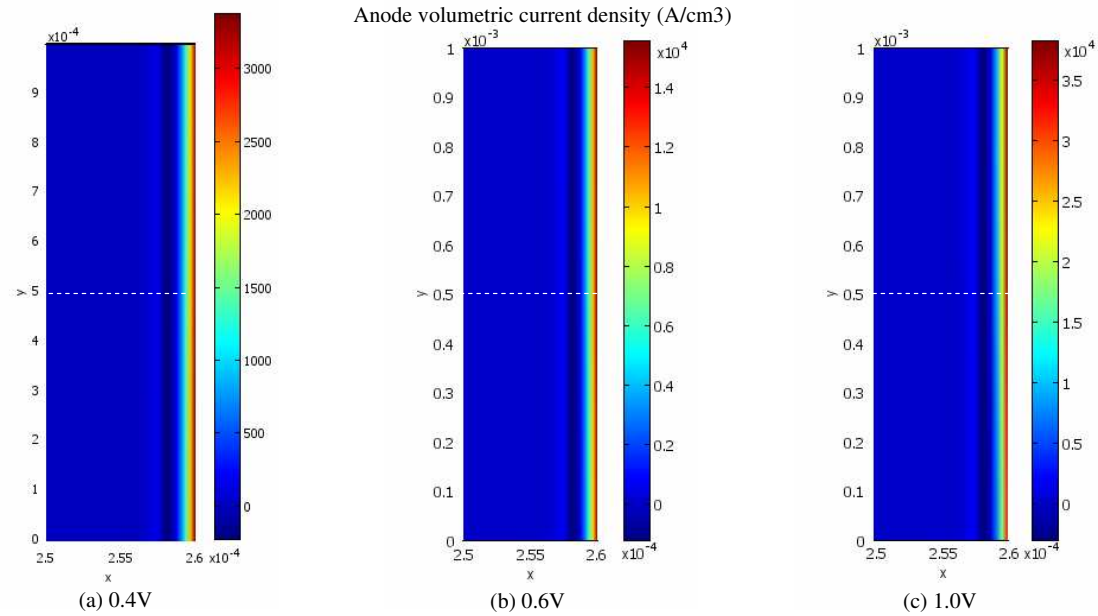

(a) 0.4V (b) 0.6V (c) 1.0V

Figure 3.8: Distribution of volumetric current density in anode catalyst layer at voltage drops across MEA of (a) 0.4 V (182 mA/cm^2), (b) 0.6 V (812 mA/cm^2) and (b) 1.0 V (1781mA/cm^2)

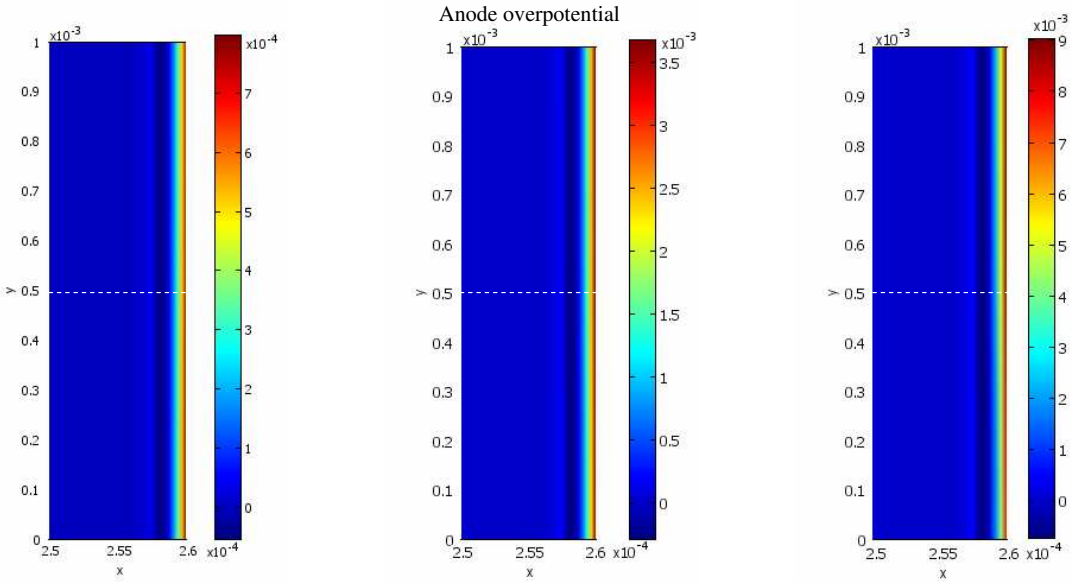

(a) 0.4V (b) 0.6V (c) 1.0V

Figure 3.9: Distribution of overpotential in anode catalyst layer at voltage drops across MEA of (a) 0.4 V (182 mA/cm^2), (b) 0.6 V (812 mA/cm^2) and (b) 1.0 V (1781 mA/cm^2)

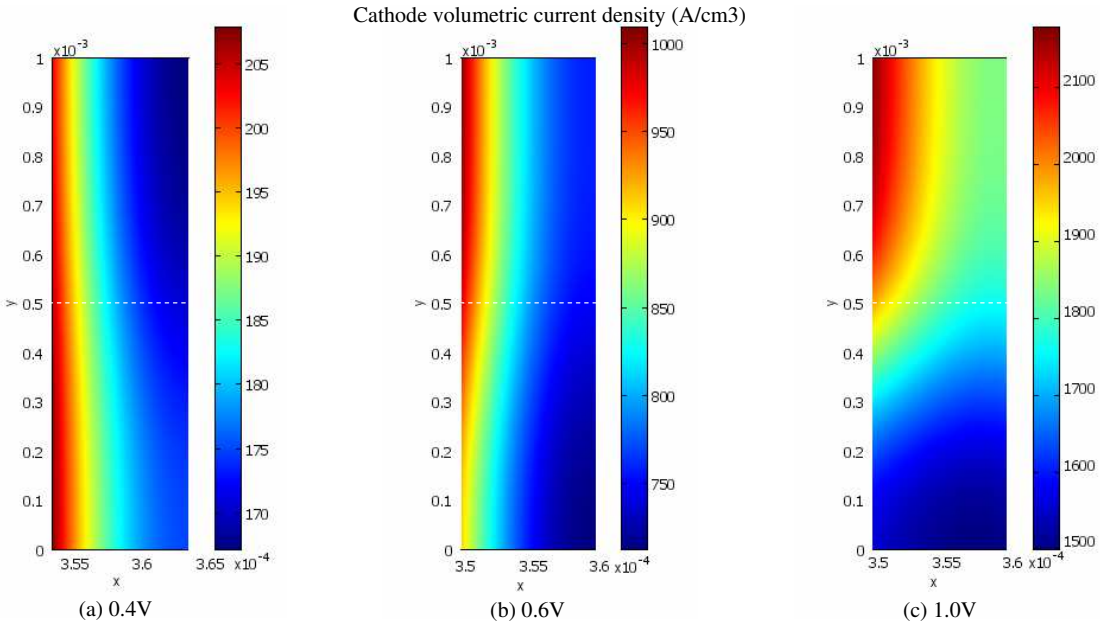

(a) 0.4V (b) 0.6V (c) 1.0V

Figure 3.10: Distribution of volumetric current density in cathode catalyst layer at voltage drops across MEA of (a) 0.4 V (182 mA/cm^2), (b) 0.6 V (812 mA/cm^2) and (b) 1.0 V (1781mA/cm^2)

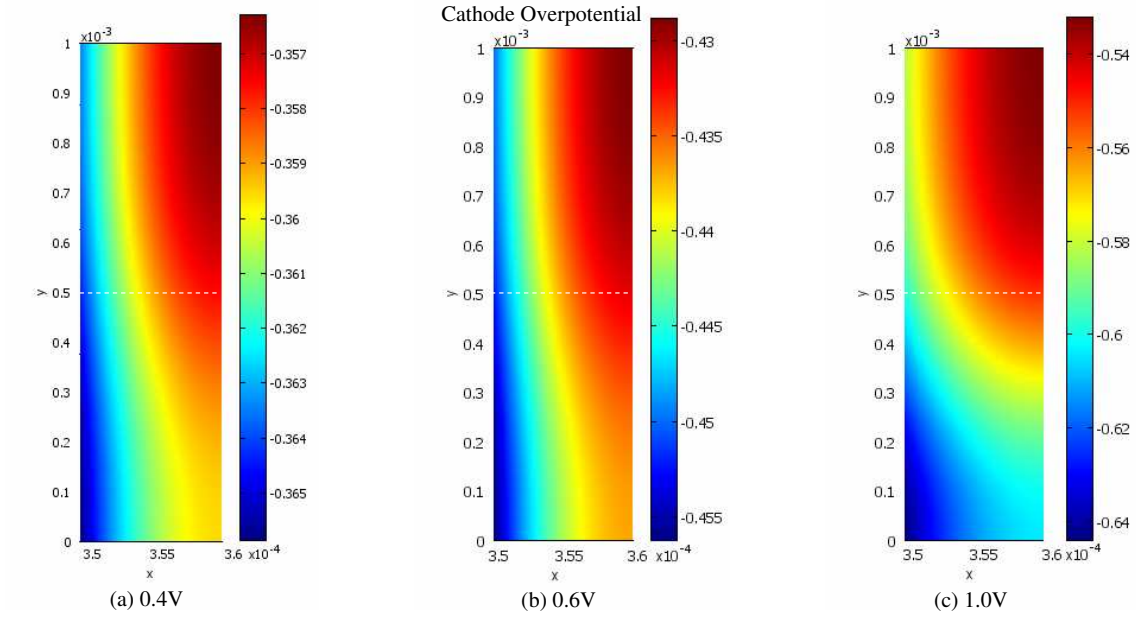

(a) 0.4V (b) 0.6V (c) 1.0V

Figure 3.11: Distribution of overpotential in cathode catalyst layer at voltage drops across MEA of (a) 0.4 V (182 mA/cm^2), (b) 0.6 V (812 mA/cm^2) and (b) 1.0 V (1781 mA/cm^2)

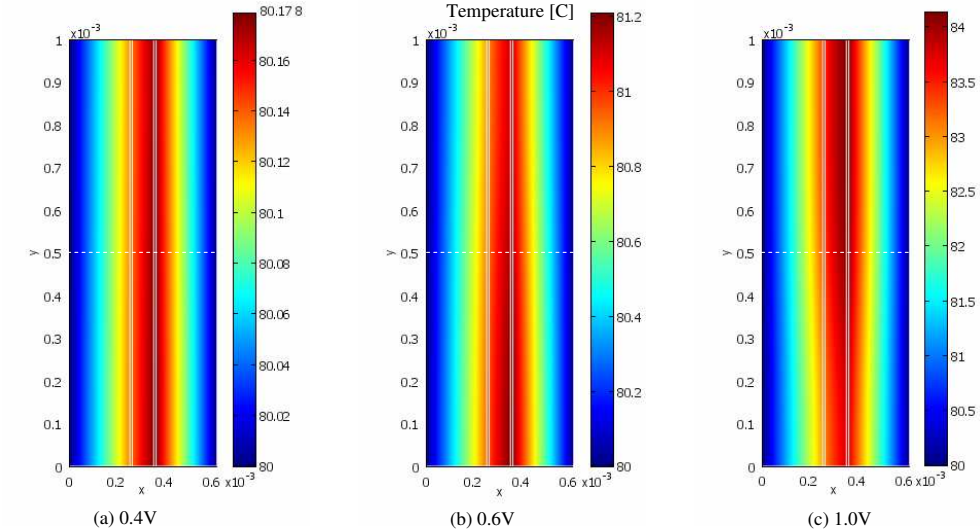

(a) 0.4V (b) 0.6V (c) 1.0V

Figure 3.12: Profiles of temperature in membrane and both catalyst layers at a operating voltage of 0.4, 0.6, 1.0 V (182.45, 812.97 and 1781.2 mA/cm^2)

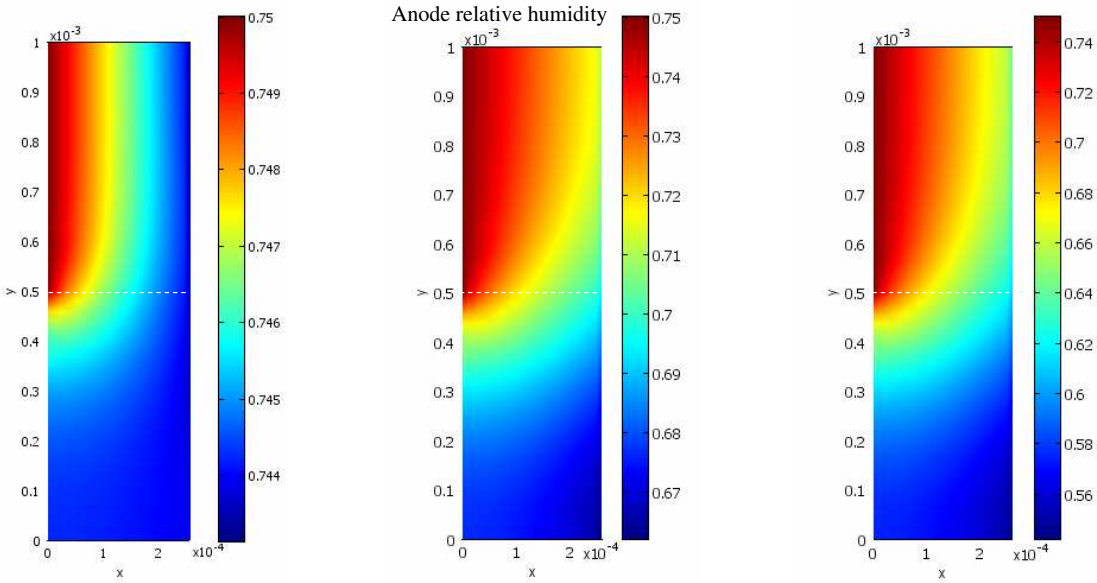

(a) 0.4V (b) 0.6V (c) 1.0V

Figure 3.13: Distribution of relative humidity in anode electrode at voltage drops across MEA of (a) 0.4 V (182 mA/cm^2), (b) 0.6 V (812 mA/cm^2) and (b) 1.0 V (1781 mA/cm^2)

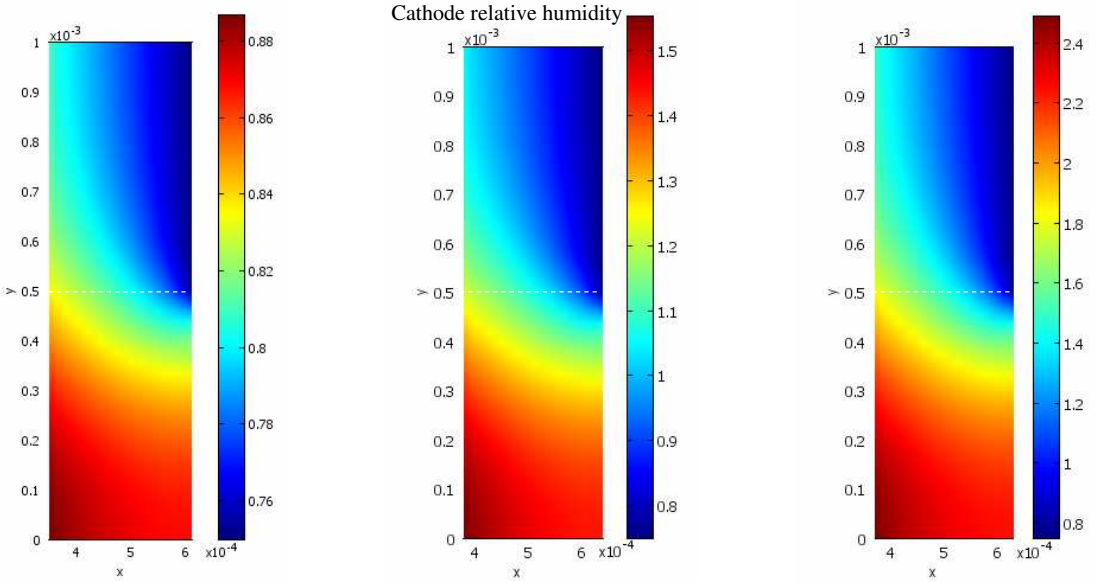

(a) 0.4V (b) 0.6V (c) 1.0V

Figure 3.14: Distribution of relative humidity in cathode electrode at voltage drops across MEA of (a) 0.4 V (182 mA/cm^2), (b) 0.6 V (812 mA/cm^2) and (b) 1.0 V (1781 mA/cm^2)

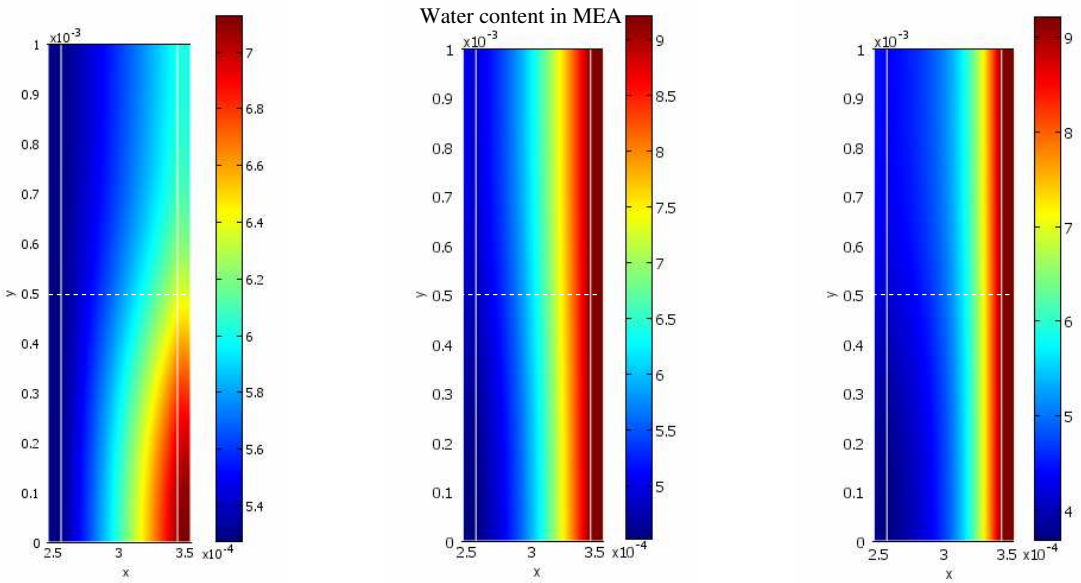

(a) 0.4V (b) 0.6V (c) 1.0V

Figure 3.15: Distribution of water content in MEA at voltage drops across MEA of (a) 0.4 V (182 mA/cm^2), (b) 0.6 V (812 mA/cm^2) and (b) 1.0 V (1781 mA/cm^2)

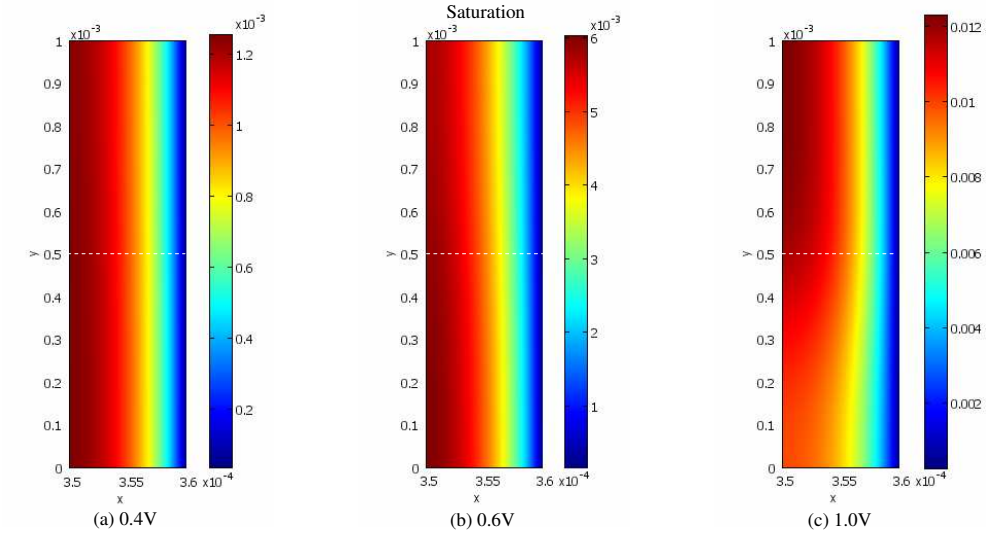

(a) 0.4V (b) 0.6V (c) 1.0V

Figure 3.16: Profiles of liquid saturation in cathode catalyst layer at a operating voltage of 0.4, 0.6, 1.0 V (182, 812 and 1781 mA/cm^2)

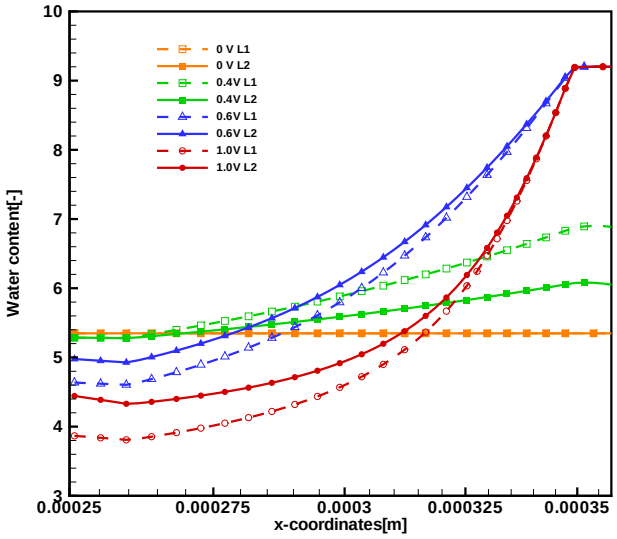

Figure 3.17: Profiles of water content in membrane and both catalyst layers at a operating voltage of 0.4, 0.6, 1.0 V (182, 812 and 1781 mA/cm^2)

Chapter 4

Dynamic Behaviour of PEMFC

In this chapter, the model developed and validated in the preceding chapter is expanded to allow investigation of dynamic behaviour of PEM fuel cells by including time-dependent terms to the set of model equations. Time-dependent simulations, however, require additional computing resources and are time consuming. Therefore, a 1D-t model is employed to solve the model equations in the time domains throughout this chapter. The model base conditions are derived from the literature and from the approximations, which are given in table 4.1. A series of simulations are performed and analyzed to study the effect of various parameters on fuel cell performance.

4.1 Dynamic Performance of PEMFCs

To study dynamic behaviour of a fuel cell under unsteady conditions, voltage sweeps are prescribed as shown in Figure 4.1. The corresponding transient response of current is superimposed on the same plot. The overshoot and subsequent time response in the current output clearly illustrates the dynamic behaviour. The rate of potential sweep is determined based on a water production rate at which a fuel cell generates water while other input parameters are fixed. Throughout the course of the simulations, the potential drop across the fuel cell is swept between 0 to 0.95 V. The evolution of the water saturation through the forward and backward sweeps is shown in Figure 4.2, and the corresponding water flux in the membrane is shown in Figure 4.3. Figure 4.3 also shows the ratio of the electro-osmostic to diffusion fluxes in the membrane. This ratio remains less than unity through most of the forward and backward cycles, except between 200 and 280 seconds (i.e. just prior to the maximum current densities), where it exceeds unity. The corresponding net water flux is thus reversed during this period due to the dominance of the electro-osmotic transport. It should be noted that the flux profiles are markedly asymmetric.

Figure 4.4 shows the resulting current-voltage characteristic curves for the fuel cell at a steady state condition and under a sweep rate of 10 mV/s for the base case. During the potential sweeps, a hysteresis effect is observed in the current-voltage relation. Decreasing voltage during the forward sweep results in increased current densities. During the course of the backward sweep the model predicts lower current

densities compared to that on the forward sweep, particular at low cell voltages and exhibits crossing of the polarization curves. This phenomenon, which is consistent with observations made in recent experimental and theoretical studies [20, 78, 80], is largely due to the different water transport fluxes (asymmetry) at the same current densities on the forward and backward sweeps shown in Figure 4.3 which results in different hydration levels and thus protonic conductivities.

To further investigate causes of the so-called threshold current density, the evolution of the membrane water content is plotted against current density in Figure 4.5. In the steady state condition, the water content profile exhibits an almost symmetrical dome shape. This can be attributed to the fact that more water is generated as the current density increases. However, water content decreases at higher current densities due to the electro-osmotic effect whereby the protons drag water molecules from the anode to the cathode side. In Figure 4.6, at higher current densities (higher overpotential), the water content gradient across the membrane becomes more pronounced as more water is produced at the cathode while the rate of water transport via electro-osmotic drag increases water content with increasing current density as shown in Figure 4.5.

In dynamic mode, water content follows an increasing current density up to 0.85 $A \cdot cm^{-2}$ where it reaches a maximum. The water content then starts declining when the voltage is swept further to the end of the forward course. During the backward potential sweep, current density values are lower at a given voltage that the corre-

sponding values for the forward sweep. This is because the membrane conductivity, which depend on the hydration level, is lower than that on the forward sweep. As the backward sweep continues, the water content in the membrane increases. The backward-sweep current density then is equal as the forward sweep one at 0.6V, the crossover point. It is interesting to note that this does not coincide with the crossing point of the water content.

4.1.1 Effect of operating temperature

The effect of inlet gas temperature on the dynamic current-voltage relation is shown in Figure 4.7. Increasing gas temperature results in increased limiting current densities. The trend is consistent with the experimental work of [130]. The increase in fuel cell performance influenced by the temperature can be described in terms of the increased membrane conductivity as the membrane conductivity is a function of temperature. Accordingly, with a temperature rises from 40 to 80°C the conductivity increases by a factor of 1.5. In unsteady-state operation, the change of potential increases a current density, hence more water is produced at the cathode. At low current density, operation at a temperature of 40°C slightly more efficient than at the higher temperature because of the higher membrane water content as shown in figure 4.8. The coupling between temperature and the finite rate/time constant of the water transport process result in varying water fluxes, as shown in Figure 4.6, between forward and backward sweeps at a given current. In addition, at higher cur-

rent densities the water saturation levels result in partial blockage of the GDL pores inducing further polarization losses.

4.1.2 Effect of operating pressure

In this section, the fuel cell parameters are kept as specified for a base case, while varying the operating pressure. In Figure 4.10, the high pressure-operated fuel cell exhibits, as expected, a higher performance than at lower pressure throughout the sweeps. The threshold/crossover current density shifts gradually to the right of the polarization curve with higher operating pressure, with this occurring at about 0.6 V for the higher pressure. Higher performance is achieved with increasing pressure, particularly during the forward sweeps. Water contents and fluxes under the different operating pressures are shown in Figures 4.11 and 4.12. Differences in membrane water content are most pronounced at higher current densities for low pressure operation and vice-versa for high pressure.

4.1.3 Effect of inlet gas humidity

Figure 4.13 shows the effect of water activity on performance, which improves with hydration, as in static conditions. is observed. This results in an increased performance as the membrane water content increases from hydration process. Operating fuel cell with the base case condition (% RH 1:75 on the anode and cathode, respectively) results in a threshold current density at around 0.6 $A \cdot cm^{-2}$, but there is no

crossover for the other humidification conditions investigated (50:50 and 75:75 %RH) and which exhibit higher performance during the forward sweep at all voltages. It is interesting to point out that at the condition of relative humidities equal 50:50, the performance is lower than the base case. This result suggests that with the proper balance in the membrane water content one can forego hydrogen humidification to reduce system cost since further humidification of the anode does not help improve a performance in this case.

4.1.4 Effect of water sorption rate

As noted earlier, PEMFCs rely critically on the performance of the proton exchange membrane, which is a strong function of water content. The membrane has its own characteristics such as water sorption and swelling. The effect of water sorption rates is presented in Figure 4.16. Base case conditions are assumed and the initial condition is obtained from the steady state solution. Increased water absorption rate results in higher rate of water uptake at the membrane/electrode interfaces and faster humidification and increased performance.

4.1.5 Effect of sweeping rate

The effect of potential sweep on a fuel cell polarization curve is shown in Figure 4.19 for the base case and in Figure 4.21 for the equal inlet gas humidities. As discussed above, with an increased sweep rate, the time evolution current-voltage characteristic

curve deviates from the steady state. Increasing sweeping rate results in an increased membrane water content. However, the time constant for water to reach a new steady state is much slower than for other transport processes. This causes the difference in the slopes of water content in Figure 4.20 and 4.22. In addition, the threshold/crossover current density in the base case moves towards a lower current density. Even though there appears to be no threshold in the latter case as the water in membrane is not in equilibrium, the current density for this case shows a similar trend as reported by [20, 78, 80].

The simulation of a step in the current density on a short time period can provide a useful information for the dynamic performance of fuel cell operated under the time evolution. Figure 4.1 shows the fuel cell response to set of sudden load changes. First, the resulting voltage decreases upon the increase of current density. Moreover, the voltage differences at the same level of a load change also is on the level of membrane hydration and

4.2 Model Application to Air-breathing PEM Fuel Cell

To demonstrate the model application, the current-voltage characteristics of a planar air-breathing fuel cell are simulated. Such fuel cells are of particular interest in low power and portable applications. They rely on passive heat and water management

which afford significant system simplifications but also impart performance characteristics that are quite different from more conventional systems with active cooling and water management [39]. The parameters used in the simulation are given in Table 4.1. Only the boundary condition for the energy equation is different from the previous section as an air breathing fuel cell is designed to work under ambient air conditions. The so-called self-breathing fuel cell performance characteristics are shown in Figure 4.23. Contrary to the results discussed in the previous section, specifically at the low anode inlet gas humidity, there is no indication of a threshold. This can be attributed to a low water potential in the cathode. Additionally, the predicted temperature at the boundary, shown in Figure 4.24, increases from the input gas temperature to 65°C as sweeping potential towards high current density. The exothermic reaction and joule heating are responsible for this increased temperature. The deviation of the temperature from a steady state condition is also captured. The increased current density due to the potential sweep generates more heat. The predicted temperature on the forward sweep is lower than the steady state condition and conversely, the dynamic temperature is higher for the backward sweep course. This can be attributed to a thermal inertia of the materials. It should be noted that heat transferred by radiation is not considered in this model. Consequently, the predicted temperature is higher than that in an actual cell. The model, however, predicts a similar trend of the increased temperature compared to the works of Fabian et al. [38] and Litster and Djilali [39]. In particular the "knee"in the polarization curve at higher current

densities is associated primarily with membrane dry-out rather than mass transport limitations. This is further highlighted by the water content profiles shown in Figure 4.20 which are distinctly different from those for more standard fuel cells.

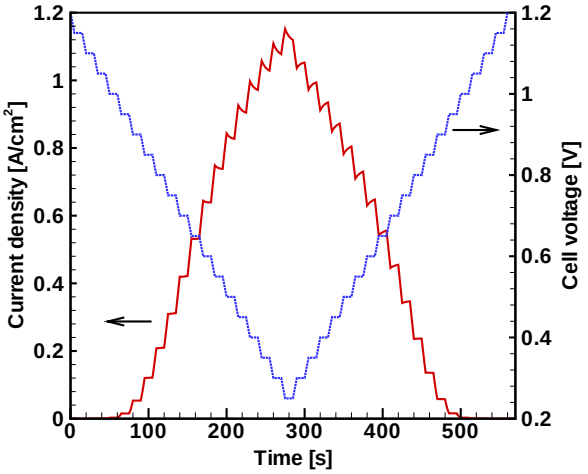

Figure 4.1: Evolution of current density under potential sweeping

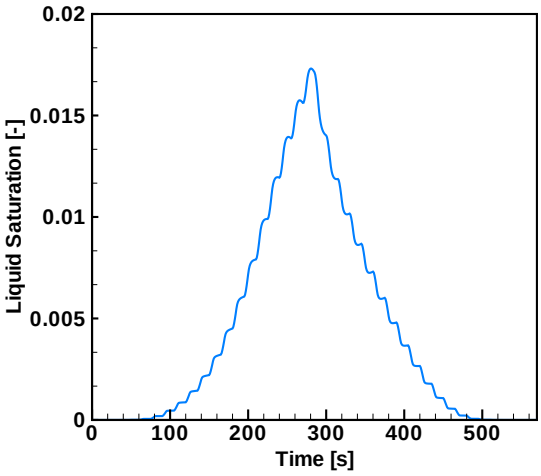

Figure 4.2: Evolution of liquid water in gas diffusion layer under potential sweeping

Table 4.1: Membrane electrode assembly geometry and operating conditions for 1D-t simulation

Parameter	*Value*	*Unit*
anode GDL thickness, L_a^{GDL}	300×10^{-6}	m
anode CL thickness, L_a^{CTL}	10×10^{-6}	m
membrane thickness, L^m	52×10^{-6}, Nafion^{TM} 112	m
cathode CL thickness, L_c^{CTL}	10×10^{-6}	m
cathode GDL thickness, L_c^{GDL}	300×10^{-6}	m
Cell operating conditions		
T	313	[K]
anode operating conditions		
p	3	[atm]
x_{H_2}	0.9999	
x_w	0.0001 (1%RH)	
cathode operating conditions		
p	3	[atm]
x_{O_2}	0.2061	
x_{N_2}	0.7756	
x_w	0.0183 (75%RH)	
Operating conditions for the air-breathing fuel cell		
Cell operating conditions		
T	303	[K]
anode operating conditions		
p	1.34	[atm]
x_{H_2}	0.9996	
x_w	0.0004 (1%RH)	
cathode operating conditions		
p	1	[atm]
x_{O_2}	0.1462	
x_{N_2}	0.8283	
x_w	0.0255 (60%RH)	

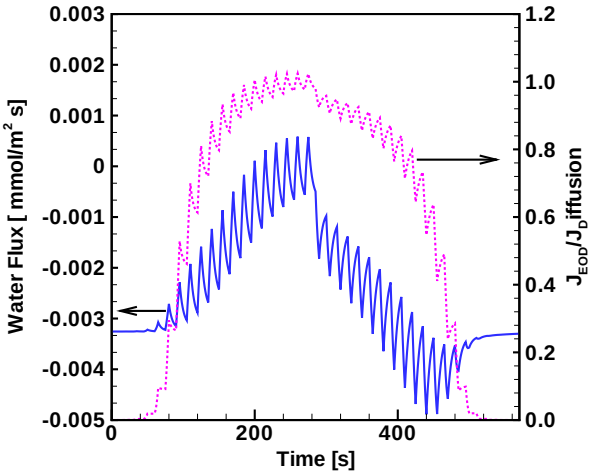

Figure 4.3: Evolution of dissolved water flux in membrane and a ratio of the electro-osmotic flux and the dissolved water diffusion flux under potential sweeping

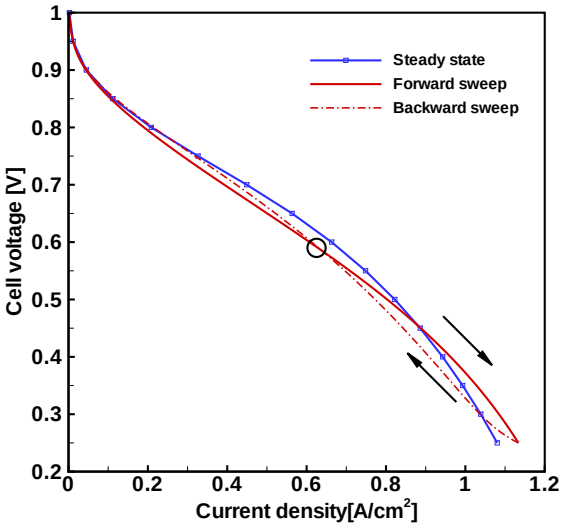

Figure 4.4: Simulation of current density under potential sweeping

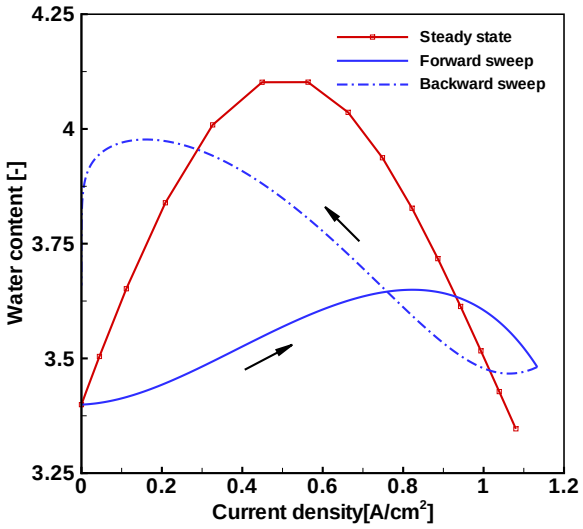

Figure 4.5: Water content under potential sweeping

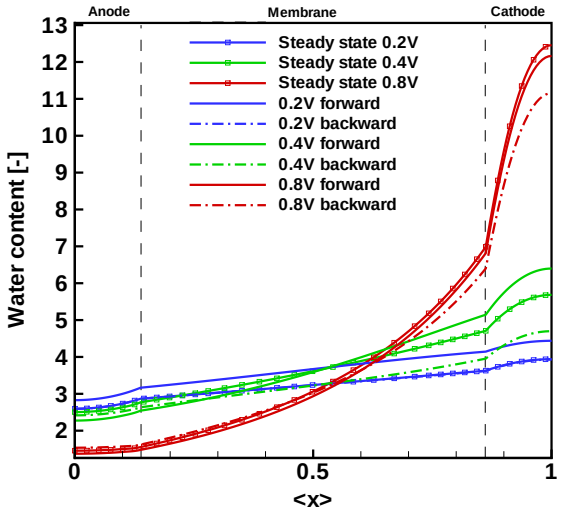

Figure 4.6: Profiles of water content in anode/membrane/cathode at a steady state and under 10 mV/s potential sweep for base case

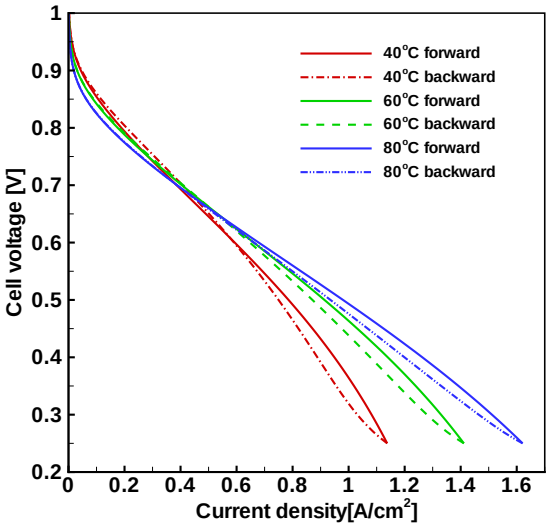

Figure 4.7: Effect of temperature on fuel cell performance during potential sweep

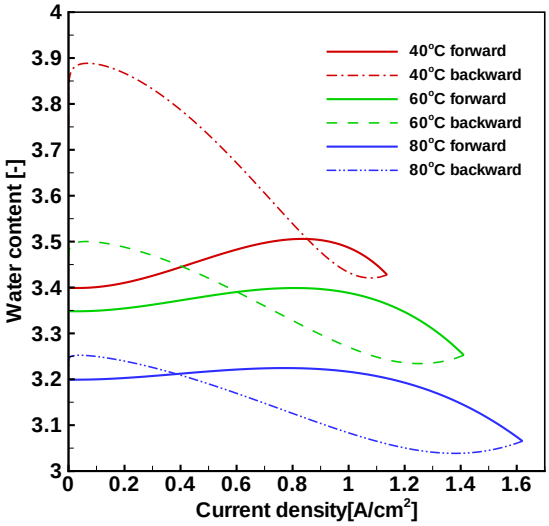

Figure 4.8: Effect of temperature on water content in membrane under 10 mV/s potential sweep for base case

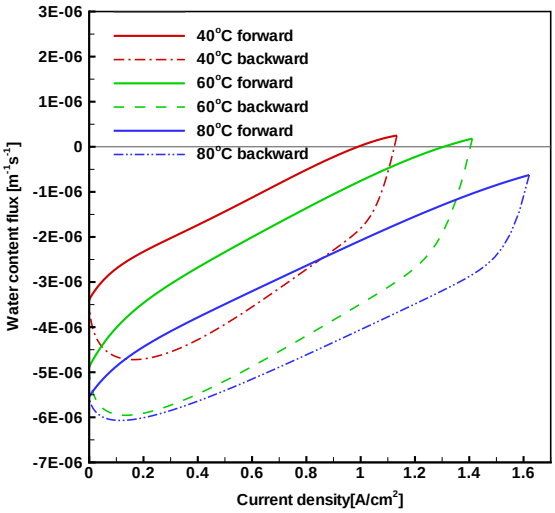

Figure 4.9: Effect of temperature on water flux in membrane under 10 mV/s potential sweep for base case

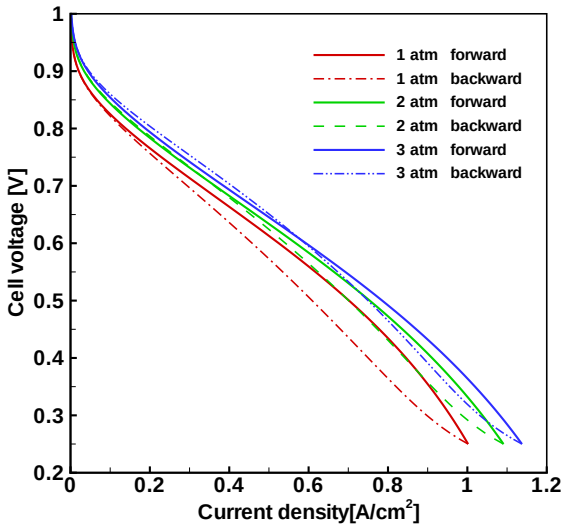

Figure 4.10: Effect of pressure on time dependent current density under potential sweeping

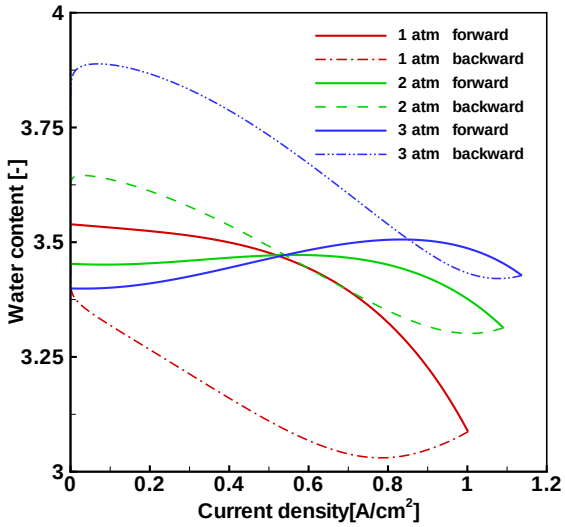

Figure 4.11: Effect of pressure on water content under potential sweeping

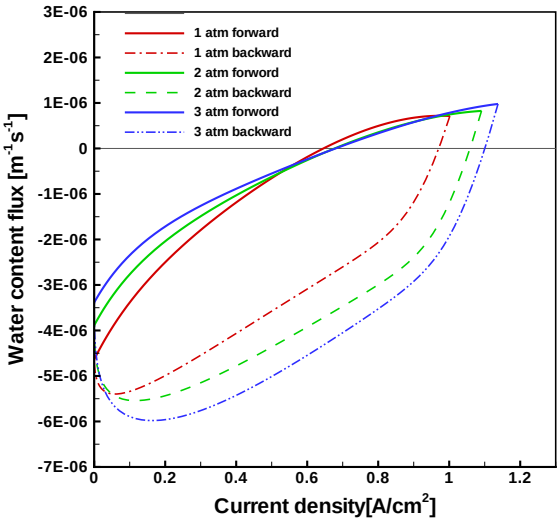

Figure 4.12: Effect of pressure on water flux under potential sweeping

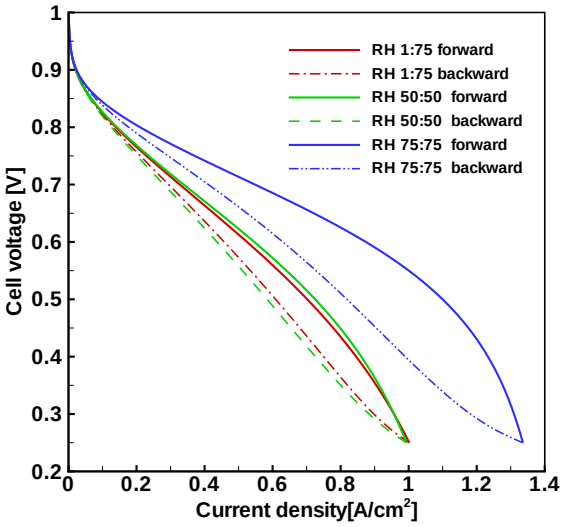

Figure 4.13: Effect of inlet gas humidity on time dependent current density under potential sweeping

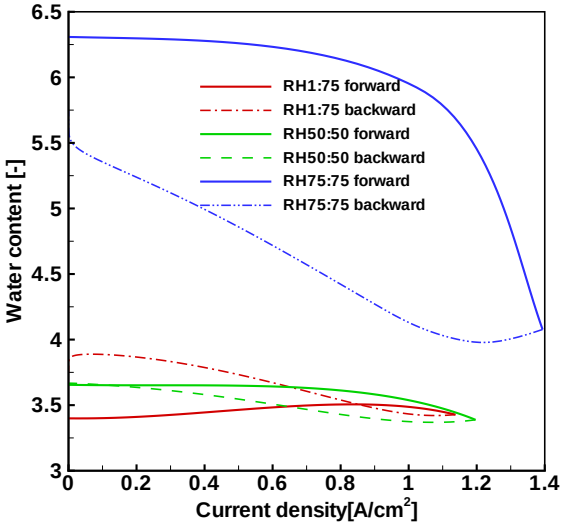

Figure 4.14: Effect of operating temperature and humidity on water content in membrane under potential sweeping

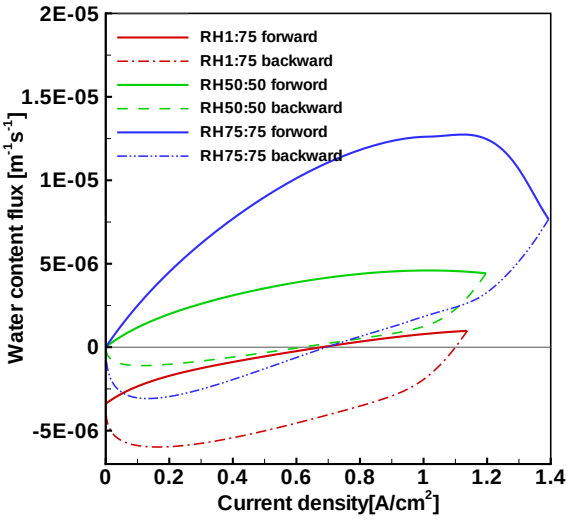

Figure 4.15: Effect of operating temperature and humidity on time dependent water content flux under potential sweeping

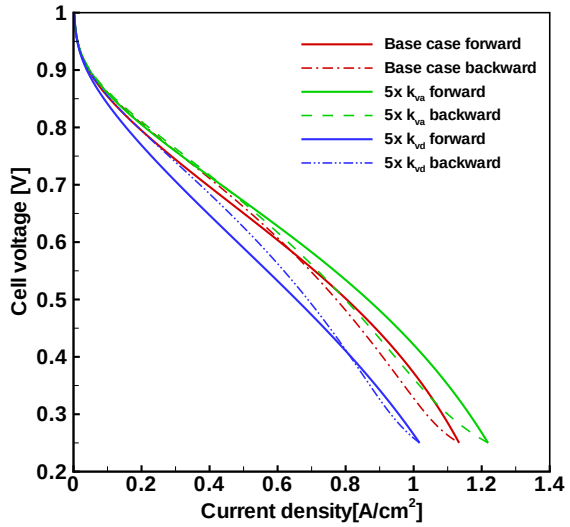

Figure 4.16: Effect of water sorption rates current density under potential sweeping

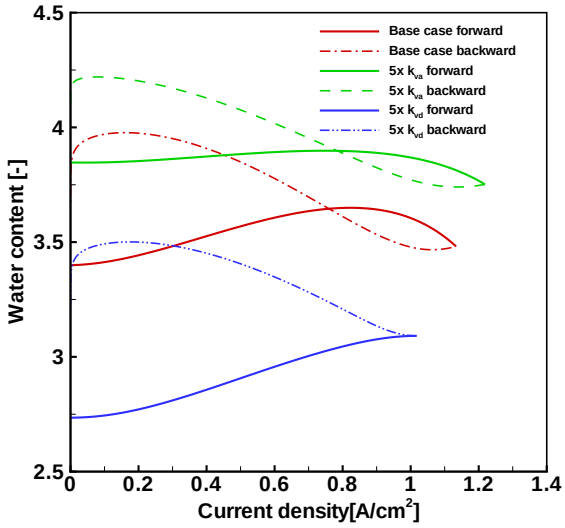

Figure 4.17: Effect of water sorption rates on water content under potential sweeping

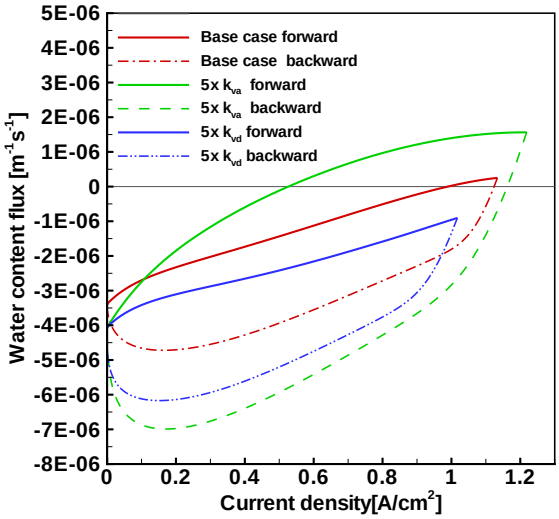

Figure 4.18: Effect of water sorption rates on water flux under potential sweeping

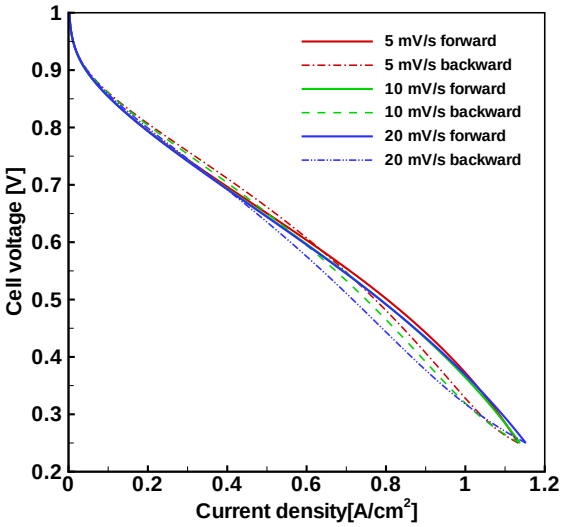

Figure 4.19: Fuel cell performance under different potential sweeping rates

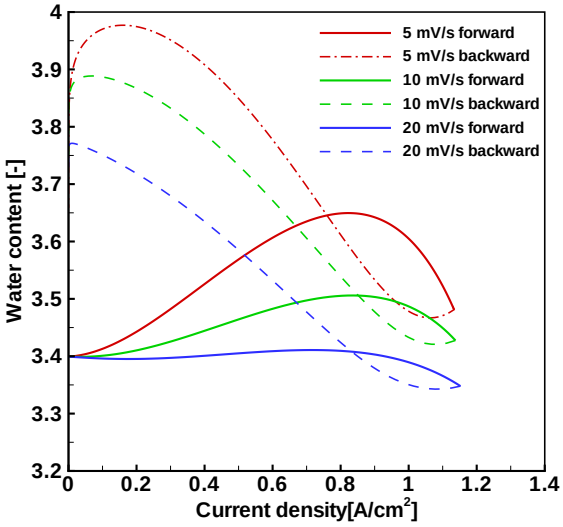

Figure 4.20: Effect of potential sweeping rate on water content in membrane

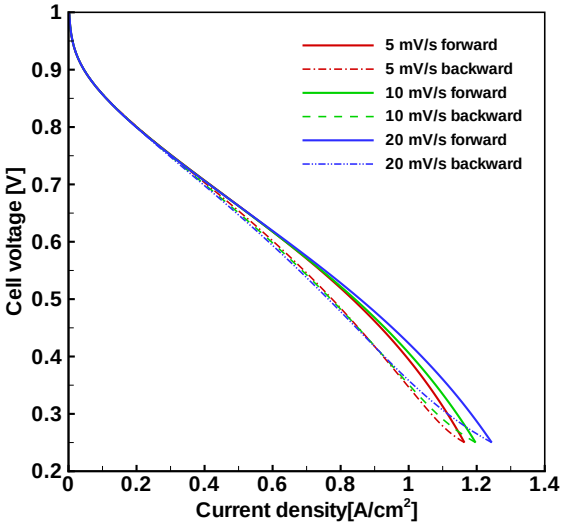

Figure 4.21: Effect of sweeping rate on the fuel cell performance

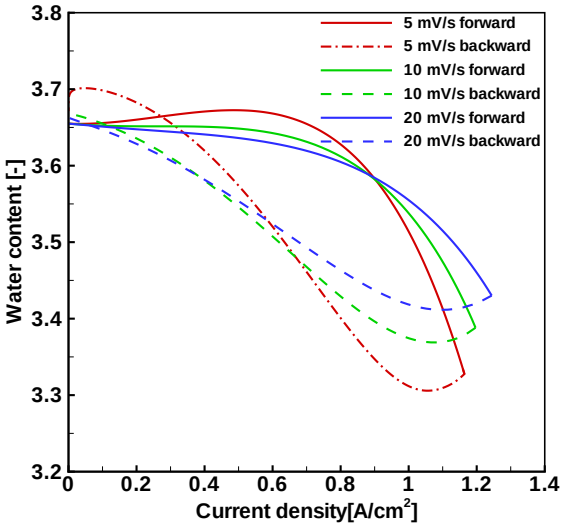

Figure 4.22: Water in membrane under potential sweeping potential (% RH 50:50)

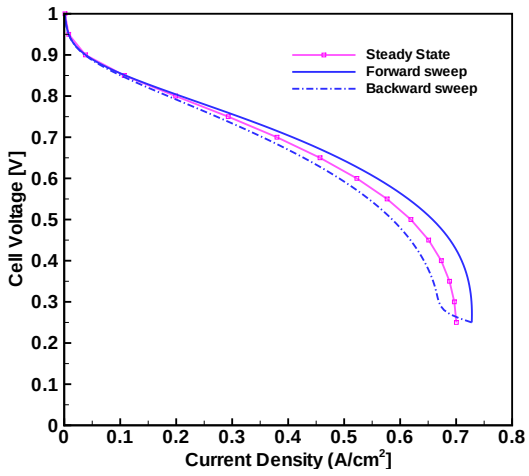

Figure 4.23: Dynamic current response to a potential sweep simulated at RHa=10% RHc=60% T_{amb} = 30°C and compared with the steady state

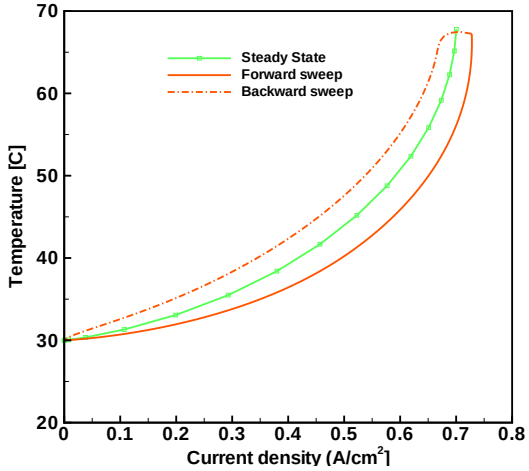

Figure 4.24: Dynamic cell temperature response to a potential sweep simulated at RHa=10% RHc=60% T_{amb} = 30°C and compared with the steady state

Chapter 5

Summary and Outlooks

5.1 Summary

A time-dependent, non-isothermal model of a proton exchange membrane fuel cell (PEMFC) was developed in this thesis, and solved using the finite element method. The model was applied to investigate dynamic behaviours in the membrane electrode assembly (MEA). In addition to solving a phenomenological transport equation for water in the membrane, the model takes into account non-equilibrium water sorption to better capture some of the dynamic characteristics of water transport in the MEA. Additional features of the model is two-phase transport in the porous electrodes as well as the resolution of the catalyst layer by using two macroscopic models: the macro-homogeneous model and the more representative agglomerate model. The model was first solved in for steady state conditions using a two-dimensional domain.

Validation and benchmarking of the model were performed against available experimental data in which measurements were made in a segmented cell that allows good representation of 2D conditions, as well as against an in-house computational code. The predicted polarization curve using the model accompanied with the two-phase submodel are found to be in good agreement with experimental data , and indicate that partial saturation/flooding of the GDL has a significant impact on the predicted performance.

The model was next used to investigate fuel cell operation under various conditions in the time domain by performing one-dimensional time-dependent, two-phase, non-isothermal simulations. The computing time for 2D case with 36330 degrees of freedom is 19.2 minutes on a PC with a single Intel 2.8 GHz processor and 1 Gb of RAM and 252 s for a 1D simulation of 10 mV/s potential sweep rate with 1786 degrees of freedom. Some highlights from the numerical analysis are

- The operating parameters influencing fuel cell performance in unsteady operation include rate of load change and membrane hydration level. The membrane hydration level, which is a function of operating conditions (pressure, temperature and inlet gas relative humidity), and dominates the direction and net rate of water transport and dictates the balance of water in the membrane.

- The rate of potential sweep has a significant impact on the fuel cell performance. For the fuel cell operated at the same inlet gas humidity on both sides, the higher rate yield higher current gains (for a given potential), particularly at

higher current densities.

- The threshold current density at which the polarization curves for forward and backward sweep cross trends to move towards higher density when cell temperature is increased.

- The membrane water sorption rate has significant impact on fuel cell performance in terms of controlling dynamic hydration of the membrane.

- Results from the model application to air-breathing fuel cell shed some highlight on the dynamic performance characteristics of passive fuel cells, especially in terms of the impact of increased temperature during the course of operation.

5.2 Outlooks

To further improve the dynamic modelling of the fuel cell components and achieve a more comprehensive representation of the processes, there are some critical issues that need to be resolved.

- As the results show material and transport properties have a significant impact on predicted performance, and particularly on membrane water content. Measurements to determine key properties of membranes such as liquid-vapor sorption coefficients, are required.

- Extension of the model to a full 3D-dimensional representation would allow simulation of larger systems typical for instance of automotive stacks and its application to transient operation scenario such as a start-up/shut-down and purging.

- When modelling the phase transition of water, evaporation and condensation rate constants are commonly used. Rather than using constants, more sophisticated models should contain a functional dependence of the evaporation and condensation rates. Condensation in micro-pores , for example, occurs on pre-existing liquid surfaces and, hence, the surface energy influences the condensation rate. Furthermore, the impact of the temperature, the average gas velocity, and the relative humidity should be studied in detail.

- The incorporation of an electrochemical capacitor submodel should be considered to enhance the range of transient phenomena that can be captured by the model.

References

[1] Energy Information Adminstration. World energy outlooks 2007. Preprint 99-43 (SFB 359), Energy Information Adminstration, February 2007.

[2] J. Hord. Is hydrogen a safe fuel? *International Journal of Hydrogen Energy*, 3(2):157–176, 1978.

[3] M.A. DeLuchi. Hydrogen vehicles: an evaluation of fuel storage, performance, safety, environmental impacts, and cost. *International Journal of Hydrogen Energy*, 14(2):81–130, 1989.

[4] F. Rigas and S. Sklavounos. Evaluation of hazards associated with hydrogen storage facilities. *International Journal of Hydrogen Energy*, 30(13-14):1501–1510, October 2005.

[5] A.J.C.M. Matthijsen and E.S. Kooi. Safety distances for hydrogen filling stations. *Fuel Cells Bulletin*, 11(11):12–16, November 2006.

[6] A.L. Vetere Arellano C. Kirchsteiger and E. Funnemark. Towards establishing

an international hydrogen incidents and accidents database (hiad). *Journal of Loss Prevention in the Process Industries*, 20(1):98–107, January 2007.

[7] D.S. Scott. *Smelling Land:The Hydrogen Defense Against Climate Catastrophe*. Canadian Hydrogen Association, 1 edition, 2007.

[8] US Department of Energy. Fuel cell report to congress. Preprint 99-43 (SFB 359), US House Report 107-234, February 2003.

[9] M A J Cropper S Geiger and D M Jollie. Fuel cells:a survey of current development. *J.Power Sources*, 131:57–61, 2004.

[10] Y. Wang and C.Y. Wang. Transient analysis of polymer electrolyte fuel cells. *Electrochimica Acta*, 50(6):1307–1315, January 2005.

[11] R.S. Gemmen and C.D. Johnson. Effect of load transients on sofc operationcurrent reversal on loss of load. *Journal of Power Sources*, 144(1):152–164, June 2005.

[12] H.R. Kunz M.V. Williams and J.M. Fenton. Operation of nafion-based pem fuel cells with no external humidification: influence of operating conditions and gas diffusion layers. *Journal of Power Sources*, 135(1-2):122–134, September 2004.

[13] S. Shimpalee S. Kim and J.W. Van Zee. The effect of stoichiometry on dynamic

behavior of a proton exchange membrane fuel cell (pemfc) during load change. *Journal of Power Soureces*, 135(1–2):110–121, September 2004.

[14] S. Shimpalee S. Kim and J.W. Van Zee. The efects of reservoirs and fuel dilution on the dynamic behavior of a pemfc. *Journal of Power Soureces*, 137(1):43–52, October 2004.

[15] S. Rael W. Friede and B. Davat. Mathematical model and characterization of the transient behavior of a pem fuel cell. *IEEE Transections on Power Electronics*, 19(5):1234–1241, September 2004.

[16] J.F. Moxley J. Benziger, E. Chia and I.G. Kevrekidis. The dynamic response of pem fuel cells to changes in load. *Journal of Chemical Engineering Science*, 60(6):1743–1759, 2005.

[17] Q. Yan, H. Toghiani, and H. Causey. Steady state and dynamic performance of proton exchange membrane fuel cells(pemfcs)under various operating conditions and load changes. *Journal of Power Sources*, 161(8):492–502, October 2006.

[18] W.H.J. and J.B. Benziger. Operation of polymer electrolyte membrane fuel cells with dry feeds: Design and operating strategies. *Journal of Power Sources*, 159(2):968–978, September 2006.

[19] R. Thangamuthu G. Sasikumar P. Sridhar N. Rajalakshmi, T.T. Jayanth and K.S. Dhathathreyan. Water transport characteristics of polymer electrolyte

membrane fuel cell. *International Journal of Hydrogen Energy*, 29(10):1009–1014, August 2004.

[20] H. Yu and C. Ziegler. Transient behavior of a proton exchange membrane fuel cell under dry operation. *Journal of Eletrochemical Society*, 153(3):A570–A575, November 2006.

[21] J. Hamelin, K. Agbossou, A. Laperriere, F. Laurencelle, and T.K. Bose. Dynamic behavior of a pem fuel cell stack for stationary applications. *International Journal of Hydrogen Energy*, 26(6):625–629, June 2000.

[22] T.A. Zawodzinski, J. Davey, J. Valerio, and S. Gottesfeld. The water content dependence of electro-osmotic drag in proton-conducting polymer electrolytes. *Journal of Eletrochemica Acta*, 40(3):297–302, June 1994.

[23] A. Marek F.N. Büchi and G.G. Scherer. In situ membrane resistance measurements in polymer electrolyte fuel cells by fast auxiliary current pulses. *Journal of The Electrochemical Society*, 142(6):1895–1901, June 1995.

[24] P W Gibson D Rivin, C E Kendrick and N S Schneider. Soluability and transport behavior of water and alcohols in nafion. *Polymer*, 42(2):623–635, January 2001.

[25] S. Motupally, A. J. Becker, and J.W. Weidner. Diffusion of water in nafion 115 membranes. *J. Electrochem. Soc.*, 147(9):3171–3177, September 2000.

[26] M. Ciureanu and M. Badita. Water balance experiments in pem fc stacks. measurements of water transport across the nafion membrane. *Journal of New Materials for Electrochemical Systems*, 6(3):163–168, July 2003.

[27] B. Yi S. Ge, X. Li and I. Hsing. Absorption, desorption, and transport of water in polymer electrolyte membranes for fuel cells. *Journal of Eletrochemical Society*, 152(6):A1149–A1157, May 2005.

[28] J.A. Evans P.M. Cronin D.M. Johnson T. Tanaka, T. Azuma and R.P. Cleaver. Experimental study on hydrogen explosions in a full-scale hydrogen filling station model. *International Journal of Hydrogen Energy*, 13(13):2162–2170, September 2007.

[29] P W Majsztrik M B SatterfieldA B Bocarsly and J B Benziger. Water sorption, desorption and transport in nafion membranes. *Journal of Membrane Science*, 301(1-2):93–106, September 2007.

[30] X. Ye and M.D. Levan. Water transport properties of nafion membranes part i. single-tube membrane module for air drying. *J.Membrane Science*, 221(1–2):371–379, August 2003.

[31] A. Trojanek P. Krtil and Z. Samec. Kinetics of water sorption in nafionthin films - quartz crystal microbalance study. *Journal of Physical Chemistry B*, 105(33):7979–7983, August 2001.

[32] B. Yi S. Ge and P. Ming. Experimental determination of electro-osmotic drag coefficient in nafion membrane for fuel cells. *Journal of Eletrochemical Society*, 153(8):A1443–A1450, 2005.

[33] H. Takata, N. Mizuno, M. Nishikawa, S. Fukada, and M. Yoshitake. Adsorption properties of water vapor on sulfonated perfluoropolymer membranes. *International Journal of Hydrogen Energy*, 32(3):371–379, March 2007.

[34] A.K. Prasad F.Y. Zhang, D. Spernjak and S.G. Advani. In situ characterization of the catalyst layer in a polymer electrolyte membrane fuel cell. *Journal of Eletrochemical Society*, 154(11):B1152–B1157, September 2007.

[35] G. Hagen H. Weydahl, S. Moller-Holst and B. Borresen. Transient response of a proton exchange membrane fuel cell. *Journal of Power Sources*, 171(2):321–330, September 2007.

[36] S. Wagner R. Hahn A. Schmitz, M. Tranitz and C. Hebling. Planar self-breathing fuel cells. *Journal of Power Sources*, 118(1–2):162–171, May 2003.

[37] R. Hahn H. Uzun A. Schmitz, S. Wagner and C. Hebling. Stability of planar pemfc in printed circuit board technology. *Journal of Power Sources*, 127(1–2):197–205, March 2004.

[38] T. Fabian, J.D. Posner, R. O'Hayre, S.W. Cha, J.K. Eaton, F.B. Prinz, and J.G. Santiago. The role of ambient conditions on the performance of a planar,

air-breathing hydrogen pem fuel cell. *Journal of Power Sources*, 161(1):168–182, October 2006.

[39] S. Litster and N. Djilali. Mathematical modelling of ambient air-breathing fuel cells for portable devices. *Electrochimica Acta*, 52(11):3849–3862, March 2007.

[40] H.J. Kim T.H. Lim I.H. Oh S.H. Kim S.U. Jeong, E.A. Cho. A study on cathode structure and water transport in air-breathing pem fuel cells. *Journal of Power Sources*, 159(2):1089–1094, September 2006.

[41] H.J. Kim T.H. Lim I.H. Oh S.H. Kim S.U. Jeong, E.A. Cho. Effects of cathode open area and relative humidity on the performance of air-breathing polymer electrolyte membrane fuel cells. *Journal of Power Sources*, 158(1):348–353, July 2006.

[42] K. Scott P. Argyropoulos and W. M. Taama. Dynamic response of the direct methanol fuel cell under variable load conditions. *Journal of Power Sources*, 87(1-2):153–161, April 2000.

[43] S. Zhou K. Scott M. Ginkel K. Sundmacher, T. Schultz and E. D. Gilles. Dynamics of the direct methanol fuel cell (dmfc): experiments and model-based analysis. *Journal of Chemical Engineering Science*, 56(2):333–341, January 2001.

[44] E. B. Martin K. Scott A. J. Morris A. Simoglou, P. Argyropoulos and W. M. Taama. Dynamic modelling of the voltage response of direct methanol fuel cells

and stacks part i: Model development and validation. *Journal of Chemical Engineering Science*, 56(23):6761–6772, December 2001.

[45] E. B. Martin K. Scott A. J. Morris A. Simoglou, P. Argyropoulos and W. M. Taama. Dynamic modelling of the voltage response of direct methanol fuel cells and stacks part ii: Feasibility study of model-based scale-up and scale-down. *Journal of Chemical Engineering Science*, 56(23):6773–6779, December 2001.

[46] L.T. Biegler C. Xu, P.M. Follmann and M.S. Jhon. Numerical simulation and optimization of a direct methanol fuel cell. *Journal of Computers and Chemical Engineering*, 29(8):1849–1860, July 2005.

[47] K. Scott P. Argyropoulos and W. M. Taama. The effect of operating conditions on the dynamic response of the direct methanol fuel cell. *Journal of Electrochimica Acta*, 45(12):1983–1998, February 2000.

[48] D. Natarajan and T.V. Nguyen. A two-dimensional, two-phase, multicomponent, transient model for the cathode of a proton exchange membrane fuel cell using conventional gas distributors. *Journal of The Electrochemical Society*, 148(12):A1324–A1335, November 2001.

[49] Hu Guilin and Fan Jianren. Transient computation fluid dynamics modeling of a single proton exchange membrane fuel cell with serpentine channel. *Journal of Power Sources*, In Press 2007, November 06 2007.

[50] Z.S. Liu D. Song, Q. Wang and C. Huang. Transient analysis for the cathode gas diffusion layer of pem fuel cells. *Journal of Power Sources*, 159(2):928–942, September 2006.

[51] R. Madhusudana Rao and R. Rengaswamy. A distributed dynamic model for chronoamperometry, chronopotentiometry and gas starvation studies in pem fuel cell cathode. *Chemical Engineering Science*, 61(22):7393–7409, June 2006.

[52] Y. Wang and C.Y. Wang. Transient analysis of polymer electrolyte fuel cells. *Electrochimica Acta*, 50(6):1307–1315, January 2005.

[53] P. Berg H. Wu and X. Li. Non-isothermal transient modeling of water transport in pem fuel cells. *Journal of Power Sources*, 165(1):232–243, February 2007.

[54] Thomas F. Fuller and John Newman. Water and thermal management in solid-polymer electrolyte fuel cells. *Journal of The Electrochemical Society*, 140(5):1218–1225, May 1993.

[55] A. Rowe and X. Li. Mathematical modeling of proton exchange membrane fuel cells. *Power Sources*, 102:82–96, March 2001.

[56] A.G. Stefanoopoulou J.T. Pukruspan and H. Peng. Modeling and control for pem fuel cell stack system. In *Proceedings of American Control Conference*, Anchorage, AK, May 8-10 2002.

[57] K. Haraldsson and K. Wipke. Evaluating pem fuel cell system models. *Journal of Power Sources*, 126(1-2):88–97, February 2004.

[58] K.B. McAuley P. Oosthuizen B. Peppley K.Z. Yao, K. Karan and T. Xie. A review of mathematical models for hydrogen and direct methanol polymer electroyte membrane fuel cells. *Fuel Cells*, 4(1-2):3–29, 2004.

[59] A.Z. Weber and J. Newman. Modeling transport in polymer-electrolyte fuel cells. *Journal of Chemical Reviews*, 104(10):4679–4726, October 2004.

[60] C.Y. Wang. Fundamental models for fuel cell engineering. *Journal of Chemical Reviews*, 104(10):4727–4766, October 2004.

[61] J.C. Amphlett, R.F. Mann, B.A. Peppley, P.R. Roberge, and A Rodrigues. A model predicting transient responses of proton exchange membranes fuel cells. *Journal of Power Sources*, 61(1–2):183–188, July–August 1996.

[62] S. Sirivasan J. Kim, S.M. Lee and C.E. Chamberlin. Modeling of proton exchange membrane fuel cell performance with an impirical equation. *Journal of The Electrochemical Society*, 142(1):2670–2674, August 1995.

[63] J.W. Van Zee S. Shimpalee, W.k. Lee and H. Naseri-Neshat. Predicting the transient response of a serpentine flow-field pemfc: I. excess to normal fuel and air. *Journal of Power Sources*, 156(2):355–368, June 2006.

[64] J.W. Van Zee S. Shimpalee, W.K. Lee and H. Naseri-Neshat. Predicting the

transient response of a serpentine flow-field pemfc: Ii: Normal to minimal fuel and air. *Journal of Power Sources*, 156(2):369–374, June 2006.

[65] Y. Wang and C.Y. Wang. Dynamics of polymer electrolyte fuel cells undergoing load changes. *Electrochimica Acta*, 51:3924–3933, December 2006.

[66] D. Spuckler S. Shimpalee and J.W. Van Zee. Prediction of transient response for a 25-cm2 pem fuel cell. *Journal of Power Sources*, 167(1):130–138, May 2007.

[67] A. Feliachi S. Yerramalla, A. Davari and T. Biswas. Modeling and simulation of the dynamic behavior of a polymer electrolyte membrane fuel cell. *Journal of Power Sources*, 124(1):104–113, October 2003.

[68] O. Gorseth T. Okada, S. M?ller-Holst and S. Kjelstrup. Transport and equilibrium properties of nafion? membranes with h+ and na+ ions. *Journal of Electroanalytical Chemistry*, 442(1-2):137–145, January 1998.

[69] H. P.L.H. van Bussel, F.G.H. Koene, and R.K.A.M. Mallant. Dynamic model for solid polymer fuel cell water management. *Journal of Power Sources*, 71(1-2):218–222, March 1998.

[70] F. Chen, Y.G. Su, C.Y. Soong, W.M. Yan, and H.S. Chu. Transient behavior of water transport in the membrane of a pem fuel cell. *Journal of Electroanalytical Chemistry*, 566:85–93, November 2004.

[71] K. Sundmacher V. John R. L?bke G. Matthies U. Krewer, Y. Song and L. Tobiska. Direct methanol fuel cell (dmfc): analysis of residence time behaviour of anodic flow bed. *Journal of Chemical Engineering Science*, 59(1):119–130, January 2004.

[72] U. Krewer and K. Sundmacher. Transfer function analysis of the dynamic behaviour of dmfcs: Response to step changes in cell current. *Journal of Power Sources*, 154(1):153–170, March 2006.

[73] K. Bolwin W. Schnurnberger M. Fischer W. Neubrand M. Wöhr and G. Eigenberger. Dynamic modeling and simulation of a polymer membrane fuel cell including mass transport limitation. *Journal of Hydrogen Energy*, 23(3):213–218, March 1998.

[74] K. Yasuda D. Bever, M. Wöhr and K.Oguro. Simulation of a polymer electrolyte fuel cell electrode. *Journal of Applied Electrochem*, 27(11):1254–1264, November 1997.

[75] S. Shimpalee S. Dutta and J.W. Van Zee. Numerical prediction of mass-exchange between cathode and anode channels in a pem fuel cell. *Journal of Heat and Mass Transfer*, 44(11):2029–2042, June 2001.

[76] S. Um and C.Y. Wang. Computational study of water transport in proton exchange membrane fuel cells. *Journal of Power Sources*, 156(2):211–223, June 2006.

[77] C. Miulli M. Ceraolo and A. Pozio. Modelling static and dynamic behaviour of proton exchange membrane fuel cells on the basis of electro-chemical description. *Journal of Power Sources*, 113(1):131–144, January 2003.

[78] C. Ziegler, H.M. Yu, and J.O. Schumacher. Two-phase dynamic modeling of pemfcs and simulation of cyclo-voltammograms. *Journal of Eletrochemical Society*, 152(8):A1555–A1567, July 2005.

[79] A.Z. Weber and J. Newman. Transport in polymer-electrolyte membranes iii. model validation in a simple fuel-cell model. *Journal of The Electrochemical Society*, 151(2):A326–A339, October 2004.

[80] P.C. Sui A.A. Shah, G.S. Kim and D. Harvey. Transient non-isothermal model of a polymer electrolyte fuel cells. *Journal of Power Sources*, 162(1):793–806, January 2007.

[81] X. Lia H. Wu and P. Berg. Numerical analysis of dynamic processes in fully humidified pem fuel cells. *International Journal of Hydrogen Energy*, 32(12):2022–2031, August 2007.

[82] Y. Shan and S.Y. Choe. A high dynamic pem fuel cell model with temperature effects. *Journal of Power Sources*, 145(1):30–39, July 2005.

[83] S.Y. Choe Y. Shan and Seo-Ho Choi. Unsteady 2d pem fuel cell modeling for a stack emphasizing thermal effects. *Journal of Power Sources*, 165(1):196–209, February 2007.

[84] T.E. Springer, T.A. Zawodzinski, and S. Gottesfeld. Polymer electrolyte fuel cell model. *Journal of Eletrochemical Society*, 138(8):2334–2342, August 1991.

[85] O. Zikanov A. Vorobev and T. Shamim. A computational model of a pem fuel cell with finite vapor absorption rate. *Journal of Power Sources*, 166(1):92–103, March 2007.

[86] B.A. Peppley P.R. Roberge J.C. Amphlett, R.F. Mann and T.J. Harris. Performance modeling of the ballard mark iv solid eelectrolyte membranes fuel cell i.mechanistic model development. *Journal of The Electrochemical Society*, 142(1):1–8, January 1995.

[87] J. Garnier. Dynamic pem fuel cell modeling for automotive applications. In *58th IEEE Semiannal Vehicular Technology Conference*, Orlando, FL, October 2003.

[88] K. Miyatake H. Uchida O. Nishikawa, K. Doyama and M. Watanabe. Gas diffusion electrodes for polymer electrolyte fuel cells using novel organic/inorganic hybrid electrolytes: effect of carbon black addition in the catalyst layer. *Journal of Electrochimica Acta*, 50(13):2719–2723, April 2005.

[89] V.K. Mathur and J. Crawford. *Recent Trends in Fuel Cell Science and Technology*, chapter Fundamentals of Gas Diffusion Layers in PEM Fuel Cells. Springer Netherlands, October 2007.

[90] B. Farhanieh R. Roshandel and E. Saievar Iranizad. The effects of porosity distribution variation on pem fuel cell performance. *Journal of Renewable Energy*, 30(10):1557–1572, August 2005.

[91] W.M. Yan J.H Jang and C.C. Shih. Effects of the gas diffusion-layer parameters on cell performance of pem fuel cells. *Journal of Power Sources*, 161(1):323–332, October 2006.

[92] D. Li M. Pan Z. Zhan, J. Xiao and R. Yuan. Effects of porosity distribution variation on the liquid water flux through gas diffusion layers of pem fuel cells. *Journal of Power Sources*, 160(2):1041–1048, October 2006.

[93] E. Spohr K.D. Kreuer, S.J. Paddison and Michael Schuster. Transport in proton conductors for fuel-cell applications: Simulations, elementary reactions, and phenomenology. *Journal of Chemical Reviews*, 104(10):4637–4678, October 2004.

[94] Friedrich Helfferich. *Ion Exhange*. Dover Publication NewYork, 1 edition, 1995.

[95] N.H. Jalani and R.Datta. The effect of equivalent weight, temperature, cationic forms, sorbates, and nanoinorganic additives on the sorption behavior of nafion. *Journal of Membrane Science*, 264(1):167–175, November 2005.

[96] J. Fimrite H. Struchtrup and N. Djilali. Transport phenomena in polymer electrolyte membranes. part i: modeling framework. *Journal of The Electrochemical Society*, 152(9):A1804–A1814, August 2005.

[97] Donald A Nield and A Bejan. *Convection in Porous Media*. Springer NewYork, 3 edition, 1998.

[98] D. Chenu M. Quintarda, L. Bletzacker and S. Whitaker. Nonlinear, multi-component, mass transport in porous media. *Journal of Chemical Engineering Science*, 61:2643–2669, 2006.

[99] W.E. Stewart R.B. Bird and E.N. Lightfoot. *Teansport Phenomena*. JOhn Wiley and Sons Inc, 1 edition, 1960.

[100] E.L. Cussler. *Diffusion Mass transfer in Fluid Systems*. Cambrige Unoversity Press, 2 edition, 1997.

[101] X.G. Yang F.Y. Zhang and C.Y. Wang. Liquid water removal from polymer electrolyte membrane fuel cell. *Journal of Eletrochemical Society*, 153(2):A225–A232, February 2006.

[102] G.J.M. Janssen. A phenomenological model of water transport in a proton exchange membrane fuel cell. *Journal of The Electrochemical Society*, 148(12):A1313–A1323, November 2001.

[103] H. Tang T. Thampan, S. Malhotra and R. Datta. Modeling of conductive transport in proton-exchange membranes for fuel cells. *Journal of The Electrochemical Society*, 147(9):3242–3250, September 2000.

[104] A.Z. Weber and J. Newman. Transport in polymer-electrolyte membranes ii.

mathematical model. *Journal of The Electrochemical Society*, 151(2):A311–A325, October 2004.

[105] H. Struchtrup J. Fimrite, B. Carnes and N. Djilali. Transport phenomena in polymer electrolyte membranes. part ii: Binary friction membrane model. *Journal of The Electrochemical Society*, 152(9):A1815–A1823, August 2005.

[106] A. Suleman M. Secanell, K. Karan and N. Djilali. Multi-variable optimization of pemfc cathodes using an agglomerate model. *Journal of Electrochimica Acta*, 52(7):6318–6337, June 2007.

[107] K. Karan. Assessment of transport-limited catalyst utilization for engineering of ultra-low pt loading polymer electrolyte fuel cell anode. *Electrochemistry Communications*, 9(4):747–753, April 2007.

[108] M. Tranitz E. Fontes C. Ziegler, A. Schmitz and J. O. Schumacher. Modeling planar and self-breathing fuel cells for use in electronic devices. *Journal of The Electrochemical Society*, 151(12):A2028–A2041, 2004.

[109] M.G. Secanell. *Computational modeling and optimization of proton exchange membrnae fuel cells*. PhD thesis, University of Victoria, December 2007.

[110] D.M. Bernardi and M.W. Verbrugge. Mathematical model of a gas diffusion electrode bonded to a polymer electrolyte. *AIChE*, 37(8):115–1163, August 1991.

[111] M. Mizuhata J.T. Hinatsu and H. Takenaka. Water uptake of perfluorosulfonic acid membranes from liquid water and water vapor. *Journal of The Electrochemical Society*, 141(6):1493–1498, June 1994.

[112] A.R. Garcia D.J. Burnett and F. Thielmann. Measuring moisture sorption and diffusion kinetics on proton exchange membranes using a gravimetric vapor sorption apparatus. *Journal of Power Sources*, 29(1):426–430, September 2006.

[113] C.Y. Hsu A. Su, F.B. Weng and Y.M. Chen. Studies on flooding in pem fuel cell cathode channels. *International Journal of Hydrogen Energy*, 31(8):1031–1039, July 2006.

[114] G. Lin and T. V. Nguyen. A two-dimensional two-phase model of a pem fuel cell. *Journal of The Electrochemical Society*, 153(2):A372–A382, 2006.

[115] T. Berning and N. Djilali. A 3d, multi-phase, multicomponent model of the cathode and anode of a pem fuel cell. *Journal of The Electrochemical Society*, 150(12):A1589–A1598, December 2003.

[116] U. Pasaogullari and C. Y. Wang. Liquid water transport in gas diffusion layer of polymer electrolyte fuel cells. *Journal of The Electrochemical Society*, 151(3):A399–A406, 2004.

[117] H. Ju G. Luo and C.Y. Wang. Prediction of dry-wet-dry transition in polymer electrolyte fuel cells. *Journal of The Electrochemical Society*, 154(3):B316–B321, 2007.

[118] Q. Ye and T.V. Nquyen. Three-dimensional simulation of liquid water distribution in a pemfc with experimentally measured capillary functions. *Journal of The Electrochemical Society*, 154(12):B1241–B1251, December 2007.

[119] V.P. Carey. *Liquid Vapor Phase Change Phenomena: An Introduction to the Thermophysics of Vaporization and Condensation Processes in Heat Transfer Equipment*. John Wiley and Sons Inc, 1 edition, 1992.

[120] R. Marek and J. Straub. Analysis of the evaporation coefficient and the condensation coefficient of water. *International Journal of Heat and Mass Transfer*, 44(1):39–53, January 2001.

[121] S. Mazumder and J.V. Cole. Rigorous 3-d mathematical modeling of pem fuel cells i. model predictions with liquid water transport. *Journal of The Electrochemical Society*, 150(11):A1503–A1509, November 2003.

[122] COMSOL AB. *COMSOL Multiphysics: Chemical Engineering Module User's Guide*. Stockholm Sweden, 2005.

[123] A Z Weber and J Newman. Modeling transport in polymer-electrolyte fuel cells. *Journal of Chemical Reviews*, 104:4679–47269, 2004.

[124] T.R. Ralph S. Slade, S.A. Campbell and F.C. Walsh. Ionic conductivity of an extruded nafion 1100 ew series of membranes. *Journal of The Electrochemical Society*, 149(12):A1556–A1564, October 2002.

[125] A. Suleman M. Secanell, B. Carnes and N. Djilali. Numerical optimization of proton exchange membrane fuel cell cathodes. *Journal of Electrochimica Acta*, 52(7):2668–2682, February 2007.

[126] D.M. Bernardi and M.W. Verbrugge. A mathematical model of the solid-polymer-electrolyte fuel cell. *Journal of Eletrochemical Society*, 139(9):2477–1163, September 1992.

[127] M.S. Wilson G. Bender and T.A. Zawodzinski. Further refinements in the segmented cell approach to diagnosing performance in polymer electrolyte fuel cells. *Journal of Power Sources*, 123(2):163–171, September 2003.

[128] M. Vynnycky C. Picard E. Birgersson, J. Nordlund and G. Lindbergh. Reduced two-phase model for analysis of the anode of a dmfc. *Journal of The Electrochemical Society*, 151(12):A2157–A2172, 2004.

[129] G.H. Guvelioglu and H.G. Stenger. Computational fluid dynamics modeling of polymer electrolyte membrane fuel cells. *Journal of Power Sources*, 147(1-2):95–106, September 2005.

[130] Q. Yan, H. Toghiani, and H. Causey. Investigation of water transport through membrane in a pem fuel cell by water balance experiments. *Journal of Power Sources*, 158(1):316–325, July 2006.